Space-Time Adaptive Monopulse Processing

A THESIS

Presented to

The Academic Faculty

By

Yaron Seliktar

In Partial Fulfillment

of the Requirements for the Degree of

Doctor of Philosophy in Electrical Engineering

Georgia Institute of Technology

December 1998

Space-Time Adaptive Monopulse Processing

Approved:

Douglas B. Williams, Chairman

James H. McClellan

E. Jeff Holder

Date approved by Chairman _____

Dedicated to my parents

Acknowledgments

First and foremost I thank G-d.

I would like to thank my advisor, Professor Douglas Williams, for his help and support throughout the course of my study and research at Georgia Tech. Our many discussions and his valuable advice went a long way to shape my research giving it both purpose and direction. My thanks also go to Dr. Jeff Holder of GTRI who has supported my work from early on, and whose suggestions and ideas in the area of radar signal processing formed the foundations of my research. I would like to thank Dr. Stephen Kogon of MIT Lincoln Laboratory for exposing me to his own work which served as a foundation for this thesis, and for providing his generous assistance and support throughout our overlap at Georgia Tech and beyond. I feel indebted to Professor Jim McClellan for serving on my thesis committee and offering his keen insights. His insistence on high standards and quality of work have made this thesis all the more complete. I also thank Dr. David Aalfs for sharing with me his knowledge on monopulse and various topics related to this thesis.

I would also like to extend my appreciation to the secretarial and computer staff at CSIP for their patience and help throughout my stay here. I would like to thank Stacy Schultz for going out of her way to ensure that all technical matters relating to my final defense and thesis were handled in an efficient and timely manner. Thanks to the faculty at CSIP for creating the excellent learning and research environment from which I prospered, and was privileged to be part of. I thank Dr. Marvin Cohen of GTRI for his friendship and his committed effort in assisting me in my employment

search, and providing the contacts and valuable recommendations that culminated in my acceptance of a position with Norden Systems Northrop Grumman.

Much gratitude goes to my family who have been a valuable source of love and support throughout the years. Finally, I would like to thank my friends here and the Beth Jacob community for making my years in Atlanta all the more pleasant.

Contents

List of Tables

List of Figures

Summary

Space/fast-time adaptive radar signal processing techniques have been shown to improve target detection in the presence of terrain scattered interference (TSI). These techniques exploit the temporal correlation of the jammer multipath components that make up the composite TSI signal. In a more difficult scenario, where a target is obscured by the direct path jammer signal and spatial nulling is rendered ineffective, TSI has been shown to aid in the suppression of the mainbeam jammer by a similar exploitation of the temporal correlation of the jammer multipath with the direct path jammer signal.

Once target detection has been accomplished, target tracking algorithms require accurate azimuthal and elevation angle readings of the target's position. However, the angle estimation problem has been confined primarily to purely spatial techniques and, therefore, fails to exploit the temporal correlation inherent in the interference. As with detection, much can be gained from the temporal correlation of the interference for improving angle estimation.

This thesis investigates two applications of space-time adaptive processing for angle estimation that take advantage of this correlation. In one application, fast-time processing coupled with spatial processing is used to improve angle estimation performance in the presence of TSI and mainbeam jamming. This technique combines space-time processing with monopulse techniques to yield an angle estimation algorithm. Results on experimental Mountaintop TSI data demonstrate the merit of the proposed algorithm under varied jamming and TSI conditions. For the second

application, monostatic clutter is also considered. Monostatic clutter (MSC) is produced by ground reflections from the radar's own transmitted signal that are incident on the radar aperture and possesses strong correlation in the space-Doppler domain. The use of joint space, fast-time, and Doppler processing is necessary to treat all three interference types simultaneously, but such processing is found to be computationally prohibitive for even small arrays. Current approaches separate the problem into two stages where TSI is suppressed first and then MSC. The problem with this cascade approach is that during the initial TSI suppression stage the MSC becomes corrupted. In this thesis an innovative technique is introduced for achieving a significant improvement in cancellation performance for both MSC and TSI, even when the jammer appears in the mainbeam. The majority of the interference rejection, both jamming and MSC, is accomplished with an MSC filter, with further TSI suppression accomplished via an additional tapped reference beam. Application of an appropriate set of constraints and simultaneous optimization of the MSC filter weights and reference beam weights yield the desired sum and difference components of the monopulse processor. Performance results using Mountaintop data demonstrate the superiority of the proposed processor over existing processors for both ground based and airborne radars and jammers.

CHAPTER 1

Introduction

The purpose of a monopulse radar is to perform angle tracking in the presence of interference. The same types of interference that hamper target detection in a surveillance radar also work against angle estimation in a monopulse radar. A typical source of interference is barrage noise jamming, where the jammer directs a wide spectrum of temporally uncorrelated noise energy at a radar's aperture with the intent of overpowering weak target returns. Phased array radars can effectively mitigate such interference by placing a spatial null in the direction of the jammer. However, when the angular separation between the jammer and target is sufficiently small that the jammer falls within the mainbeam of the radar's receive pattern, a more potent form of jamming is realized called mainbeam jamming. In such a case, spatial adaptive processing is inadequate and alternative solutions must be sought. A second and more difficult source of interference to contend with than ordinary sidelobe jamming is monostatic terrain clutter. Monostatic clutter (MSC) consists of reflections of the radar's own transmitted signal from surrounding terrain. Typical MSC is spatially diverse and, therefore, does not lend itself well to spatial nulling. Velocity discrimination by means of combined spatial and Doppler (i.e., space/slow-time) processing has been shown to be effective in mitigating MSC [7, 66, 67, 59].

A third and less common type of interference is terrain-scattered interference (TSI). Terrain-scattered interference is caused by a jammer that directs some or all of its energy at the surrounding terrain. The reflected jammer energy arrives at the radar

aperture with different delays and from different directions, and, therefore, the composite TSI signal has a wide spatial and temporal extent that renders spatial nulling ineffective. However, the TSI signal can be modeled as the output of a linear time-invariant system that represents the terrain surface with the jammer waveform as its input. As such, it is possible to utilize a system identification approach for mitigating the TSI; in other words, perform space/fast-time adaptive processing. A number of fast-time adaptive algorithms have been proposed and applied to the TSI mitigation problem. Most notable are the single reference Beam Canceler (SRB) [46, 18, 19] and its generalization, the Beamspace TSI Canceler by Kogon [34, 31]. The element space equivalent of the Beamspace TSI Canceler was developed concurrently by Griffiths [24]. Conversely, it is shown in [31, 32, 33, 37] that coherent multipath can be exploited to improve significantly interference mitigation performance in a mainbeam jamming scenario. The operation of this processor is based on the principle that delayed jammer reflections from the ground (i.e., TSI) present in the sidelobes can be used to estimate and, thus, cancel the direct path jammer in the mainbeam, which is similar in concept to the cancellation of wideband mainbeam jammers [15]. It has also recently become popular to borrow from the monopulse technique, traditionally used for angle estimation, to improve interference mitigation in the presence of mainbeam jamming. For instance, an adaptive space-time technique by Fante, that employs a conventional beam and a tapped reference monopulse difference beam to provide target free multipath information, provides improved mitigation performance in the presence of TSI and mainbeam jamming [14]. A similar technique by Jones employs additional tapped monopulse beams with Doppler compensation channels for improving mitigation performance in the presence of nonstationary mainbeam interference [30].

Although these various algorithms are able to mitigate MSC or TSI individually, in an airborne surveillance radar the two seldom occur separately. Three-dimensional adaptive processing (i.e., in space, fast-time, and slow-time) was proposed as a means

to combat the combined effects of jamming, TSI and, MSC [16]. However, for even a modest number of elements, pulses, and taps, the adaptive processor becomes computationally prohibitive and requires excessive training data. By employing a reduced cluster of beams in the beamspace, a slight reduction in the number of spatial degrees of freedom could be accomplished [16], but it is still insufficient for practical consideration. In [51], a variation of the reduced rank beamspace approach was proposed, which included the added features of variable beam taps and weight thinning. The factored beamspace approach by Kogon [31, 36] was designed to operate in the presence of combined jamming, TSI, and MSC by applying two adaptive stages in cascade. The first stage removes the TSI and jamming from the returns, with the second stage removing the remaining MSC interference. This algorithm, although of practical consideration, suffers from the "modulation" effect [51] where MSC interference is shifted and spread in Doppler. Preventative measures against the modulation effect are discussed by Rabideau for both the factored beamspace algorithm and for the reduced rank three-dimensional beamspace processor [51].

Extensive work has been done on the problem of adaptive angle estimation in the presence of sidelobe jamming and, to a lesser extent, mainbeam jamming. In [5], Brennan derives a lower bound on angle estimation performance for a phased array, and proceeds to compare angle estimation performance for amplitude comparison and phase comparison monopulse against that bound. In [11], Davis, Brennan and Reed used a maximum-likelihood angle estimator to derive adaptive sum and difference monopulse beams for nulling the external noise sources (i.e., jammers). Simulation results were presented for both sidelobe and mainbeam jamming. Nickel extended the maximum-likelihood estimation technique to alternative array geometries, subarray adaptive arrays, and arbitrary sum and difference beams [47]. In [10], constrained optimization was employed to improve the quiescent pattern characteristics of the distorted sum and difference beams that occur as a result of mainbeam jamming. Gabriel [20] employed a Butler matrix formulation [42] to arrive at adap-

tive sine/cosine illuminated sum and difference monopulse beams. An investigation of adaptive monopulse in a mainbeam jamming scenario was presented in [40, 39, 41] with a derived set of Cramer-Rao bounds that put a theoretical bound on achievable performance. In [40, 39] the adaptive monopulse system was based on Gabriel's formulation [20], whereas in [41] a new monopulse system based on a sidelobe canceler architecture was formulated. Virtually no work, however, has been done on angle-estimation techniques that address the problems of TSI and combined TSI and MSC, particularly when mainbeam jamming is present.

It is the primary goal of the thesis to treat the problem of angle estimation in these more complicated interference environments by applying and extending some of the adaptive techniques and ideas of TSI and mainbeam jamming mitigation developed in [31, 34, 35, 32, 33, 37, 22, 23] to the problem of angle estimation. Initially, the extension of standard monopulse to space-time monopulse will be confined to the case of TSI and mainbeam jamming. With the appropriate constraints, the space/fast-time processor of Kogon will be be made into a pair of sum and difference processors that make up the key component of the monopulse system. The space/fast-time monopulse processor is shown to offer improved performance over existing spatial-only techniques.

In the second part of this thesis, a new three-dimensional reduced rank algorithm will be introduced that is able contend with the combined effects of mainbeam jamming, TSI, and MSC, offering both improved interference mitigation and angle estimation performance over existing methods. Finally, the new technique is extended to perform monopulse.

CHAPTER 2

Space-Time Processing

Prior to presenting the algorithm development in Chapters 4, 5, and 6, background material pertaining to the topics of relevance – space-time processing and the monopulse technique – are addressed in this and the following chapter. Fundamental concepts in array signal processing are introduced and developed in the context of radar. These concepts are extended to the temporal domain corresponding to range in radar systems, and target and interference models are presented along with a number of the techniques available for mitigating such interference.

2.1 Spatial Array Fundamentals

Classical transmitter or receiver devices utilize a single transmitting or receiving antenna element to broadcast or receive the desired signal. The geometry and physical orientation of the antenna determines its directional properties. For instance, an omni-directional antenna element radiates uniformly in all directions and, conversely, is equally sensitive to signals arriving from all directions. A directional antenna, on the other hand, transmits and receives most efficiently in the direction in which it is oriented. Directional antennas are commonly found in radar and other devices that require high gain in a particular direction.

With an array of antenna elements it is possible for the overall array to emulate a variety of directional characteristics without altering the geometry, position, or

orientation of the individual antenna elements that make up the array. Proper phase and amplitude adjustments of an outgoing signal waveform at the individual elements focuses the radiated energy in a particular direction. Likewise, phase and amplitude weighting of incoming signals sensitizes the array to a particular direction. Utilizing phase and amplitude weighting as a means to achieve a desired steer direction is typically referred to as phase steering or beamforming [29].

Planar arrays (i.e., elements configured in a plane) permit beamforming in azimuth and elevation, whereas linear arrays (i.e., elements configured on an axis) permits beamforming in one but not the other. The number of elements in an array and their spacing determine the extent of the angular and temporal resolution afforded by the array. The particular configuration considered here is a uniform linear array (ULA) having N equally spaced elements, D meters apart. The array output at time t is represented by the $N \times 1$ vector

$$\mathbf{x}(t) = \left[\begin{array}{cccc} x_0(t) & x_1(t) & \cdots & x_{N-1}(t) \end{array} \right]^T, \tag{2.1}$$

where $x_n(t)$ are the voltage levels at the sensor outputs indexed 0 through N-1 and superscript T denotes the transpose operator. Delay-and-sum beamforming entails applying a set of weights and delays to the sensor outputs and summing them together.

A localized far field source transmits or echos a signal, $s(t)$, that arrives at the array approximating a plane wave as shown in Fig. 2.1. For a given angle of propagation (with respect to array broadside), ϕ, the time lag between wavefronts impinging on neighboring sensors is

$$\tau = \frac{D \sin \phi}{c}, \tag{2.2}$$

where c is the speed of propagation. If the incoming signal is narrowband (e.g., a complex sinusoid), then delays correspond to phase shifts and can, thus, be incorporated into the beamformer weights as complex phases. The normalized vector of beamformer weights

$$\mathbf{a}(\nu) = \frac{1}{\sqrt{N}} \left[\begin{array}{cccc} 1 & \mathrm{e}^{j2\pi\nu} & \cdots & e^{j2\pi\nu(N-1)} \end{array} \right]^T, \tag{2.3}$$

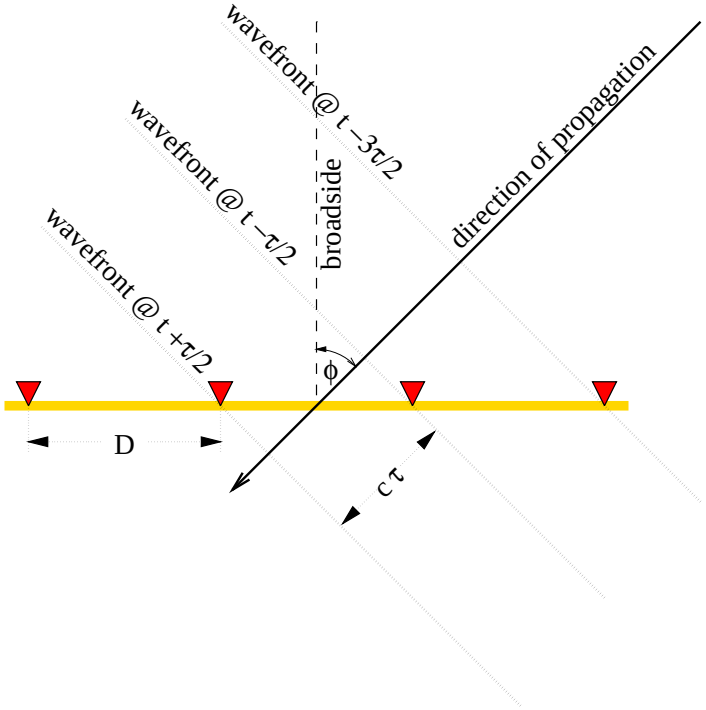

Figure 2.1: Plane wave impinging on an array.

also known as a steering vector, aligns the sensor outputs so that they sum coherently. These weights result in the maximum possible beamformer output (sensitivity) for a signal having spatial frequency ν (or corresponding angle ϕ)[29]. In order to prevent spatial aliasing (i.e., angular ambiguities), the inter-element spacing must satisfy $D < \frac{\lambda}{2}$, where $\lambda = \frac{c}{f_c}$ is the wavelength corresponding to the highest frequency component, f_c, in $s(t)$ [29]. The spatial frequency variable is related to angle by

$$\nu = f_c \tau = \frac{D}{\lambda} \sin \phi. \tag{2.4}$$

The beampattern [29] is defined as the response of a fixed beamformer, specified by its weight vector $\mathbf{w}$, to an ideal signal arriving from direction ν

$$\mathcal{W}(\nu) = \mathbf{w}^H \mathbf{a}(\nu), \tag{2.5}$$

where superscript H denotes the complex conjugate transpose operator. For the conventional beamformer weights, $\mathbf{w} = \mathbf{a}(\nu_0)$, the beampattern is shown in Fig. 2.2 and is given by

$$\mathcal{W}(\nu) = \frac{1}{N} \frac{\sin N\pi(\nu - \nu_0)}{\sin \pi(\nu - \nu_0)}. \tag{2.6}$$

The mainbeam consists of the central lobe containing the steering vector look direction (i.e., $\phi_0 = 0°$), whereas the sidelobes consist of the remaining lobes in the spectrum. The 3 dB beamwidth of the mainlobe is defined as the angular distance between the half power (i.e., 3 dB) points on the mainbeam [61]. Regardless of the number of sensors, the beampattern for the conventional beamformer is characterized by a peak sidelobe level that is 13 dB below the mainlobe peak.

2.2 Radar Background

2.2.1 Fundamentals of Radar

A radar (radio detection and ranging) device transmits a waveform into the atmosphere and then listens for echos as the transmitted waveform reflects back from

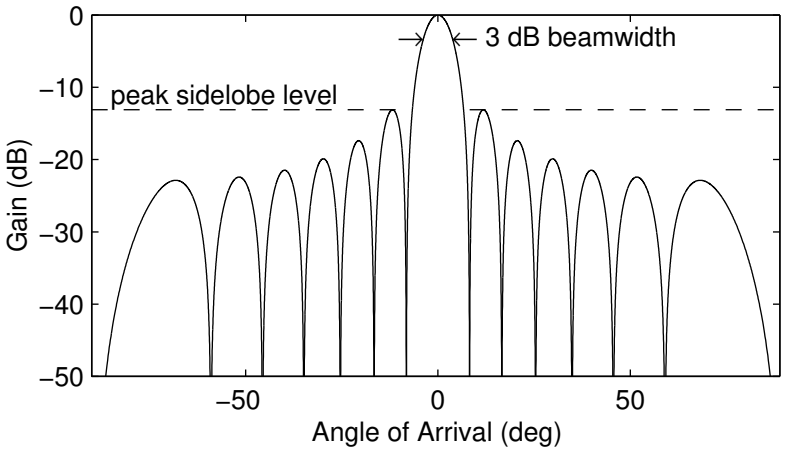

Figure 2.2: Beampattern for conventional beamformer of a 14 sensor array with half wavelength element spacing.

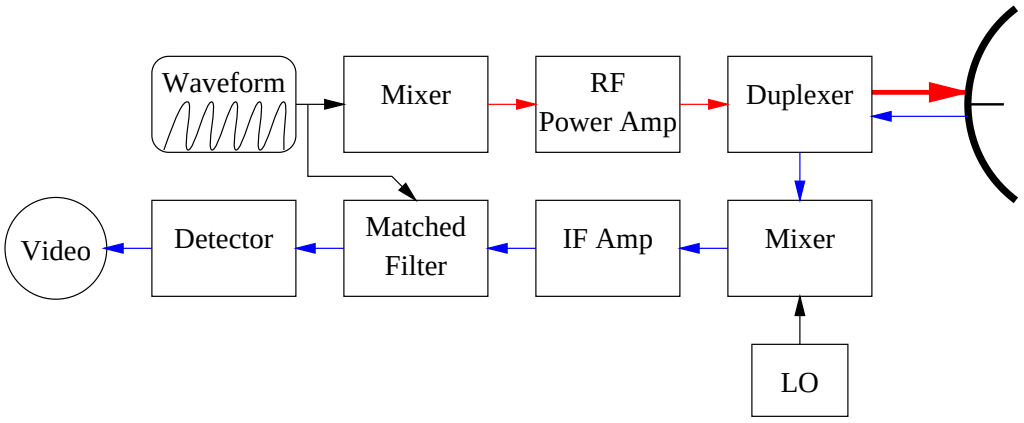

Figure 2.3: Conceptual block diagram of a radar system.

surrounding objects. Depending on the radar, various types of information can be obtained from the incoming echos about the desired scatterer object, known as the target. Range information can be inferred from the amount of time it takes the transmitted signal to travel to an object and then arrive back at the receiver. Directional information can be attained by scanning the surrounding space with a directive beam. Velocity or target movement can be determined through measuring the Doppler shift induced in the reflected waveform. The accuracy or resolution to which any of the above parameters can be measured depends to a large extent on the physical parameters of the radar and its electronics and to some extent on the environment in which it operates.

Different applications of radar call for different operating characteristics. Early warning airborne (AEW) radars typically operate in the UHF frequency range (300–1000 MHz) with average transmitter power in the KW (kilowatt) range [61]. The receiver bandwidth can be on the order of a few hundred KHz to a few MHz depending on the desired range resolution. A conceptual block diagram of a radar system is shown in Fig. 2.3 [61]. A duplexer permits the antenna to serve both the transmitter and receiver. The transmitted signal is typically generated at video frequency and boosted to RF where it is amplified and transmitted through the antenna. The

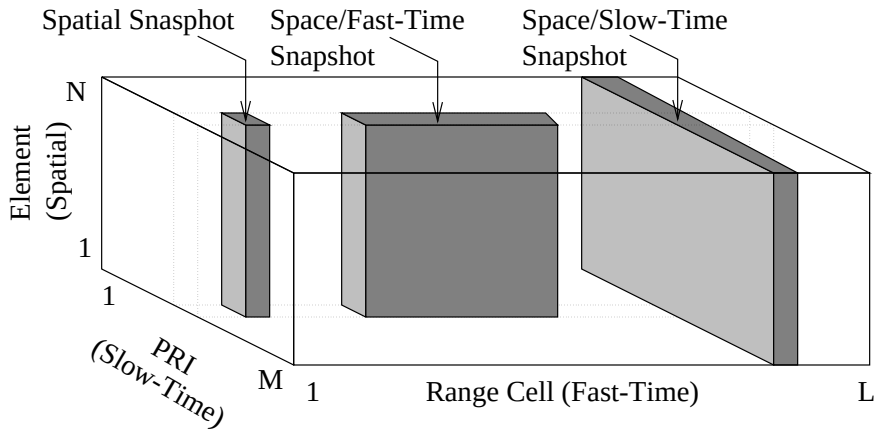

Figure 2.4: Datacube.

received signal is then amplified and mixed down to baseband where it is matched filtered, processed, and displayed.

2.2.2 Modern Pulsed Airborne Radar

Considered here is a radar system that transmits a sequence of M coherent pulses and samples the returns on an N element ULA.[1] The transmitted waveform is often a linear, frequency modulated (LFM) pulse having time duration, T_p, and bandwidth, W_p. The radar collects L temporal samples from each element receiver at each *pulse repetition interval* (PRI), where each time sample corresponds to a *range cell*. The three-dimensional datacube structure depicted in Fig. 2.4 represents the sampled returns in a single *coherent processing interval* (CPI) of M pulses. This set of samples is denoted by a sequence of M matrices $\mathbf{X}^{(m)}$(i.e., one for each pulse) with elements $x^{(m)}(n,l)$. To distinguish between temporal dimensions, the inter-PRI sampling dimension is referred to as *slow-time* and the range cell dimension as *fast-time* [65]. The element and slow-time dimensions are typically denoted in the frequency domain as spatial frequency (ν) and Doppler (f), respectively.

[1] In the notation used here, N denotes a scalar constant, $\mathbf{n}$ a spatial vector, and $\mathbf{N}$ a space-time vector or matrix.

From Fig. 2.4, a spatial snapshot consists of N elements of spatial data from the t^{th} range cell (i.e., t^{th} column of $\mathbf{X}^{(m)}$),

$$\mathbf{x}^{(m)}(t) = \begin{bmatrix} x^{(m)}(0,t) \\ x^{(m)}(1,t) \\ \vdots \\ x^{(m)}(N-1,t) \end{bmatrix}. \tag{2.7}$$

A space/slow-time (SST) snapshot, $\mathbf{X}(t)$, consists of stacked element data from consecutive pulses at a given range cell,

$$\mathbf{X}(t) = \begin{bmatrix} \mathbf{x}^{(0)}(t) \\ \mathbf{x}^{(1)}(t) \\ \vdots \\ \mathbf{x}^{(M-1)}(t) \end{bmatrix}. \tag{2.8}$$

Similarly, a space/fast-time (SFT) snapshot, $\mathbf{X}_T^{(m)}(t)$, consists of T consecutive spatial snapshots in descending order (i.e., T consecutive descending columns of $\mathbf{X}^{(m)}$):

$$\mathbf{X}_T^{(m)}(t) = \begin{bmatrix} \mathbf{x}^{(m)}(t) \\ \mathbf{x}^{(m)}(t-1) \\ \vdots \\ \mathbf{x}^{(m)}(t-T+1) \end{bmatrix}. \tag{2.9}$$

The two-dimensional SST steering vector steered in the direction of the desired spatial and normalized Doppler frequency pair $(\nu,\bar{f})$ is defined as

$$\mathbf{v} = \mathbf{v}(\nu,\bar{f}) = \mathbf{b}(\bar{f}) \otimes \mathbf{a}(\nu), \tag{2.10}$$

where $\otimes$ denotes a Kronecker product [27]. Assuming a uniform linear array and fixed PRI, the spatial and temporal phase-centered steering vectors are defined respectively as

$$\mathbf{a}(\nu) = \frac{\mathrm{e}^{-j\pi\nu(N-1)}}{\sqrt{N}} \begin{bmatrix} 1 & \mathrm{e}^{j2\pi\nu} & \cdots & \mathrm{e}^{j2\pi\nu(N-1)} \end{bmatrix}^T \tag{2.11}$$

$$\mathbf{b}(\bar{f}) = \frac{\mathrm{e}^{-j\pi\bar{f}(M-1)}}{\sqrt{M}} \left[\begin{array}{cccc} 1 & \mathrm{e}^{j2\pi\bar{f}} & \cdots & \mathrm{e}^{j2\pi\bar{f}(M-1)} \end{array} \right]^T. \tag{2.12}$$

The normalized Doppler frequency is $\bar{f} = fT_r$ where T_r is the PRI.

2.2.3 Interference Environment

For modern pulsed airborne radars the availability of spatial information and two kinds of temporal information, slow-time and fast-time, is necessary in order to detect targets in the presence of strong interference. Primary sources of interference include monostatic clutter (MSC) caused by the reflections of radar signals from the surrounding terrain, direct path jamming, and multipath jamming components known as hot clutter or terrain scattered interference (TSI). Returns containing MSC are correlated in space and slow-time, whereas returns containing TSI are correlated in space and fast-time. Both target and interference models are considered here.

A moving point target is typically modeled as a space-time steering vector having gain σ_t and occupying a single range cell,

$$\mathbf{X}_{tgt}(t) = \sigma_t \mathbf{v}(\nu, \bar{f})\delta[t - T_t], \tag{2.13}$$

where $\delta[t]$ is a discrete impulse function (i.e., equals one when argument is zero, and zero otherwise). The time taken for the reflecting echo to arrive back at the radar is proportional to the target range (r_t) [48],

$$T_t = \frac{2r_t}{c}. \tag{2.14}$$

The target is characterized by spatial frequency ν, which is related to the target angle by (2.4), and normalized Doppler frequency,

$$\bar{f} = \frac{2v_t T_r}{\lambda}, \tag{2.15}$$

where v_t is the target's radial velocity with respect to the radar platform [66]. An example of the space-Doppler spectrum of a target signal is illustrated in Fig. 2.5.

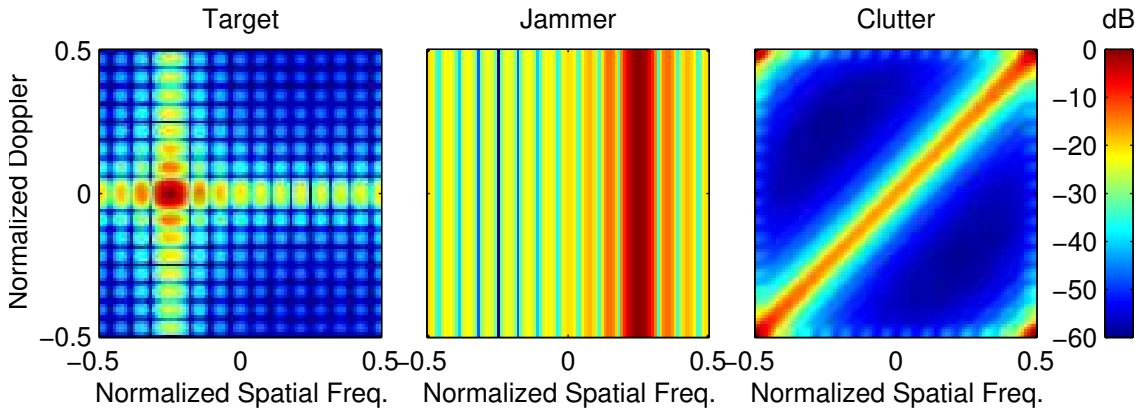

Figure 2.5: Space-Doppler spectrum of a target signal (left), jammer signal (center) and monostatic clutter signal (right).

The most fundamental form of interference is thermal noise appearing at the sensor outputs. Such noise is generated internally in the receiver electronics and is independent from one receiver to the next. Assuming separate receivers at each element, the thermal noise in an array is spatially and temporally uncorrelated (white) [66]. The thermal noise typically represents the lower-bound on achievable mitigation performance. As a result, both target and interference power levels are often expressed relative to the noise power or *noise floor*, σ_n^2, a practice that is adopted throughout the thesis.

Barrage noise jamming is the most common form of hostile interference. Such interference emanates from a spatially localized source and is temporally uncorrelated from sample to sample as well as from PRI to PRI. It is modeled as the Kronecker product of a white Gaussian $M \times 1$ noise vector, $\mathbf{n}_j(t)$, with a spatial steering vector,

$$\mathbf{X}_{jam}(t) = \mathbf{n}_j(t) \otimes \mathbf{a}(\nu), \tag{2.16}$$

where the power of each component of $\mathbf{n}_j(t)$ is σ_j^2. Based on this model, the jammer has spatial correlation only. This is particularly evident from Fig. 2.5, where the jammer energy appears spatially localized while spread in Doppler.

Reflections of the transmitted signal from the surrounding terrain, known as

monostatic clutter, typically accompany the target return. The reflecting terrain surface, characterized by a large cross-sectional area at any given range cell, can easily overwhelm the target. Since terrain characteristics vary significantly from one location to another, the precise correlation structure of the resulting MSC cannot be easily captured in a single model. A simple clutter model assumes that for each range cell there is a ring of terrain centered about the radar platform that produces reflections of the transmitted signal. For an omni-directional transmitter and uniformly reflecting terrain, the clutter returns can be modeled as,

$$\mathbf{X}_{msc}(t) = \alpha(t) \int_{\phi} \mathbf{v}\left(\frac{D}{\lambda}\sin\phi, \frac{2v_a T_r}{\lambda}\sin(\phi+\phi_a)\right) d\phi, \tag{2.17}$$

where v_a is the radar's platform velocity and ϕ_a is the misalignment between the array axis and platform velocity vector.[2] The amplitude factor $\alpha(t)$ is typically considered to be a white Gaussian random variable with square root variance that is inversely proportional to the range index, t. As such, MSC is uncorrelated from sample to sample. It is, however, correlated in space and Doppler. When there is no platform misalignment, the energy of the clutter returns is focused on a ridge in the azimuth-Doppler spectrum having slope

$$\beta = \frac{2v_a T_r}{D}. \tag{2.18}$$

For maximum unambiguous platform velocity the clutter ridge has a slope of 1 as shown in Fig. 2.5.

The most complicated form of interference considered, and by far the most difficult to model, is coherent multipath commonly referred to in the radar literature as *terrain scattered interference* (TSI). Just as the radar's transmitted signal reflects from the surrounding terrain to form a composite clutter signal at the aperture, so too can the jammer signal reflect from the surrounding terrain to form TSI as illustrated in Fig. 2.6. Such interference can be intentional or a result of the poor sidelobe

[2]for a more complete model, incorporating an elevation parameter, see [66].

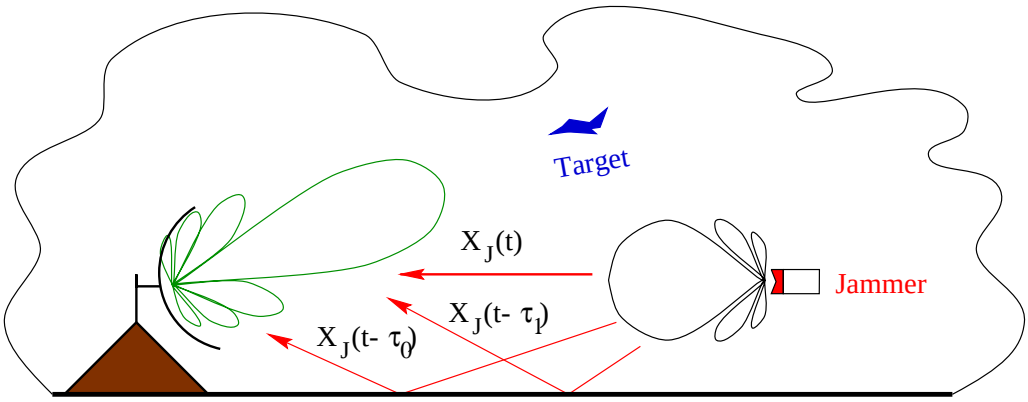

Figure 2.6: Terrain Scattered Interference.

behavior that is characteristic of barrage noise jammers. The delayed and scaled jammer reflections integrate at the aperture to form the composite TSI signal. Since the multipath components integrate over a wide angular extent and at varying delays, the TSI signals at the array elements possess strong spatio-temporal correlation. The terrain surface can be interpreted as a linear time-invariant spatio-temporal filter, $h(t, \nu)$ [31, 34], and, as such, the composite TSI signal may be expressed as

$$\mathbf{X}_{tsi}(t) = \int_{\nu=-0.5}^{0.5} \int_{\tau=0}^{\infty} h(\tau, \nu) \mathbf{x}_j(t-\tau) \otimes \mathbf{a}(\nu) d\tau d\nu, \tag{2.19}$$

where $\mathbf{x}_j(t)$ is an $M \times 1$ vector whose components are shifted versions of jammer signal, $x_j(t)$, at multiples of the PRI interval,

$$\mathbf{x}_j(t) = \left[\begin{array}{cccc} x_j(t) & x_j(t-T_r) & \cdots & x_j(t-(M-1)T_r) \end{array} \right]^T. \tag{2.20}$$

Typically, multipath components fade for sufficiently large delays, and, therefore, the TSI signal is uncorrelated from PRI to PRI and, thus, in Doppler. When the radar or jammer is moving, then Doppler shifts are induced in the reflected multipath, and a more complicated, time-varying, model must be employed, such as the one in [28].

2.3 Adaptive Processing

The output of a linear time-invariant processor can be expressed as the inner product of weight vector, $\mathbf{W}$, and input vector, $\mathbf{Y}(t)$ [66]:

$$z(t) = \mathbf{W}^H \mathbf{Y}(t). \tag{2.21}$$

The vector quantity $\mathbf{Y}(t)$ represents the input to the processor and is defined according to the type of processing employed. The simplest type of processing that can be performed on the data is nonadaptive spatial processing, also known as conventional processing or beamforming. In conventional spatial processing, $\mathbf{W} = \mathbf{a}(\nu_0)$ is the spatial steering vector defined in (2.11), and $\mathbf{Y}(t) = \mathbf{x}^{(m)}(t)$ is a spatial snapshot.

Adaptive processing represents a more sophisticated class of processors and typically requires solving for a set of weights, $\mathbf{W}$, that is optimal in the mean square sense. In other words, the mean square output of the processor,

$$\zeta = \mathrm{E}\left\{|z(t)|^2\right\} = \mathbf{W}^H \mathbf{R}_\mathbf{Y} \mathbf{W}, \tag{2.22}$$

is minimized with respect to $\mathbf{W}$ subject to the constraints $\mathbf{C}\mathbf{W} = \mathbf{c}$ [29]. The covariance matrix, $\mathbf{R}_\mathbf{Y}$, representing the interference environment in the subspace occupied by the input vector, is defined as the expected value [49] of the outer-product of the input vector,

$$\mathbf{R}_\mathbf{Y} = \mathrm{E}\left\{\mathbf{Y}(t)\mathbf{Y}(t)^H\right\}. \tag{2.23}$$

Note that stationary statistics must be assumed, otherwise the covariance matrix itself is time-varying. The solution can be expressed in closed form as [29]

$$\mathbf{W} = \mathbf{R}_\mathbf{Y}^{-1}\mathbf{C}^H \left(\mathbf{C}\mathbf{R}_\mathbf{Y}^{-1}\mathbf{C}^H\right)^{-1} \mathbf{c}. \tag{2.24}$$

In the case of spatial adaptive processing, $\mathbf{Y}(t)$ is a spatial snapshot $\mathbf{x}^{(m)}(t)$. For such processing, the constraints, $\mathbf{C}$ and $\mathbf{c}$, are typically selected so as to satisfy a unity gain condition at the look direction frequency, $\nu_0 = \frac{D}{\lambda}\sin(\phi_0)$, (i.e., $\mathbf{W}^H\mathbf{a}(\nu_0) = 1$),

$$\mathbf{C} = \mathbf{a}(\nu_0)^H, \qquad \mathbf{c} = 1. \tag{2.25}$$

The resultant processor is typically referred to as a minimum variance beamformer [29]. Later in the thesis additional constraints will be considered, including null constraints where some values of the vector $\mathbf{c}$ are zero.

In practice, the covariance matrix $\mathbf{R_Y}$ is not known a priori and, must, therefore be estimated. Substitution of the maximum-likelihood estimate, $\hat{\mathbf{R}}_\mathbf{Y}$, of the covariance matrix $\mathbf{R_Y}$ in Eq. (2.24) results in a technique known as sample matrix inversion (SMI) [52]. The sample covariance matrix is defined as

$$\hat{\mathbf{R}}_\mathbf{Y} = \frac{1}{N_L} \sum_{t=0}^{N_L-1} \mathbf{Y}(t)\mathbf{Y}(t)^H, \tag{2.26}$$

where N_L is the number of snapshots employed in the averaging. The number of statistically independent sample outer products must be at least the dimension of the adaptive weight vector in order for the covariance matrix to have full rank, and, thus, be invertible. Typically, N_L is selected to be twice the dimension of the weight vector so that performance is within 3 dB of optimum [4].

Since the nature of the interference is such that the covariance matrix rarely attains full rank, even with the required number of samples in the estimate, the resulting covariance matrix must be induced to have full rank by artificial means. A technique known as diagonal loading is typically employed together with SMI in order to artificially boost the lower eigenvalues [9]. Diagonal loading is accomplished by adding to the covariance matrix a matrix having σ_d^2 as its diagonal elements and zeros elsewhere,

$$\hat{\mathbf{R}} \rightarrow \hat{\mathbf{R}} + \sigma_d^2 \mathbf{I}, \tag{2.27}$$

where $\mathbf{I}$ is a diagonal matrix of ones. By selecting the diagonal loading level to be that of the noise floor, the matrix inverse is made robust to numerical precision errors, and the covariance matrix produces less "noisy" weights at negligible sacrifice to mitigation performance [19, 31].

2.4 Space-Time Processing

As mentioned earlier, the radar under consideration samples data in space, fast-time, and slow-time and, as such, has available to it three processing dimensions. The three processing dimensions allow discrimination of targets in angle, range, and Doppler. Simultaneous processing of samples in all three dimensions represents the most general class of processors. However, under many circumstances it is sufficient to process only a subset of samples taken from one or more dimensions. Such processing is referred to as reduced rank processing and is typically accompanied by a considerable savings in computation, particularly, when adaptive processing is considered. Therefore, reduced rank algorithms have been the focus of much past and current research in radar signal processing and play a key role in this research as well. This section reviews some of the common multidimensional processing techniques that exploit partially or fully the available dimensionality of the sampling space.

2.4.1 SFT Processing

The adaptive formulation of (2.24) applies to multi-dimensional processing as well as to spatial processing. In the case of space/fast-time (SFT) processing, the input vector in (2.24) is an SFT snapshot $\mathbf{X}_T^{(m)}(t)$ as defined in (2.9) and depicted in Fig. 2.4, where T is the number of fast-time taps employed. Figure 2.7 illustrates SFT processing being performed on the returns of a single pulse. Weights are applied to all element data from T consecutive taps which are then summed together to form an output. Note that a spatial adaptive processor is realized for $T = 1$. For M pulses, M separate SFT filters are applied to their respective pulse, followed by nonadaptive Doppler filtering.

The constraints, $\mathbf{C}$ and $\mathbf{c}$, are typically selected so as to satisfy two sets of conditions at the look direction frequency, $\nu_0 = \frac{D}{\lambda}\sin(\phi_0)$: namely, unity gain at the first tap and zero gain at successive taps. The latter constraints are known as

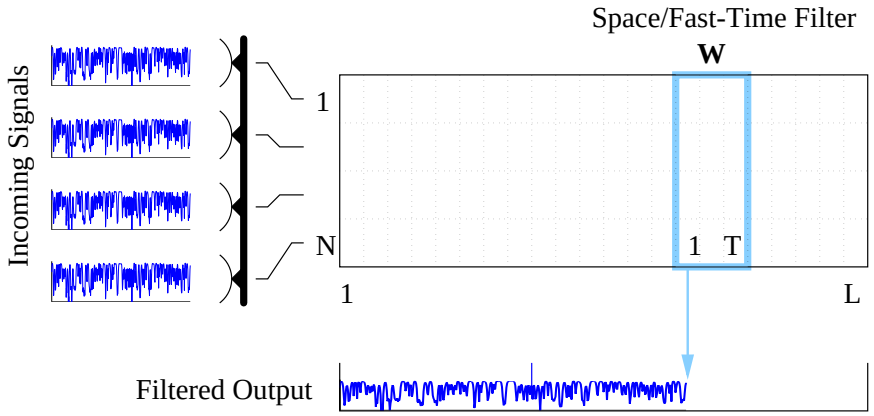

Figure 2.7: Space/fast-time processing.

range constraints or *null constraints*, and their purpose is to prevent target spreading in successive range cells. This is of particular importance when the transmitted waveform is to be matched filtered on return, where any spreading of the LFM coded waveform ultimately results in reduced gain in the matched filters. The constraint quantities are given as follows

$$\mathbf{C} = \mathbf{I}_T \otimes \mathbf{a}(\nu_0)^H \qquad \mathbf{c} = \delta_T, \tag{2.28}$$

where $\mathbf{I}_T$ is the $T \times T$ identity matrix, and $\delta_T = \begin{bmatrix} 1 & 0 & \cdots & 0 \end{bmatrix}^T$ is a $T \times 1$ impulse vector. The resulting set of weights has the desirable property that a target in the look direction passes through the processor undistorted. A similar construction was offered in [21], where a generalized sidelobe canceler architecture realized both a unity gain constraint at the center tap and a set of null constraints at the target look direction for the remaining taps.

Space/fast-time processing has been applied to TSI mitigation as discussed in [31, 34, 13, 22, 23]. In particular the SFT formulation of (2.24) and (2.28) has been shown to offer improved characteristics and performance over reduced rank SFT techniques, such as the single-reference beam canceler [31, 34]. The operation of this processor is based on the principle that the direct path jammer can be used to predict and, thus, cancel the delayed jammer reflections from the ground (i.e., TSI)

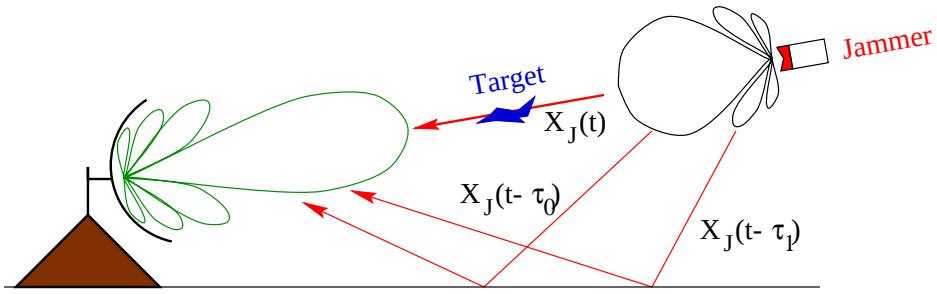

Figure 2.8: Mainbeam jamming scenario with TSI present.

present in the mainbeam.

Mainbeam jamming occurs when the jammer signal is directly impinging on the radar's receive beam, obscuring targets that fall in its path [55]. Spatially adaptive processing works well when target and jammer are adequately separated in angle. However, as the separation diminishes until target and jammer both appear within the mainbeam, performance degrades. This degradation is most severe when the target and jammer are co-aligned and the spatially adaptive processor is unable to achieve any cancelation at all. The problem of using a spatially adaptive processor is further compounded in that its beampattern can become very distorted in the presence of mainbeam jamming. In [31, 33, 32, 37] it was demonstrated that the coherent multipath or TSI could be exploited to improve significantly mainbeam jamming interference mitigation performance. In an ideal setting, as depicted by Fig. 2.8, delayed and scaled replicas of the jammer signal arriving at the radar aperture can be used to reconstruct the jammer signal in the mainbeam and, thus, cancel it.

Conceptually, the function of the SFT processor is to isolate the multipath components and align them coherently with the jammer so that they may be subtracted from the mainbeam where the jammer resides. In reality, the reflecting ground surface produces a continuum of delayed and scaled replicas of the jammer signal (i.e., distributed multipath). The discrete processor can then only approximate the continuous filtering action performed by the terrain that produces the TSI from the jammer signal, and, therefore, exact reconstruction and cancelation is not feasible. However,

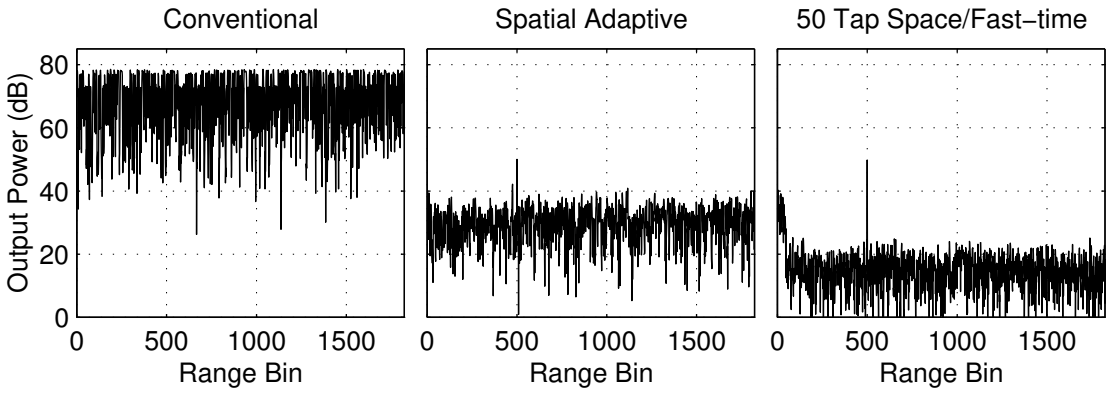

Figure 2.9: Mainbeam jamming mitigation using conventional, spatial adaptive, and SFT processing. The processed data contains a 50 dB target in range cell 500.

performance results on Mountaintop data[3] show remarkable improvement in mainbeam jamming mitigation performance using SFT adaptive processing over spatial processing, as Fig. 2.9 demonstrates.

2.4.2 MSC Mitigation

While SFT processing is useful for mitigating TSI, STAP is useful for cancelling MSC [66, 67, 59]. STAP exploits the space-Doppler correlation in the MSC to null it, while emphasizing the target. Fully adaptive STAP entails applying a set of weights to all element and pulse data at one range cell and summing the weighted samples to form an output [17, 7, 66]. As such, the input vector in (2.24) is a slow-time snapshot, $\mathbf{Y}(t) = \mathbf{X}(t)$, as defined in (2.8) and depicted in Fig. 2.4. A unity gain constraint in the look direction frequency pair $(\nu_0, \bar{f}_0)$ is typically selected resulting in the weights

$$\mathbf{W} = \frac{\mathbf{R}_{\mathbf{X}}^{-1}\mathbf{v}_0}{\mathbf{v}_0^H \mathbf{R}_{\mathbf{X}}^{-1}\mathbf{v}_0}, \tag{2.29}$$

where $\mathbf{v}_0 = \mathbf{v}(\nu_0, \bar{f}_0)$.

As an alternative, partially adaptive STAP architectures [66, 67, 1, 12, 64] have become widely popular in that they have demonstrated under most circumstances

[3]The Mountaintop experiment is described in Sec. 4.4.

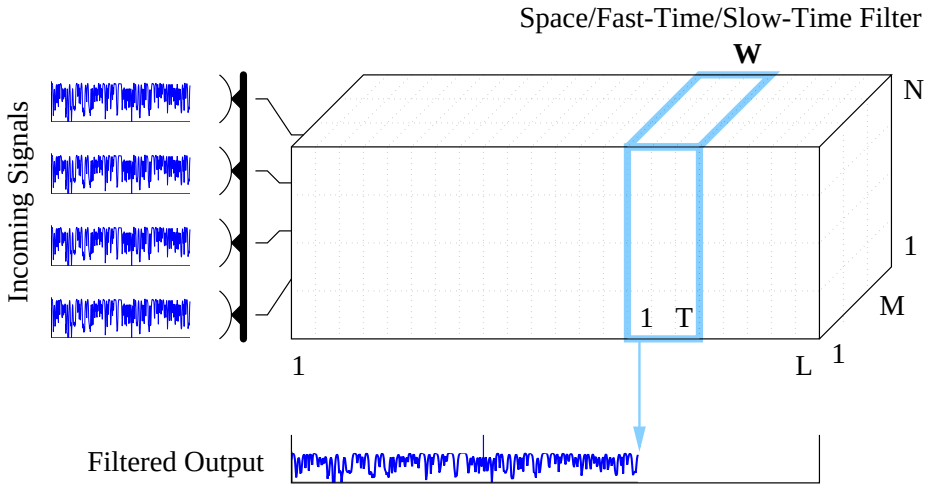

Figure 2.10: Three-dimensional processing.

near equivalent performance to the fully adaptive STAP architecture.

2.4.3 Joint TSI and MSC Mitigation

When TSI and MSC are both present in the radar returns, STAP and SFT processing are each effective only for one interference type and not the other. Thus, a joint cancelation of MSC and TSI must take place in the element, PRI, and fast-time domain [16]. Figure 2.10 illustrates the filtering mechanism for a full rank three-dimensional processor. Weights from all elements and PRIs are applied to a number of taps and are summed together to form the output. Given N elements, M PRIs, and T taps, the optimal solution has a computational complexity on the order of $O[(NMT)^3]$ and a sample support requirement on the order of $O[NMT]$. Thus, both processing and sample support requirements become prohibitive for even a small array.

A reduced rank solution proposed in [31, 36], the factored beamspace algorithm (FBA), computes a TSI processor for each of N orthogonal directions and M pulses, which are used to remove the TSI from the data returns while preserving the spatial and temporal dimensionality of the data. The filtered data is then fed into a second

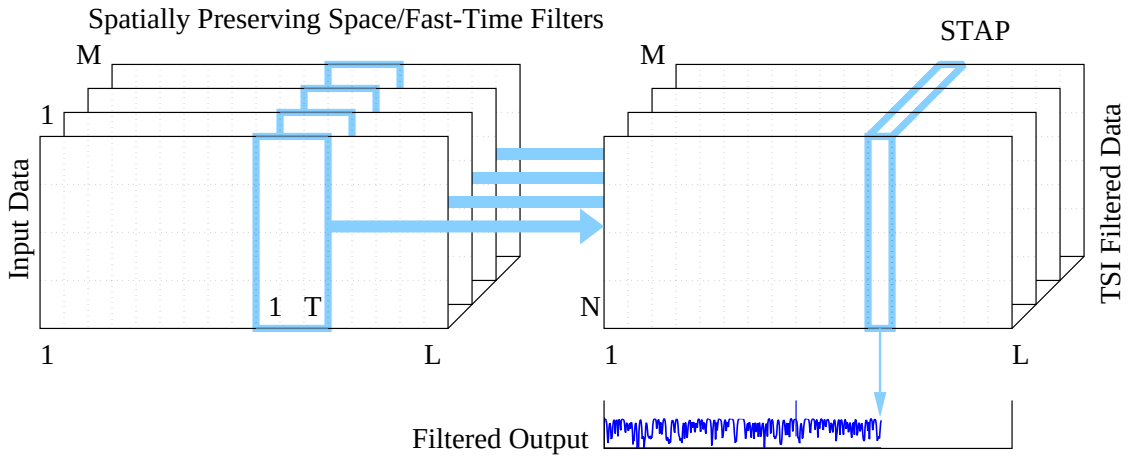

Figure 2.11: Factored Beamspace Algorithm.

stage, a STAP processor, which serves to remove the remaining MSC. Figure 2.11 illustrates the filtering mechanism of the FBA.

The set of MN weight vectors in the first stage are given by,

$$\mathbf{W}_{m,n} = \mathbf{R}^{-1}_{\mathbf{x}^{(m)}_T} \mathbf{C}^H_n \left(\mathbf{C}_n \mathbf{R}^{-1}_{\mathbf{x}^{(m)}_T} \mathbf{C}^H_n \right)^{-1} \mathbf{c}, \tag{2.30}$$

where $\mathbf{R}_{\mathbf{x}^{(m)}_T}$ is the $NT \times NT$ "TSI only" covariance matrix of the m^{th} PRI ($m \in \{0, 1, \cdots, M-1\}$), $\mathbf{C}_n = \mathbf{I}_T \otimes \mathbf{a}\left(\frac{n}{N}\right)^H$ is the constraint matrix associated with the n^{th} orthogonal direction ($n \in \{0, 1, \cdots, N-1\}$), and $\mathbf{c}$ is the constraint vector defined earlier in (2.28). In estimating the covariance matrix for the TSI filtering stage, far range samples containing little or no MSC must be used in order that the TSI filters do not attempt spatial suppression of the MSC [31, 36]. Any spatial suppression of the MSC in the first stage will detract from the TSI cancellation power of the TSI filters and can also cause severe target cancellation. The spatially preserved data output of the m^{th} PRI from the first stage is given by

$$\tilde{\mathbf{X}}^{(m)}(t) = \mathbf{W}^H_m \mathbf{X}^{(m)}_T(t), \tag{2.31}$$

where $\mathbf{W}_m = \begin{bmatrix} \mathbf{W}_{m,0} & \mathbf{W}_{m,1} & \cdots & \mathbf{W}_{m,N-1} \end{bmatrix}$ is a weight matrix comprised of the set of weight vectors for the m^{th} PRI in N orthogonal directions.

In anticipation of STAP processing at the second stage, it is necessary to modify the space-Doppler steering vector used with the STAP processor to reflect the transformation undergone by the target in the TSI filtering stage (similar to the transformation undergone by the spatial steering vector in the two-step nulling algorithm in [43]),

$$\tilde{\mathbf{v}}(\nu_0, \bar{f}_0) = \left(\mathbf{b}(\bar{f}_0) \otimes \mathbf{1}_N\right) \odot \left(\begin{bmatrix} \mathbf{W}_0 & \mathbf{W}_1 & \cdots & \mathbf{W}_{N-1} \end{bmatrix}^H \mathbf{a}(\nu_0) \otimes \delta_M \right), \tag{2.32}$$

where $\mathbf{1}_N$ is an $N \times 1$ vector of ones and $\odot$ denotes the Hadamard product [27] (i.e., an element-wise matrix product operator). STAP weights for the second stage are computed with a unity gain look direction constraint using the modified steering vector,

$$\tilde{\mathbf{W}} = \frac{\mathbf{R}_{\tilde{\mathbf{X}}}^{-1} \tilde{\mathbf{v}}_0}{\tilde{\mathbf{v}}_0^H \mathbf{R}_{\tilde{\mathbf{X}}}^{-1} \tilde{\mathbf{v}}_0}, \tag{2.33}$$

where $\mathbf{R}_{\tilde{\mathbf{X}}}$ is the $MN \times MN$ covariance matrix of the SST snapshot of the filtered data, and $\tilde{\mathbf{v}}_0 = \tilde{\mathbf{v}}(\nu_0, \bar{f}_0)$. The processor output is

$$z(t) = \tilde{\mathbf{W}}^H \tilde{\mathbf{X}}(t). \tag{2.34}$$

2.5 Performance Analysis

In analyzing processor performance it is useful to consider such quantifiable measures as interference power and target power. Comparing these quantities at the input and output of the radar processor indicates how well the radar processor is doing its job of removing interference and enhancing the target. As mentioned earlier, all power measurements are referenced to the thermal noise in the system, or noise floor. For a given radar system, the noise floor is fixed at σ_n^2 and is usually expressed in decibels, $N_f = 10 \log_{10}(\sigma_n^2)$, which for the radar under consideration is 50 dB.

2.5.1 Mitigation Performance

The signal-to-noise ratio (SNR) is defined as

$$\text{SNR} = \frac{\text{E}\left\{\mathbf{X}_{tgt}^H \mathbf{X}_{tgt}\right\}}{\sigma_n^2} = \frac{\sigma_t^2}{\sigma_n^2}. \tag{2.35}$$

The input interference-to-noise ratio (INR) is defined as

$$\text{INR} = \frac{\text{E}\left\{\mathbf{X}_i^H \mathbf{X}_i\right\}}{\sigma_n^2} = \frac{\text{Tr}\left[\mathbf{R}_i\right]}{\sigma_n^2}, \tag{2.36}$$

where $\mathbf{R}_i$ is the interference covariance matrix, and Tr denotes the trace function, which sums the elements on the diagonal of the covariance matrix [29]. The output interference-to-noise ratio (OINR) is defined as

$$\text{OINR} = \frac{\text{E}\left\{|z_i|^2\right\}}{\sigma_n^2} = \frac{\mathbf{W}^H \mathbf{R}_i \mathbf{W}}{\sigma_n^2}, \tag{2.37}$$

where z_i is the output of the processor when only interference is present and $\mathbf{W}$ is the weight vector projected onto the space spanned by the covariance matrix. Cancellation or mitigation performance can be reported in any number of ways. When comparing processors, it is most straightforward to compare them on the basis of OINR, although sometimes the *interference rejection ratio*, which is the ratio of OINR to INR, is more revealing. In either case, the processors under consideration must pass the target with unity gain (i.e., no target cancellation should occur). Otherwise, a comparison of OINR or interference rejection alone is not meaningful. For a standard adaptive processor of the form (2.24), a unity gain constraint in the look direction and Doppler is sufficient to prevent target cancellation. For a more complicated, multistage processor such as the factored beamspace algorithm, a different normalization scheme is necessary.

2.5.2 Burnthrough

Sometimes it is convenient to speak of burnthrough in relating the performance of a conventional processor to that of an adaptive processor. Burnthrough is a technique

based on averaging that is often employed to boost SNR in the presence of strong interference through a prolonged dwell period [54]. The concept is that successive echos from a target integrate coherently, whereas the noise components integrate incoherently [61]. Let $n = \sum_{i=1}^{M} n_i$ be the integrated noise component and $t = \sum_{i=1}^{M} t_i$ be the integrated target component. The average power of each noise sample, n_i, is σ_n^2 and that of each target sample, t_i, is σ_t^2. Assuming that the noise is uncorrelated from pulse to pulse, the total noise power is given by

$$P_n = \mathrm{E}\left\{n \cdot n^*\right\} = \sum_{i=1}^{M} \mathrm{E}\left\{|n_i|^2\right\} = M\sigma_n^2, \tag{2.38}$$

and that of the target is

$$P_t = \mathrm{E}\left\{t \cdot t^*\right\} = \sum_{i=1}^{M}\sum_{j=1}^{M} \mathrm{E}\left\{t_i t_j^*\right\} = M^2\sigma_t^2. \tag{2.39}$$

For one pulse the SNR is, $S_1 = \sigma_t^2/\sigma_n^2$, whereas for M pulses it is

$$S_M = M\sigma_t^2/\sigma_n^2 = MS_1. \tag{2.40}$$

Expressed in decibels, $S_M^{dB} - S_1^{dB} = 10\log_{10} M$, or

$$M = 10^{(S_M^{dB} - S_1^{dB})/10}. \tag{2.41}$$

For instance, a boost of 50 dB in SNR (i.e., $S_M^{dB} - S_1^{dB} = 50$) requires an increase in dwell time of $M = 100,000$. In practice the dwell time dictated by the conventional processor places an unrealistic demand on the radar, since it diminishes from the radar's ability to focus on other targets [61]. Furthermore, a moving radar or target can limit the effectiveness of burnthrough by diminishing the target's integrated power across pulses. In such cases, the merit of the adaptive processor over the conventional processor becomes evident from the reported burnthrough time that is necessary to detect a given target.

2.6 Summary

This chapter began by introducing some preliminary concepts in array processing and radar. A discussion of modern pulsed array radar followed, focusing on available processing dimensions and the interference environment in which such a radar operates. Mathematical models describing the various forms of interference were presented to motivate specific classes of adaptive processing techniques suitable for handling such interference. In particular, space/fast-time processing was shown to be beneficial for TSI and mainbeam jamming mitigation, STAP for monostatic clutter mitigation, and three-dimensional processing techniques such as the factored beamspace approach for combined MSC and TSI. The chapter concluded with a framework for evaluating mitigation performance. Additional information on topics covered here is available in the general literature. See

- [29, 42] for array processing,
- [61, 48, 54] for topics in radar, and
- [66] for space-time processing.

CHAPTER 3

Monopulse

Ranging and direction finding are essential operations for almost any radar system. Whereas the previous chapter briefly discussed the concept of ranging, this chapter focuses on direction finding. Both surveillance and tracking radars require some form of direction finding or angle discrimination capability. In surveillance radars angle discrimination is employed to map out targets from different angular sectors. Whereas, in tracking radars angle discrimination is employed to isolate and fix on a single target for tracking purposes, often to guide a missile.

Direction finding in surveillance radars, which requires broad spatial coverage, is typically implemented with a rotating antenna dish that transmits pulses and receives echos throughout the rotation cycle. The approximate angular location of a target is indicated by the pointing direction of the antenna mainbeam at the time of detection. The angular resolution (i.e., minimum angle separation necessary to resolve two targets) that can be achieved is ultimately bounded by the Rayleigh Criterion, which places the limit at the half power beamwidth of the antenna's diffraction pattern [53]. As a result, tracking radars, which require high angular resolution and only narrow angular coverage, must employ alternative techniques, such as beam switching or conical scanning together with range gating (separation by range), to overcome these inherent resolution limitations. Beam switching or lobe switching employs two rapidly switching beampatterns to illuminate a target, and, thereby, provide slightly different perspectives of the target for angle discrimination [60, 53].

In conical scanning the antenna dish rotates narrowly about boresight illuminating a narrow cone-like region of the target space [60, 53]. Hence, a target that is offset from boresight is modulated by the rotational frequency of the antenna. The modulation amplitude of the echo corresponds to the target's radial distance from boresight and the phase of the envelope peak indicates the target's angular position about the cone's rim. The latter technique is particularly useful for three dimensional direction finding.

All of the *sequential lobing* techniques, mentioned thus far, rely on the comparison of sequential pulses and, as a result, suffer degradation due to *target scintillation* (i.e., rapid fluctuations of a target's cross sectional area caused by essentially random factors) [53, 60]. Early in the history of radar it was recognized that rather than transmitting multiple pulses sequentially, a single pulse could be transmitted and received simultaneously on two slightly displaced apertures to achieve the same effect: namely, the projection of two separate spatial realizations of the target echo on the antenna element. This technique became known as *monopulse* since it works with only one transmitted pulse.

3.1 Monopulse Fundamentals

Assuming that the amplitude of a target's echos from repeated pulse transmissions remains relatively constant, it is possible to obtain an accurate angle measurement of the echoing source by comparing the amplitudes of successive echos as they are received on two slightly offset beams as shown in Fig. 3.1. In practice, however, echo strengths change rapidly from one transmission to the next, and, hence, the constant amplitude assumption is not realistic. The idea behind monopulse is to compare the amplitudes of two simultaneous projections of an echo (V_0, V_1) on two displaced receive beams, as shown in Fig. 3.2. The echo projects on the receive beams in a manner that is dependent on its angle of arrival. Thus, amplitude and phase components that

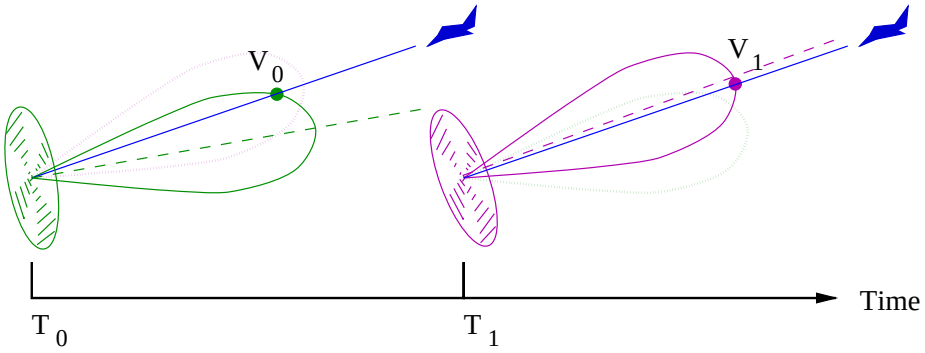

Figure 3.1: Sequential lobing example.

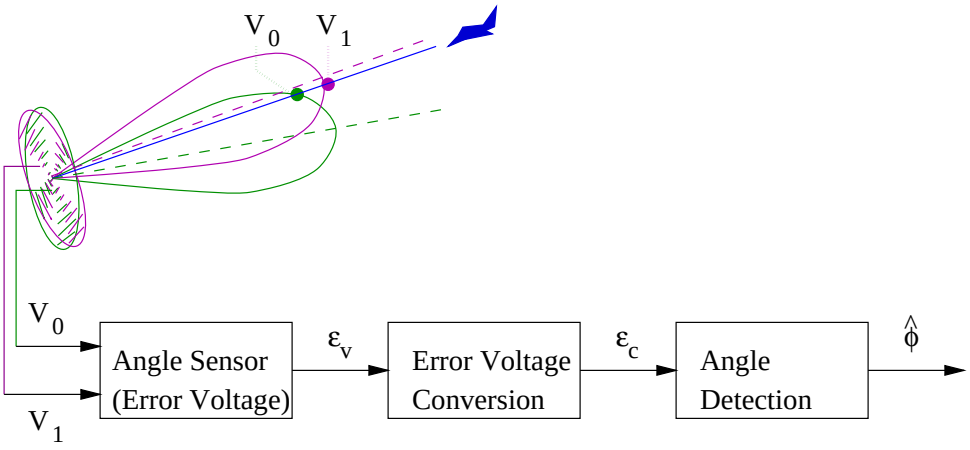

Figure 3.2: Simultaneous lobing example – monopulse.

depend on angle of arrival are different for V_0 and V_1. On the other hand, amplitude and phase components caused by factors that are external to the radar, such as target range, target cross-section, and medium losses, appear identically in both V_0 and V_1. By considering a ratio of the voltages, the components that appear identically in the two voltages cancel out, while the angle dependent components are retained,

$$\epsilon_v = f\left(\frac{V_0}{V_1}\right). \tag{3.1}$$

The quantity ϵ_v, called the *error voltage*, conveys purely directional information, and, although it does not convey the information directly in angular form, it can be converted to angular form via a mapping function. The mapping function, called a *monopulse response curve* (MRC), is given in terms of the ratio of the two receive beampattern functions because the beampattern functions represent the ideal response of the antenna to targets across angle,

$$\mathcal{M} = f\left(\frac{\mathcal{W}_0}{\mathcal{W}_1}\right). \tag{3.2}$$

If the receive beampattern functions, $\mathcal{W}_0$ and $\mathcal{W}_1$, are designed properly, then this mapping is invertible for a given angular region about the boresight angle, and, thus, given an error voltage reading a corresponding angle can be found. The exact form of the function $f(\cdot)$ that appears in the error voltage and MRC definitions depends on the monopulse system employed and typically serves to make the error voltage function real-valued, as will be specified further on.

Monopulse is not restricted to *amplitude comparison* as discussed in the example. The differences among various monopulse implementations manifest themselves primarily in the way in which angle information is conveyed. Since in amplitude comparison monopulse only amplitude information is considered, the beams must be offset in angle as shown on the top left of Fig. 3.3 [38, 53]. Note that phase is discarded in the angle sensor. For the configuration shown, angle estimation can only take place within a narrow region about boresight but with higher accuracy than afforded by the Rayleigh criterion. The useful monopulse region can be increased

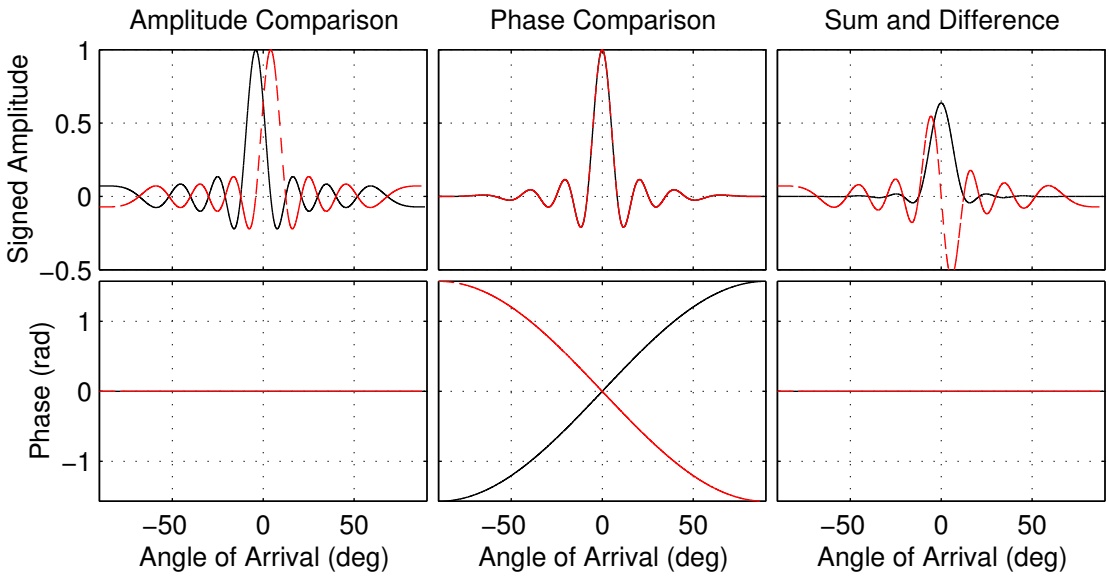

Figure 3.3: Beampatterns for three types of monopulse.

by separating the beams farther, but accuracy in turn degrades. In contrast, *phase comparison monopulse* utilizes only phase information, and, thus, the beampatterns have identical shapes and pointing directions, but with mirroring phase functions [38, 53]. Although the phase functions shown in Fig. 3.3 are continuous in the entire 180° range, typically the phase functions wrap around a number of times throughout this range, permitting angle estimation to take place in only a narrow region about boresight, but, again, with increased accuracy. Most commonly considered is *sum and difference monopulse*. In Fig. 3.3 the sum beam (solid-black) is formed by summing the displaced beams of the amplitude comparison monopulse, whereas the difference beam (dashed-red) is formed by taking their difference [53, 60]. Note that the sum beam peaks at boresight whereas the difference beam has a null at boresight.

In the block diagram of Fig. 3.2 the angle sensor stage feeds first into an error voltage conversion stage and then into an angle detection stage. The angle sensor stage corresponds to taking an error voltage measurement, whereas the angle detection stage corresponds to mapping the error voltage to an angle measurement via an MRC. In traditional hardware based monopulse systems an additional intermediate conversion stage is often necessary because the angle sensor hardware is of one type and the angle detector hardware of another [53]. For instance, the output of an amplitude comparison angle sensor might need to be converted for use with a phase or sum and difference angle detector.

3.2 Monopulse with Sensor Arrays

The monopulse technique utilizes signals from multiple apertures to estimate angle of arrival in one or two angular planes. Since phased arrays can easily form multiple, simultaneous apertures, the monopulse technique naturally extends to them. In the previous discussion the monopulse apparatus consisted of two displaced apertures. The geometrical misalignment or displacement of the aperture feeds gave rise to

beampatterns that were offset in angle or phase, thus allowing two independent spatial realizations of the target echo to be obtained. With a phased array the number of independent spatial realizations that can be obtained is the element count, and, thus, the array might at first glance seem redundant for the purpose of monopulse. However, as will be seen later, the additional spatial degrees of freedom afforded by the array can be utilized for spatial nulling of interference sources.

In phased arrays beamforming is typically performed electronically by either hardware or software. Beamforming at the software level is particularly amenable to monopulse, because no additional hardware is required for simultaneous beam formation. Since arbitrary beampatterns can be emulated by the array through the application of appropriate phase shifts to the incoming signals, any of the commonly considered monopulse configurations in Fig. 3.3 are possible with a phased array, without modification to the array.

Of particular interest is sum and difference monopulse, which is characterized by a sum pattern that peaks at boresight and a difference pattern that has a null there. It is most straightforward to consider the sum and difference beams to be the sum and difference of two orthogonal steering vectors centered about boresight and separated by a normalized spatial frequency of $\frac{1}{N}$,

$$\mathbf{a}_\Sigma = \frac{\mathbf{a}(\nu_0 + \frac{1}{2N}) + \mathbf{a}(\nu_0 - \frac{1}{2N})}{2}, \qquad \mathbf{a}_\Delta = \frac{\mathbf{a}(\nu_0 + \frac{1}{2N}) - \mathbf{a}(\nu_0 - \frac{1}{2N})}{2}. \tag{3.3}$$

The resulting beampattern responses are shown in Fig. 3.4 (left) and are given by

$$\mathcal{W}_\Sigma(\nu) = \frac{1}{2N}\left[\frac{\sin N\pi\left(\nu - \nu_0 - \frac{1}{2N}\right)}{\sin \pi\left(\nu - \nu_0 - \frac{1}{2N}\right)} + \frac{\sin N\pi\left(\nu - \nu_0 + \frac{1}{2N}\right)}{\sin \pi\left(\nu - \nu_0 + \frac{1}{2N}\right)}\right] \tag{3.4}$$

$$\mathcal{W}_\Delta(\nu) = \frac{1}{2N}\left[\frac{\sin N\pi\left(\nu - \nu_0 - \frac{1}{2N}\right)}{\sin \pi\left(\nu - \nu_0 - \frac{1}{2N}\right)} - \frac{\sin N\pi\left(\nu - \nu_0 + \frac{1}{2N}\right)}{\sin \pi\left(\nu - \nu_0 + \frac{1}{2N}\right)}\right]. \tag{3.5}$$

By another method, the sum weights are taken to be a steering vector in the look direction, and the difference weights are obtained by phase reversing the latter half of the components of the steering vector

$$\mathbf{a}_\Sigma = \mathbf{a}(\nu_0), \qquad \mathbf{a}_\Delta = -j\mathbf{t}_d \odot \mathbf{a}(\nu_0), \tag{3.6}$$

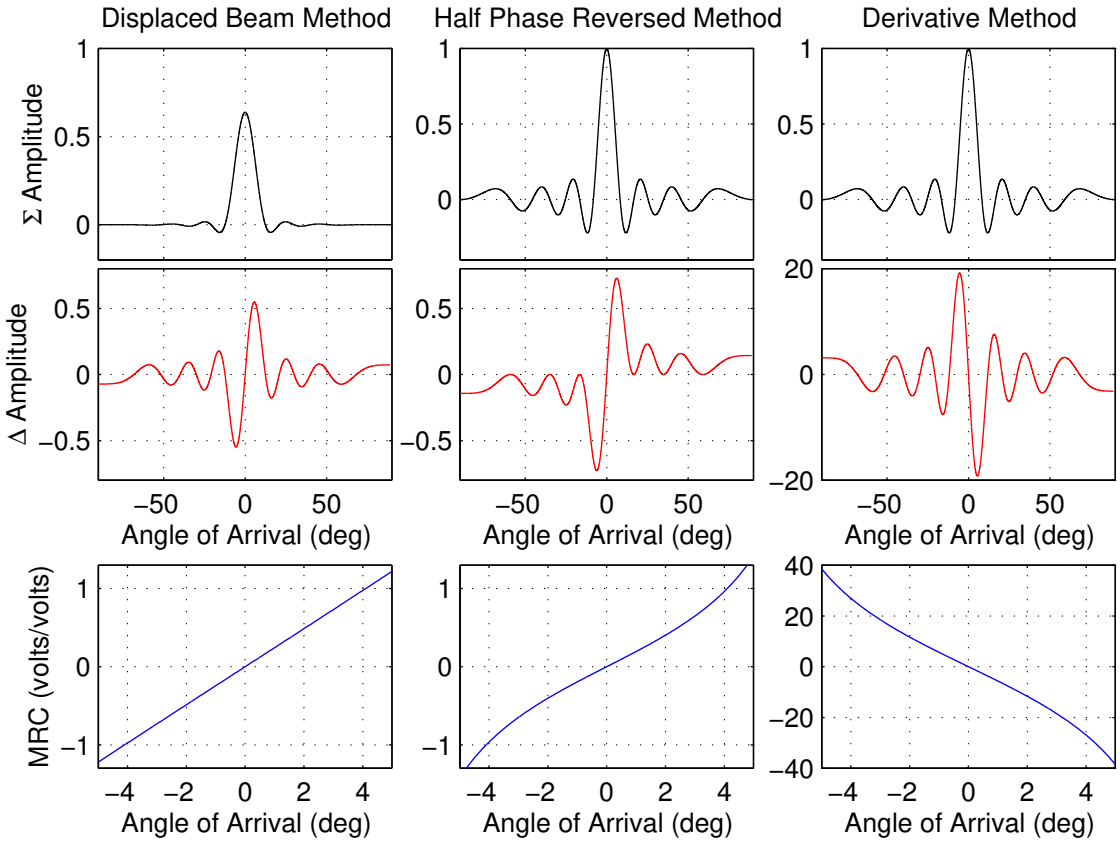

Figure 3.4: Beampatterns and MRCs for three types of sum and difference beams.

where $\mathbf{t}_d = \left[\begin{array}{cc} \mathbf{1}_{1\times\frac{N}{2}} & -\mathbf{1}_{1\times\frac{N}{2}} \end{array} \right]^T$.[1] In this type of difference processor, the outputs from one half of the array elements are subtracted from the other half, a construction similar to the two-horn receiver, where one beam is subtracted from the other [60]. The effect of the phase reversal is to place a null in the look direction, thus splitting the mainlobe in two as illustrated in Fig. 3.4 (center). The sum and difference beam patterns are given by,

$$\mathcal{W}_\Sigma = \frac{1}{N}\frac{\sin N\pi\,(\nu-\nu_0)}{\sin\pi(\nu-\nu_0)}, \qquad \mathcal{W}_\Delta = \frac{2}{N}\frac{\sin^2\frac{N}{2}\pi\,(\nu-\nu_0)}{\sin\pi(\nu-\nu_0)}. \tag{3.7}$$

Yet another method for obtaining sum and difference weights is to take the vector of sum weights to be a steering vector in the look direction and the vector of difference weights to be the derivative of the steering vector with respect to normalized spatial frequency

$$\mathbf{a}_\Sigma = \mathbf{a}(\nu_0), \qquad \mathbf{a}_\Delta = \left.\frac{\partial\mathbf{a}(\nu)}{\partial\nu}\right|_{\nu_0}. \tag{3.8}$$

The sum and difference patterns are shown in Fig. 3.4 (right) and are given by

$$\mathcal{W}_\Sigma = \frac{1}{N}\frac{\sin N\pi\,(\nu-\nu_0)}{\sin\pi\,(\nu-\nu_0)}, \tag{3.9}$$

$$\mathcal{W}_\Delta = \frac{\pi}{2N}\frac{(N-1)\sin(N+1)\pi(\nu-\nu_0)-(N+1)\sin(N-1)\pi(\nu-\nu_0)}{\sin^2\pi(\nu-\nu_0)}. \tag{3.10}$$

Sum and difference processors are denoted by the $N\times 1$ vectors $\mathbf{w}_\Sigma$ and $\mathbf{w}_\Delta$, respectively. Sum and difference outputs are given in terms of the respective processors,

$$z_\Sigma(t) = \mathbf{w}_\Sigma^H\mathbf{x}(t) \qquad z_\Delta(t) = \mathbf{w}_\Delta^H\mathbf{x}(t), \tag{3.11}$$

where $\mathbf{x}(t)$ is the $N\times 1$ spatial snapshot[2] at time instant t, as defined in (2.7). The error voltage was defined earlier as a function of the ratio of two beam outputs. Since

[1] A bold numeral denotes a vector or matrix all of whose elements are that value (i.e., $\mathbf{1}_{2\times 3}$ is a 2×3 matrix of ones, and $\mathbf{1}_2$ is a length-two column vector of ones).

[2] At present, only a single pulse is considered, and, for notational convenience, the superscript (m) from $\mathbf{x}^{(m)}(t)$ denoting pulse index has been dropped.

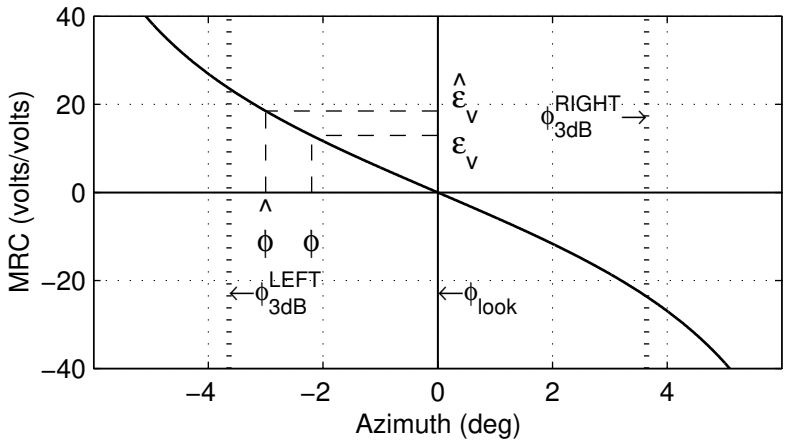

Figure 3.5: Conventional monopulse response curve.

both the antenna patterns and the array sensor outputs can be complex-valued the ratio of beam outputs is in general considered complex. However, for the examples of sum and difference monopulse systems given previously it is evident that only real-valued ratios, z_Δ/z_Σ, correspond to a physical target, and, therefore, the imaginary-part of the ratio should be discarded since it is primarily due to interference. In terms of the error voltage and MRC definitions of (3.1) and (3.2) this corresponds to taking the real part of the ratio (i.e., $f(r) = \Re(r)$)

$$\epsilon_v(t) = \Re\left\{\frac{z_\Delta(t)}{z_\Sigma(t)}\right\}, \qquad \mathcal{M}(\phi) = \Re\left\{\frac{\mathcal{W}_\Delta(\phi)}{\mathcal{W}_\Sigma(\phi)}\right\}. \tag{3.12}$$

It should be noted that for other monopulse system designs where the target information is contained in the phase component (phase comparison monopulse) or imaginary component of the voltage ratio, $f(r) = \angle(r)$ or $f(r) = \Im(r)$ are more appropriate. When working with adaptive processors, a distorted pair of sum and difference beams does not produce a ratio that corresponds to any simple form of $f(r)$, and in such a case the definitions in (3.12) will be used. However, other forms of $f(r)$, such as the absolute value of the ratio [41], may be employed equally well.

Figure 3.5 illustrates the response for the conventional monopulse processor of (3.8) to targets ranging in azimuth from $-5°$ to $5°$. Given an error-voltage measure-

ment, the target azimuth is determined by inverse mapping the error voltage through the MRC:

$$\hat{\phi} = \mathcal{M}^{-1}\left(\hat{\epsilon_v}\right), \tag{3.13}$$

as illustrated in Fig. 3.5. In practice the processor pair $\mathbf{w}_\Sigma$ and $\mathbf{w}_\Delta$ are unable to completely reject interference. The residual interference present in the real component of the ratio, z_Δ / z_Σ, causes the error voltage ϵ_v to deviate from its ideal value as given by the MRC. The corresponding error in the azimuth angle measurement, $\epsilon_\phi = \hat{\phi} - \phi$, is illustrated by the dashed lines in Fig. 3.5. Qualitatively, the flatter the MRC, the greater the resulting error in azimuth reading for a given deviation of error voltage. Therefore, it is desirable to have a "well-sloped" curve such as the one shown in Fig. 3.5. Another desirable property of the conventional processor's MRC is that it be unbiased; that is, the curve passes through the coordinate $(\phi_{look}, 0)$.

3.3 Adaptive Monopulse

In nonadaptive monopulse, a set of fixed sum and difference weights is computed to achieve certain desirable properties, such as low sidelobes, angle sensitivity, robustness, and good performance in thermal noise. The literature contains numerous design procedures for arriving at sum and difference beams that exhibit various trade-offs among the different criteria [50, 3]. For the purpose of the development presented here, it is sufficient to utilize any of the basic sum and difference beams introduced earlier and shown in Fig. 3.4.

3.3.1 Maximum Likelihood Angle Estimation

The disadvantage of conventional monopulse is that it fails to provide adequate suppression of jamming and other forms of interference. Spatial adaptive monopulse has been proposed as an effective means to counter the problem of sidelobe jamming and,

to a limited extent, mainbeam jamming [11]. Several different approaches have been proposed for designing an adaptive pair of sum and difference beams, such as the maximum-likelihood approach in [11], which yields a pair of beams that optimizes a selected angle estimator discussed below.

For the maximum-likelihood (ML) technique a Gaussian probability density function (pdf) was assumed for the signal-plus-noise process. When the spatial frequency (ν) and signal amplitude (σ_t) are unknown the pdf is

$$p(\mathbf{x}|\sigma_t\mathbf{a}(\nu)+\mathbf{n}) = (\pi)^{-N}|\mathbf{R}_\mathbf{x}|^{-1}\exp\left[(\mathbf{x}-\sigma_t\mathbf{a}(\nu))^H\mathbf{R}_\mathbf{x}^{-1}(\mathbf{x}-\sigma_t\mathbf{a}(\nu))\right], \tag{3.14}$$

where $\mathbf{n}$ is a white Gaussian $N\times 1$ noise vector whose components have power σ_n^2, and $|\mathbf{R}_\mathbf{x}|$ is the determinant of the spatial covariance matrix. As shown in [11], the spatial ML frequency estimate $\hat{\nu}$ maximizes the log-likelihood function (i.e., $\arg\max_{\hat{\nu}} \ln p\left(\mathbf{x}|\sigma_t\mathbf{a}(\hat{\nu})+\mathbf{n}\right)$) and satisfies

$$\Re\left\{\frac{z_\Sigma(\hat{\nu},\mathbf{x})z_\Delta^*(\hat{\nu},\mathbf{x})}{|z_\Sigma(\hat{\nu},\mathbf{x})|^2}\right\} = \Re\left\{\frac{\mathrm{E}\left[z_\Sigma(\hat{\nu},\mathbf{x})z_\Delta^*(\hat{\nu},\mathbf{x})\right]}{\mathrm{E}|z_\Sigma(\hat{\nu},\mathbf{x})|^2}\right\}, \tag{3.15}$$

where superscript asterisk (*) denotes the complex conjugate and the sum and difference output functionals, z_Σ and z_Δ, are defined as

$$z_\Sigma(\nu,\mathbf{x}) = \mathbf{a}(\nu)^H\mathbf{R}_\mathbf{x}^{-1}\mathbf{x} \tag{3.16}$$

$$z_\Delta(\nu,\mathbf{x}) = \frac{\partial\mathbf{a}(\nu)^H}{\partial\nu}\mathbf{R}_\mathbf{x}^{-1}\mathbf{x} = \mathbf{a}_\Delta(\nu)^H\mathbf{R}_\mathbf{x}^{-1}\mathbf{x}. \tag{3.17}$$

When the interference noise is isotropic [29] (e.g., white noise and element spacing is $D=\lambda/2$) then (3.15) reduces to the standard monopulse criterion [11]

$$\Re\left\{\frac{z_\Delta(\hat{\nu},\mathbf{x})}{z_\Sigma(\hat{\nu},\mathbf{x})}\right\} = 0. \tag{3.18}$$

The simplified form of the ML criterion in isotropic noise (3.18) suggests that performing monopulse is the "best thing to do" under such conditions. On the other hand, for nonisotropic noise interference the standard monopulse criterion does not yield the best angle estimate, but rather (3.15) must be met. Since the general

solution to (3.15) is nonlinear, computing it can be difficult. However, by making certain assumptions and simplifying approximations, Davis et al. [11] were able to arrive at closed form solutions to the ML estimator. Note that nonisotropic noise and interference, including barrage noise jammers, MSC, and TSI, prevent conventional monopulse processing and ML angle estimation from being equivalent. It will be seen later that in such cases adaptive monopulse processing has performance that is very similar to ML estimation.

3.3.2 Linearly Constrained Angle Estimation

Rather than directly optimizing an angle estimator as in Eq. (3.15), it is possible to minimize the interference in the individual sum and difference output channels by employing linearly constrained optimization. The rationale is that when little or no distortion is introduced into the sum and difference mainbeams then the reduced form of the monopulse criterion (3.18) still applies and the performance of this angle estimator will approach that of ML. On the other hand, when distortions are present then the reduced form (3.15) does not apply and a distorted mapping function (i.e., MRC) must be employed to compensate for these distortions.

One realization of conventional monopulse (3.3) employed a sum and difference of squinted beams (i.e., angularly displaced beams). Adaptive monopulse may be realized in a similar manner. Two adaptive beams that have peaks[3] offset by a normalized spatial frequency of $\frac{1}{N}$ are given as follows,

$$\mathbf{w}_1 = \mathbf{R}_{\mathbf{x}}^{-1}\mathbf{a}\left(\nu_0 + \frac{1}{2N}\right), \qquad \mathbf{w}_2 = \mathbf{R}_{\mathbf{x}}^{-1}\mathbf{a}\left(\nu_0 - \frac{1}{2N}\right). \tag{3.19}$$

Adaptive sum and difference beams are realized by summing and subtracting the displaced adaptive beams,

$$\mathbf{w}_\Sigma = \frac{\mathbf{w}_1 + \mathbf{w}_2}{2} = \mathbf{R}_{\mathbf{x}}^{-1}\mathbf{a}_\Sigma, \tag{3.20}$$

$$\mathbf{w}_\Delta = \frac{\mathbf{w}_1 - \mathbf{w}_2}{2} = \mathbf{R}_{\mathbf{x}}^{-1}\mathbf{a}_\Delta, \tag{3.21}$$

[3]When distortions are present then the peaks may drift away from the desired locations.

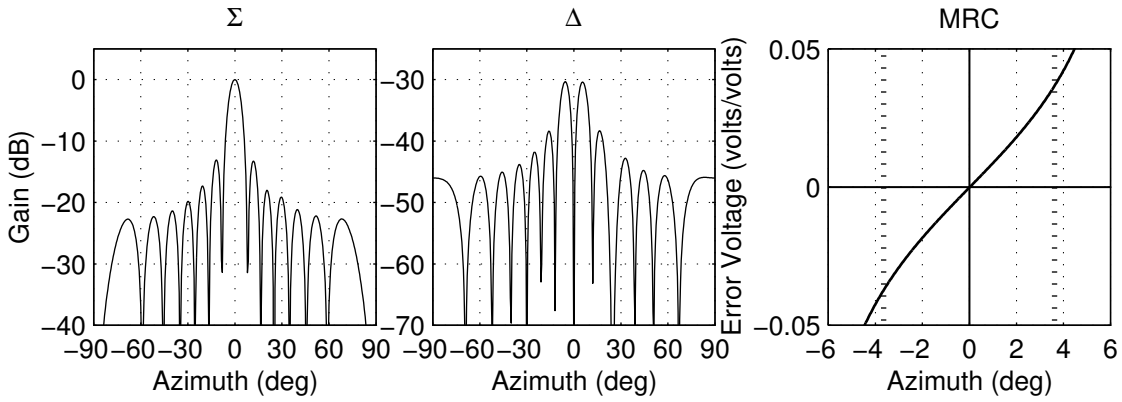

Figure 3.6: Monopulse sum and difference beams and MRC for sidelobe jamming with a jammer at 25°.

where $\mathbf{a}_\Sigma$ and $\mathbf{a}_\Delta$ are those of (3.3). A more general technique for arriving at adaptive sum and difference beams is by applying sum and difference unity gain constraints at the look direction,

$$\mathbf{w}^H\mathbf{a}_\Sigma = 1 \qquad \mathbf{w}^H\mathbf{a}_\Delta = 1, \tag{3.22}$$

which, from (2.24), yields minimum variance (MV) sum and difference weights

$$\mathbf{w}_\Sigma = \frac{\mathbf{R}_\mathbf{x}^{-1}\mathbf{a}_\Sigma}{\mathbf{a}_\Sigma^H\mathbf{R}_\mathbf{x}^{-1}\mathbf{a}_\Sigma} \qquad \mathbf{w}_\Delta = \frac{\mathbf{R}_\mathbf{x}^{-1}\mathbf{a}_\Delta}{\mathbf{a}_\Delta^H\mathbf{R}_\mathbf{x}^{-1}\mathbf{a}_\Delta}. \tag{3.23}$$

Note that a difference processor can be obtained from the adaptive sum processor in (3.23) by differentiating the numerator and normalizing the resulting weight vector. If the sum and difference processors possess distorted mainbeams then a corresponding distorted MRC must be employed. A natural choice is to employ the definition for MRC provided earlier in (3.12) (i.e., the ratio of beampatterns). Thus, when no interference is present then the angle estimates are exact, despite distortions that may be present in the beampatterns.

Figure 3.6 shows spatially adaptive sum and difference beampatterns with a corresponding monopulse curve for a 60 dB sidelobe jammer at 25°. A null at 25° can be discerned in the sum and difference beampatterns, but, overall, the beampatterns

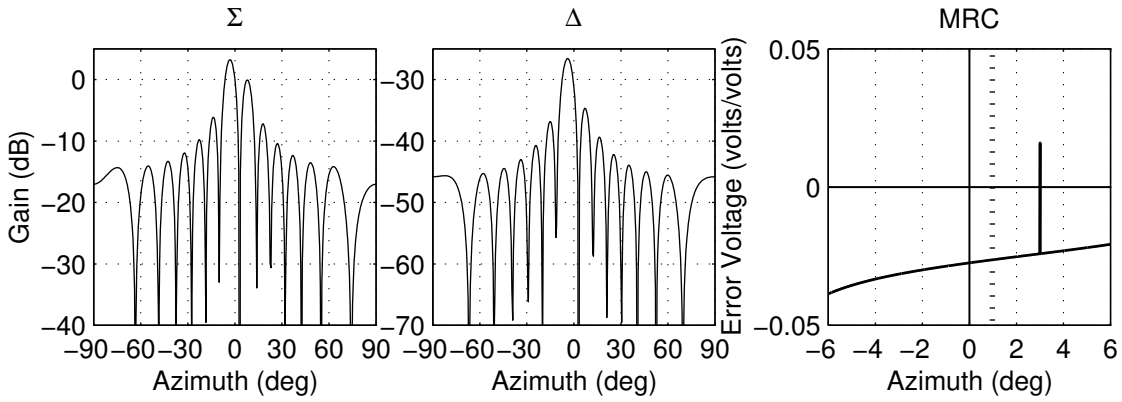

Figure 3.7: Monopulse sum and difference beams and MRC for mainbeam jamming with a jammer at 3°.

and MRC resemble those of the conventional processor (see Figures 3.4 and 3.5).[4] The 3 dB beamwidths of the conventional and adaptive processors (indicated by the dotted lines on the MRC) are the same, indicating that a sidelobe jammer has little or no effect on the MRC. However, as will be seen later, the angle-estimation performance of the adaptive processor, because of the placement of a null at the jammer location, improves significantly over that of the conventional processor, because the residual interference in the adaptive sum and difference outputs and, thus, in the error voltage is diminished.

Figure 3.7 shows spatially adaptive sum and difference patterns with a corresponding monopulse curve for a 60 dB mainbeam jammer at 3°. Distortions introduced by the jammer signal into the sum and difference beams are evident, in particular the common null at 3° that manifests itself as a singularity in the MRC. The distorted beams not only detract from the processor's angle estimation capability as evidenced by the flattened MRC, but also from the processor's robustness. The singularity that splits the sum beam in two is particularly problematic because it can introduce angle estimation ambiguities within a detection cell. For the moment con-

[4]Note that gain in Fig. 3.4 is plotted as signed amplitude whereas gain in Fig. 3.6 is plotted in decibel magnitude.

sider both sides of the split sum mainbeam as being contained within the detection cell.[5] An error voltage that is above -0.024 can be mapped to either 3° or a different angle that is greater than 3°, and hence an ambiguity. The problem becomes more severe when a real jammer is considered. In such a case the singularity may spread, thus causing the MRC to shoot up on one side and back down on the other side and, thus, to lose its monotone increasing or decreasing property across the singularity altogether. The resulting ambiguity is then present between two regions within the detection cell rather than between a region and a point as in the example – a more difficult ambiguity to contend with! Alternatively, if the half phased reversed difference beam (3.6) is used in (3.23) then this effect is observed for the simulated jammer used here, as well.

3.4 Angle Estimation Performance

In the previous section a detailed description of the monopulse technique was presented both in terms of concept and implementation. In this section, a formal methodology for assessing monopulse performance is established. Of particular interest is angle estimation performance. One particularly useful performance measure for angle estimation techniques is the rms (root mean square) of the angle error,

$$\sigma_{\epsilon_\phi} = \sqrt{\mathrm{E}\left\{|\epsilon_\phi|^2\right\}}. \tag{3.24}$$

For unbiased estimators (i.e., $\mathrm{E}\left\{\epsilon_\phi\right\} = 0$ [49]) the rms is also the *standard deviation of the angle error (STDAE)* [60]. In this thesis the term STDAE is adopted and used rather loosely to denote the rms definition (3.24) even when a biased estimator is involved.

[5] Technically, in establishing a detection cell's boundaries the half power points are considered, and for this example that would include only the left lobe. However, for illustrative purposes the right lobe is considered within the detection cell as well.

3.4.1 Standard Expression for Angle Accuracy in Monopulse

In [60, 2], expressions relating angle estimation performance of a monopulse processor to SNR and the monopulse slope are discussed. A reasonable approximation to the STDAE is

$$\sigma_\phi = \frac{1}{k_m \sqrt{2S_\Sigma / N_\Delta}} \sqrt{1 + \mathcal{M}^2(\phi_t)}, \tag{3.25}$$

where S_Σ is the signal power in the sum channel output, N_Δ is the noise-plus-interference power in the difference channel output, and $k_m = \mathcal{M}'(\phi_0)$ is the slope of the MRC at boresight.[6] A multiplicative correction term for off-boresight targets is included to the right of the fraction. This formula justifies the assertion made earlier that both cancellation performance and a well sloped MRC are necessary to attain good angle estimation performance.

Although (3.25) applies to mechanically steered antennas, it can be readily adapted to phased arrays by substituting a spatial frequency variable ν in place of the angle variable ϕ. Furthermore, substituting for the signal output power $S_\Sigma = \|\mathbf{w}_\Sigma\|^2 \sigma_t^2$ and the residual interference-plus-noise power in the difference channel output $N_\Delta = \left(\mathbf{w}_\Delta^H \mathbf{R}_\mathbf{x} \mathbf{w}_\Delta\right) \sigma_n^2$ yields the following expression for the rms of ν,

$$\sigma_\nu = \frac{\sqrt{\mathbf{w}_\Delta^H \mathbf{R}_\mathbf{x} \mathbf{w}_\Delta} / \|\mathbf{w}_\Sigma\|}{k_m \sqrt{2\sigma_t^2 / \sigma_n^2}} \sqrt{1 + \mathcal{M}^2(\nu_t)}, \tag{3.26}$$

where $k_m = \mathcal{M}'(\nu_0)$ is the slope of the MRC at boresight with respect to spatial frequency and σ_t^2 / σ_n^2 is the input SNR.

In order to assess the accuracy of the monopulse formula in predicting angle estimation performance, a few examples are brought forth. In these examples, the standard deviation (STD) of the spatial frequency error (i.e., $\sqrt{\mathrm{E}\left\{(\hat{\nu} - \nu)^2\right\}}$) rather than STDAE is considered and computed as a function of input SNR for various processors and interference conditions. In all cases the target is assumed to be on

[6] Note that angular quantities here differ in units from those in [60] in that they are expressed in degrees rather than beamwidths.

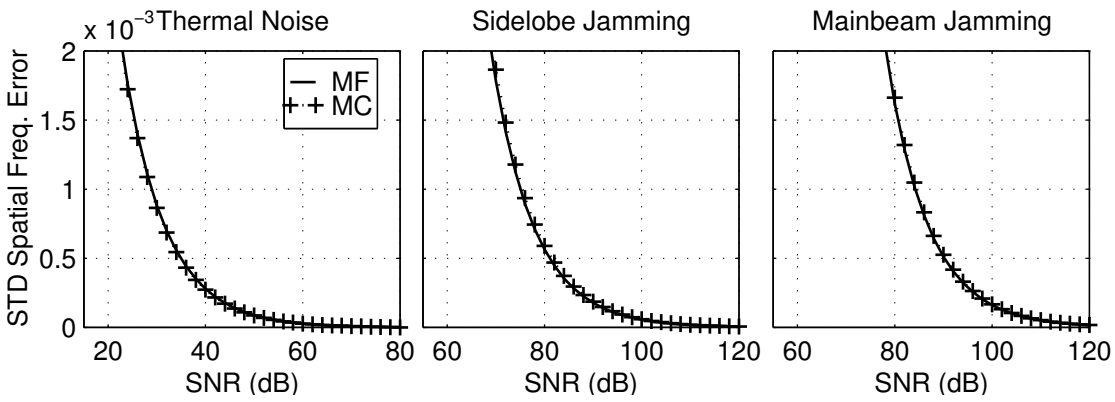

Figure 3.8: Monopulse formula (MF) using Eq. (3.26) versus Monte Carlo simulation (MC) for a conventional processor.

boresight. Two methods are considered here for computing rms performance: the monopulse formula (MF) in (3.26) and Monte Carlo (MC) simulation [49]. The experimental procedure employed for the latter method is briefly described in Sec. 4.4.5.

Results for a conventional monopulse processor are shown in Fig. 3.8. The left hand plot shows results for white noise, whereas the center and right hand plots show results for the sidelobe and mainbeam jamming examples of the previous section. In all three cases the analytic MF matches the simulation performance figures very well. As the interference conditions get progressively more difficult – in going from white noise to sidelobe jamming to mainbeam jamming – the curves shift further to the right.

In a second set of simulations, the adaptive processors of the previous section are considered. Figure 3.9 shows the two cases of sidelobe jamming and mainbeam jamming. Once again, for sidelobe jamming the MF accurately depicts angle estimation performance. However, for mainbeam jamming the MF proves more pessimistic than the experimental results indicate. In both cases the adaptive processors demonstrate significant improvement in angle estimation performance over that of the conventional processor. For the case of sidelobe jamming, the adaptive processor is able to whiten

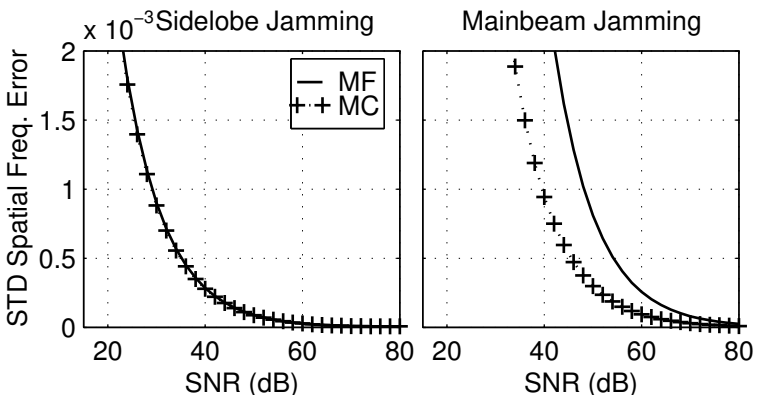

Figure 3.9: Monopulse formula versus Monte Carlo simulation for adaptive processors.

the jammer without distorting the mainbeam region and, thus, attain the noise floor performance demonstrated earlier in Fig. 3.8 when only thermal noise was present at the input.

For the remainder of the thesis angle estimation is computed based on MC simulation rather than the monopulse formula, because the MF fails to accurately predict angle estimation performance for an adaptive processor in a mainbeam jamming environment. Furthermore, the MF for arrays provides a measure of direction finding performance in sine-space units (i.e., spatial frequency). The STD in sine-space units is not readily convertible to the STD in the desired angular units, because of the nonlinear mapping (2.4) entailed. With MC simulation, on the other hand, the STD is computed from a sampling of angle estimates which are either initially expressed in degrees or can be converted to degrees via (2.4) prior to computing the STD.

3.4.2 Maximum Likelihood vs. Minimum Variance

In Sec. 3.3 two angle estimation techniques were discussed. The maximum likelihood (ML) technique offered optimal angle estimation performance because the angle estimator was being optimized directly. The minimum variance technique, on the other

hand, did not explicitly optimize an angle estimator, but rather minimized the interference in the individual sum and difference outputs and used a nonlinear mapping function to estimate the best "quiescent" angle estimate given the distorted sum and difference beams. However, since the distorted sum and difference beams take the same form for MV as for ML, it is suspected that MV offers at least a good approximation to ML.

In this section a comparison of the two techniques based on simulated results is carried forth. The sidelobe and mainbeam jamming parameters remain as before. The MV technique was implemented as discussed in Sec. 3.3.2 with sum and difference weights given by (3.23). The ML estimator was found by performing an exhaustive search for the solution of (3.15) in a specified angular region. In order to make the comparisons fair, the angular region over which the search took place corresponded to the angular region used in the analysis of the MV monopulse processor (i.e., the invertible MRC region within the beamwidth of the MV processor). Unlike the analysis performed in the previous section pertaining to the monopulse formula, an angle variable rather than a spatial frequency variable was used; a convention that is adopted throughout the remainder of the thesis. For both techniques a Monte Carlo simulation method for an on boresight target was used to arrive at STDAE performance.

Figure 3.10 illustrates STDAE performance for the ML, MV, and conventional processors. The curves for ML (solid) and MV (plus-dotted) are evaluated for an SNR range of 0 to 80 dB. However, note that for MV only the portion of the curve which corresponds to the detectable SNR range is shown. From Fig. 3.10 the detection cutoffs appear to be at 20 and 25 dB for sidelobe and mainbeam jamming, respectively. The curves for MV and ML approximately overlap for both sidelobe and mainbeam jamming, suggesting that indeed the MV technique may be a good approximation to the ML technique, if the SNR is high enough. Clearly both ML and MV improve significantly over the conventional monopulse processor (dashed). When plotted on

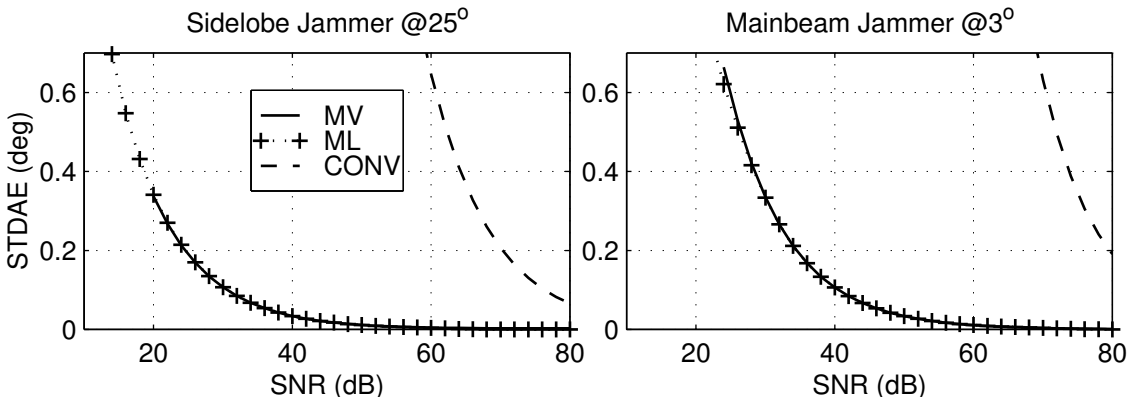

Figure 3.10: Maximum likelihood versus minimum variance and conventional monopulse techniques for sidelobe and mainbeam jamming.

a log scale, as in Fig. 3.11, an improvement factor of approximately 45 dB can be observed for both sidelobe and mainbeam jamming.

3.5 Summary

Angle estimation theory covers a wide variety of concepts and techniques. Of particular interest in radar is the monopulse angle estimation concept described in this chapter, which can also be found in the general literature [60, 2, 53, 26, 38]. The chapter presented background material pertaining to the origin of the monopulse technique, developed some of the theory pertaining to conventional array monopulse, and finished with a discussion of spatial adaptive monopulse, presenting examples that illustrate its strengths and weaknesses. The chapter concluded with a discussion of angle estimation performance both from a theoretical and experimental point of view. A comparison of angle estimation performance between a baseline adaptive monopulse processor and a maximum likelihood technique established spatial adaptive monopulse as a strong contender.

In the outcome of the various analyses, mainbeam jamming proved particularly problematic for spatial adaptive monopulse, where distorted beampatterns detracted

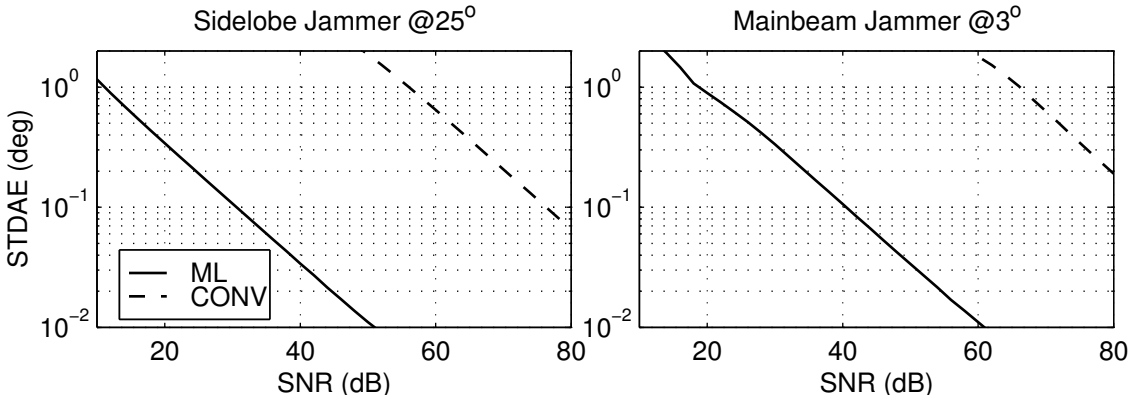

Figure 3.11: STDAE versus SNR on a log scale.

from angle estimation performance as well as from robustness. The failings of spatial adaptive monopulse motivate the development of space-time adaptive monopulse in the next chapter.

CHAPTER 4

Space-Time Monopulse

As explained and demonstrated in Chapter 3, spatial adaptive monopulse processing does not work well in a mainbeam jamming environment. However, we see from [31, 32, 33, 37] and Chapter 2 that space/fast-time (SFT) processing is able to provide substantial improvement of mainbeam jamming interference cancellation when TSI is present in the returns. In this chapter we develop a monopulse processor that employs SFT filtering to enhance angle estimation in much the same way that SFT filtering was employed in Chapter 2 to enhance interference mitigation. The resulting SFT monopulse processor ultimately proves advantageous over its spatial adaptive predecessors whenever TSI is present in the returns.

The chapter begins by generalizing the monopulse concept to SFT. Two optimization schemes, which have been successfully applied to spatial monopulse, are considered for the resulting SFT architecture. Once an architecture and an optimization criterion are selected, various design considerations and their tradeoffs are explored. Specifically considered are those intended to overcome the limitations of spatial distortion discussed earlier with respect to spatial monopulse, and target spreading discussed in Chapter 2 with respect to SFT filters. The chapter concludes with an evaluation of the new SFT monopulse concept on experimental data collected as part of the DARPA/Navy Mountaintop program [63, 62]. These examples include a qualitative evaluation of the beampattern response and MRC, and a quantitative evaluation of angle estimation performance. Various design issues for SFT monopulse

and their tradeoffs are considered as well.

4.1 Extending Monopulse to Space–Fast-Time

Recall, that a monopulse system generates an error voltage signal, $\epsilon_v(t)$, and maps the error voltage to a corresponding angle measurement using a mapping function called a monopulse response curve (MRC) denoted by $\mathcal{M}$. For estimating angles in a single plane (i.e., azimuth or elevation), such as will be done here, a single error voltage signal and MRC are required [60]. Care must be taken to ensure that the MRC, $\mathcal{M}$, is invertible, otherwise the angle estimate for a given value of error voltage, ϵ_v, may be ambiguous. Extension of spatial monopulse processing to SFT entails reinterpreting some of the spatial quantities defined in Sec. 3.2.

By definition, an SFT monopulse system has sum and difference filters that perform spatial as well as temporal filtering. The purpose of the temporal filtering is to rid the output signal of TSI and possibly mainbeam jamming interference. Sum and difference SFT processors are denoted by the $NT \times 1$ weight vectors $\mathbf{W}_\Sigma$ and $\mathbf{W}_\Delta$, respectively. Sum and difference outputs are given in terms of the respective processors,

$$z_\Sigma(t) = \mathbf{W}_\Sigma^H \mathbf{X}(t) \qquad z_\Delta(t) = \mathbf{W}_\Delta^H \mathbf{X}(t), \tag{4.1}$$

where $\mathbf{X}(t)$ is the $NT \times 1$ SFT snapshot at time instant t. The error voltage signal is, thus, a function of the ratio of SFT filtered outputs,

$$\epsilon_v(t) = \Re\left\{\frac{z_\Delta(t)}{z_\Sigma(t)}\right\}. \tag{4.2}$$

As before, the error voltage conveys purely directional information that must be converted to angular form via a mapping function. The mapping function or MRC was defined earlier as the ratio of difference to sum beampatterns and represented the "ideal" error voltage response to targets arriving from a particular angular region about boresight. SFT sum and difference processors have beampattern responses that

are functions of angle and time. In general, the SFT response of a processor is defined as

$$\mathcal{W}(\phi,\tau) = \mathbf{W}^H \left[\delta_T(\tau) \otimes \mathbf{a}(\phi)\right] = \mathbf{W}(\tau)^H \mathbf{a}(\phi), \tag{4.3}$$

where $\delta_T(\tau) = \left[\begin{array}{ccc} \mathbf{0}_{1\times\tau} & 1 & \mathbf{0}_{1\times T-\tau-1} \end{array}\right]^T$ is a $T \times 1$ vector of zeros with 1 as its τ^{th} component and $\mathbf{W}(\tau)$ denotes an $N \times 1$ vector comprised of the N weights in $\mathbf{W}$ corresponding to tap τ. Since the MRC must map error voltage to angle, it cannot retain its old definition as the ratio of $\mathcal{W}_\Delta$ and $\mathcal{W}_\Sigma$ because the responses now contain time dependencies.

Typically, in designing an SFT processor the target response is constrained to have a specific gain at a given angle and tap (i.e., time delay). For instance, the processor given by (2.28) has a unity gain look direction constraint at the first tap. It is anticipated, though not guaranteed, that the response has a peak at tap T_0 where the gain constraint is applied, particularly if range constraints are present. If the response is indeed strongest at T_0, then it is reasonable to define the MRC as the ratio of spatial responses there

$$\mathcal{M}(\phi) = \Re\left\{\frac{\mathcal{W}_\Delta(\phi,T_0)}{\mathcal{W}_\Sigma(\phi,T_0)}\right\}, \tag{4.4}$$

where $\mathcal{W}(\phi,T_0)$ is the response of an SFT processor at tap T_0.

An alternative way to arrive at the expression for the MRC is to consider the definition of error-voltage in (4.2):

$$\epsilon_v(t) = \Re\left\{\frac{z_\Delta(t)}{z_\Sigma(t)}\right\} = \Re\left\{\frac{\mathbf{W}_\Delta^H \mathbf{X}(t)}{\mathbf{W}_\Sigma^H \mathbf{X}(t)}\right\}. \tag{4.5}$$

If the SFT snapshot, $X(t)$, contains a target, then the response of the sum processor is anticipated to be strongest when the target appears at tap T_0. A target, $\mathbf{V}_{tgt}$, at T_0 is given by

$$\mathbf{V}_{tgt} = \delta_T(T_0) \otimes \mathbf{a}(\phi). \tag{4.6}$$

Evaluated for this target, the error voltage is

$$\epsilon_v(\mathbf{V}_{tgt}) = \Re\left\{\frac{\mathbf{W}_\Delta^H \mathbf{V}_{tgt}}{\mathbf{W}_\Sigma^H \mathbf{V}_{tgt}}\right\} = \Re\left\{\frac{\mathbf{W}_\Delta^H \left[\delta_T(T_0) \otimes \mathbf{a}(\phi)\right]}{\mathbf{W}_\Sigma^H \left[\delta_T(T_0) \otimes \mathbf{a}(\phi)\right]}\right\} = \Re\left\{\frac{\mathcal{W}_\Delta(\phi, T_0)}{\mathcal{W}_\Sigma(\phi, T_0)}\right\}, \quad (4.7)$$

which is the same expression as for the MRC given in (4.4).

4.2 Selecting a Minimization Criteria

Now that the monopulse concept has been generalized to SFT, an optimization criteria needs to be considered. In one approach, a maximum likelihood angle estimator based on SFT sum and difference beams would be developed in a similar manner to the spatial case in [11]. However, the estimator in [11] was noted in [10] to have certain disadvantages that would be of concern in an SFT implementation. In particular, there is a lack of control over the SFT responses of the sum and difference processors. Extending the analysis in [11] to SFT would not permit the required degree of control over the temporal behavior of the new SFT sum and difference processors. The consequence is potential target spreading and, hence, reduced range-cell resolution. As a result, targets that are close to each other in range overlap at the output, rendering angle estimation difficult or impossible. The results are similar to those of spatial monopulse when multiple targets overlap in the mainbeam [26].[1] A spatial only MRC utilized together with SFT filters cannot tolerate overlapping targets nor can it tolerate target spreading. Furthermore, as mentioned in Chapter 2, radars typically transmit a coded waveform (e.g., LFM) that is match filtered at the output. An SFT filter that permits target spreading warps the LFM signal and, hence, drastically reduces the gain of the matched filter.

A second and more robust option is to employ linearly constrained optimization [29]. In contrast to a maximum likelihood (ML) approach, the use of linear constraints would allow the designer to exercise a great deal of control over both the spatial and

[1] In [68] a set of three Butler beams is used to resolve the angles of arrival of two sources in the mainbeam.

temporal behaviors of the SFT sum and difference processors, thus assuring robustness by providing a means to avoid target spreading and other distorting effects. The disadvantage of the linearly constrained approach is that it cannot be used directly to minimize an angle estimation performance criteria as is the case with the maximum likelihood approach. At best it is able to minimize the residual interference in the respective sum and difference outputs. Nonetheless, as was demonstrated in Chapter 3, a spatial monopulse processor was able to achieve near ML performance.

To summarize, ideally we would like to be able to

- directly minimize angle estimation error, and
- exercise control over the spatio/temporal response of the processor so that the effect of target spreading and overlapping targets is reduced.

To achieve both requires a highly nonlinear solution that is not of practical consideration. Maximum likelihood estimation has been shown to offer direct minimization capability for the spatial case. However, the solutions were nonlinear and required simplifying approximations for implementation, which would only present more difficulties when working in the SFT domain. The linearly constrained optimization approach, on the other hand, provides a simple linear solution that allows for a controlled response. However, because angle estimation is not the criteria being optimized, a small but acceptable price may be paid in terms of angle estimation performance.

4.3 Designing Sum and Difference Filters

Having reinterpreted the MRC for SFT and selected an optimization criteria, the next step is to design the sum and difference processors, $\mathbf{W}_\Sigma$ and $\mathbf{W}_\Delta$. The desired monopulse processor should have the target response characteristics shown in Fig. 4.1 and yet provide adequate suppression of main-beam jamming with minimal target spreading. The SFT processor considered is that of (2.24) with a set of constraints chosen to achieve these criteria.

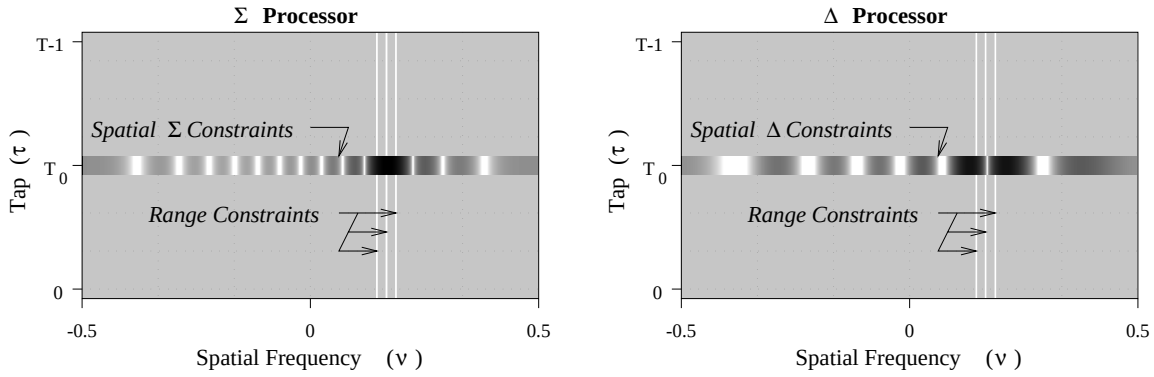

Figure 4.1: Constraint specifications for the SFT adaptive monopulse processor.

Of the T taps in the processor, the T_0^{th} tap captures the target as shown in Fig. 4.1. To prevent target spreading in the look direction, range constraints are applied at the look direction (ν_0) for all taps except T_0 (shown as the center white line in Fig. 4.1). In general, however, it is not sufficient to apply one set of range constraints at the look direction. Since the detected target may have been detected anywhere within the mainbeam, it is necessary to provide additional range constraints about the look direction at spatial frequencies, $\nu_0 \pm 0.5/N$ (shown as additional white lines in Fig. 4.1). They do not ensure zero gain throughout the angular extent of the mainbeam but rather serve as "anchors" to keep the gain low in that region, and, as such, they serve to sharpen the beam along the range direction. The specified range constraints are implemented via a constraint matrix and vector:

$$\mathbf{C}_0 = \begin{bmatrix} \mathbf{I}_{T_0} & \mathbf{0}_{T_0 \times T - T_0} \\ \mathbf{0}_{T-T_0-1 \times T_0+1} & \mathbf{I}_{T-T_0-1} \end{bmatrix} \otimes \begin{bmatrix} \mathbf{a}(\nu_0 - \frac{1}{2N})^H \\ \mathbf{a}(\nu_0)^H \\ \mathbf{a}(\nu_0 + \frac{1}{2N})^H \end{bmatrix} \tag{4.8}$$

$$\mathbf{c}_0 = \mathbf{0}_{3(T-1)\times 1}. \tag{4.9}$$

Spatial response constraints (SRC) are defined for an expected target at tap T_0. Typically, a unity gain constraint (2.28) is used, but, for the case of monopulse processing in mainbeam jamming, a more rigid set of constraints is necessary to ensure a reliable and robust MRC. This requirement is met most stringently by forcing the

processor to take the form of a conventional processor at tap T_0, in which case the spatial responses of the processors are identical to one of those shown in Fig. 3.4. This condition can be met by applying the constraint matrix and vector:

$$\mathbf{C}_1 = \left[\begin{array}{ccc} \mathbf{0}_{1\times T_0} & 1 & \mathbf{0}_{1\times T-T_0-1} \end{array} \right] \otimes \mathbf{I_N}, \tag{4.10}$$

$$\mathbf{c}_1 = \begin{cases} \mathbf{a}_\Sigma, & \text{if sum processor,} \\ \mathbf{a}_\Delta, & \text{if difference processor.} \end{cases} \tag{4.11}$$

The sum and difference steering vectors $\mathbf{a}_\Sigma$ and $\mathbf{a}_\Delta$ can be one of those given in equations (3.3), (3.6), (3.8), or some other valid sum and difference pair. An alternative and simpler method for implementing the SRC is to apply a large degree of diagonal loading to the portion of the covariance matrix $\mathbf{R_X}$ corresponding to T_0,

$$\mathbf{R_X} \rightarrow \mathbf{R_X} + \sigma_d^2 \left[\delta_T(T_0) \cdot \delta_T(T_0)^T \right] \otimes \mathbf{I}_N, \tag{4.12}$$

along with a unity gain constraint at T_0,

$$\mathbf{C}_1^{alt} = \begin{cases} \left[\delta_T(T_0) \otimes \mathbf{a}_\Sigma \right]^H & \text{if sum processor,} \\ \left[\delta_T(T_0) \otimes \mathbf{a}_\Delta \right]^H & \text{if difference processor,} \end{cases} \tag{4.13}$$

$$\mathbf{c}_1^{alt} = 1. \tag{4.14}$$

Both approaches for implementing the SRC result in identical processors.

The range constraints are grouped with the spatial response constraints giving the constraint matrix and vector

$$\mathbf{C} = \left[\begin{array}{c} \mathbf{C}_0 \\ \mathbf{C}_1 \end{array} \right], \qquad \mathbf{c} = \left[\begin{array}{c} \mathbf{c}_0 \\ \mathbf{c}_1 \end{array} \right]. \tag{4.15}$$

The sum and difference processors are specified in terms of the design parameter T_0. The significance of T_0 is in the type of prediction that the resulting processor performs. In the example of Sec. 2.4.1 and in the derivations of [34, 31], a forward prediction filter is implemented by specifying that the target appear in the first tap

(i.e., $T_0 = 0$). On the other hand, if the target is constrained to appear in the final tap (i.e., $T_0 = T - 1$), a backward prediction filter results. In Sec. 4.4 a tap-centered configuration (i.e., $T_0 = T/2$) corresponding to a combination of forward and backward prediction is selected because the components of the jamming signals in the sidelobes arrive both before and after the corresponding mainbeam components.

In summary, extending monopulse processing into SFT entails the following key steps:

- Redefining the MRC in terms of the SFT responses of the sum and difference channels.
- Adopting an optimization criteria and solving for the sum and difference channel processors.
- Defining desired response characteristics for the sum and difference channels.

After achieving these goals, angle estimation proceeds in the same way as described in Sec. 3.2 (i.e., using Eq. 3.13).

4.4 Angle Estimation Results with Experimental Data

In this section performance of SFT monopulse is demonstrated for a variety of experimental Mountaintop (MT) datasets collected as part of the DARPA Mountaintop program [63, 62]. The radar employed [8] is a bistatic array of 14 elements spaced 1/3 meters apart. In gathering data the array transmitted bursts of 16 pulses spaced 3.2 milliseconds apart (i.e., $T_r = 0.0032$) on a 435 MHz carrier and sampled the incoming baseband signals at 1 MHz. Two-hundred kHz Gaussian bandpass filters centered at the carrier frequency at the front end of each element's receiver filter the incoming data returns prior to sampling. The radar is situated on top of a mountain to simulate

airborne as well as ground based environments. All subsequent results are normalized to the radar's noise floor of 50 dB.

Initially, four existing methods for generating sum and difference beams with their corresponding spatial adaptive implementations are considered:

1. (DER) Adaptive distorted sum and derivative difference beams.

2. (CAS) Adaptive distorted sum and derivative difference beams with zero-bias constraint (see Castella [10]).

3. (GAB) Cosine/sine illumination sum and difference beams (see Gabriel [20], Lin and Kretschmer fengling,lingrep1).

4. (HPR) Adaptive distorted sum and half-phased-reversed difference beams.

The first method, DER, is based on the unity gain constraint processor pair (3.23) with sum and difference steering vectors given by (3.8). The second method, CAS, adds a constraint to the difference processor to force a null at boresight, thus, ensuring an unbiased monopulse curve. The third method, GAB, employs sinusoidal tapering to generate sum and difference steering vectors in (3.23). The fourth method, HPR, is based on the unity gain constraint processor pair (3.23) with sum and difference steering vectors given by (3.6).

Ultimately, only one of the above methods is considered for evaluation and analysis of SFT monopulse. However, prior to selecting a method, an analysis and comparison of the four must take place. In all of the analyses, an evaluation of mitigation performance, beampattern response, resulting MRC, and angle estimation performance is included. The first to be eliminated is CAS, on the basis that it yields identical angle estimation performance to DER, as demonstrated through simulations and an analytical proof in Appendix A. The SFT extensions of DER, GAB, and HPR are then introduced and compared to their spatial counterparts. Processor GAB is then eliminated on the basis of inferior angle estimation performance to DER and

HPR. Since DER and HPR perform similarly only the standard adaptive processor, DER, and its SFT extension are considered further.

Once DER has been selected as the method of choice for generating sum and difference beams, evaluation of various aspects of SFT monopulse proceeds. Full spatial constraints at T_0 are introduced into the SFT extension of DER and the resulting sacrifice in performance for improved robustness and beamwidth is investigated. Relaxation of the full spatial constraints is then performed via variable diagonal loading on T_0 to determine the amount of performance that could be regained without adversely affecting robustness. Similarly, a relaxation method employing reduced constraints is also evaluated.

Till now, all performance results were based on stationary TSI data coming from the `mmit004v1` Mountaintop dataset. Results based on the nonstationary TSI dataset `rio043v1` are presented and a comparison drawn between the spatial processor and its SFT extension. A summary of results based on other Mountaintop datasets containing various forms of jamming and TSI – stationary, nonstationary, and indirect path jamming – are tabulated for the spatial and SFT implementations. Finally, results are given that demonstrate the merit of the SFT monopulse processor under ordinary jamming conditions.

Remaining to be addressed are certain concerns that arise with SFT monopulse and spatial adaptive monopulse under conditions of mainbeam jamming. In order to alleviate some of these concerns, a beamwidth analysis and an explanation of transmit-receive beampatterns are included.

4.4.1 Spatial Processing Results

When no taps are utilized then the comparison between the four processors is straight forward. Adaptive weights for each of the four processors are computed for mountaintop dataset `mmit004v1`. The look direction corresponds to the jammer present at 32° east of boresight, thus making this a mainbeam jamming problem.

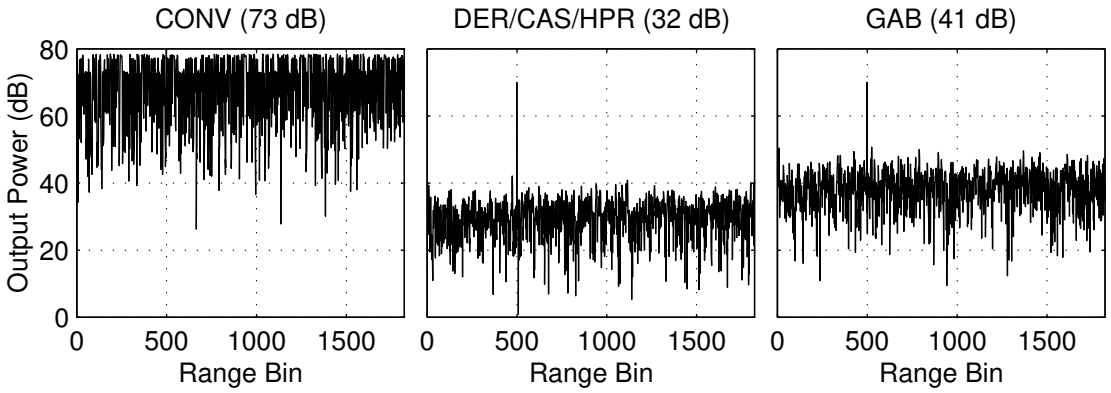

Figure 4.2: Sum (Σ) Outputs.

Filtered outputs from a conventional processor and the four adaptive processors are shown in figure 4.2. Note that the Σ component of the DER, CAS, and HPR processors are the same, and, therefore, only one output is shown for all three. This, however, is not the case for the Δ component of the processors and corresponding outputs, so indeed we are talking about different processors. The output interference to noise ratio (OINR) is indicated above each plot. A 70 dB synthetic target has been injected into the TSI input data in range bin 500. As can be seen from the filtered outputs, no target cancellation occurs. This is not by coincidence, but rather by design, and is intended to enable the OINR to be used as a direct measure of mitigation performance. By that token, the DER, CAS, and HPR processors demonstrate improved mitigation performance over the tapered processor (GAB).

The sum and difference beampatterns of the DER, CAS, and GAB processors are shown in Fig. 4.3.[2] A dashed line indicates the boresight angle (look direction) and coinciding jammer location. As the experimental results demonstrate, the spatial processors have highly distorted sum and difference beampatterns. The high sidelobes seen in the Σ beampatterns are typical of mainbeam jamming. Although such high sidelobes would be unacceptable in an actual radar processor implementation, it is

[2]HPR has been omitted from this comparison because of its similarity to DER.

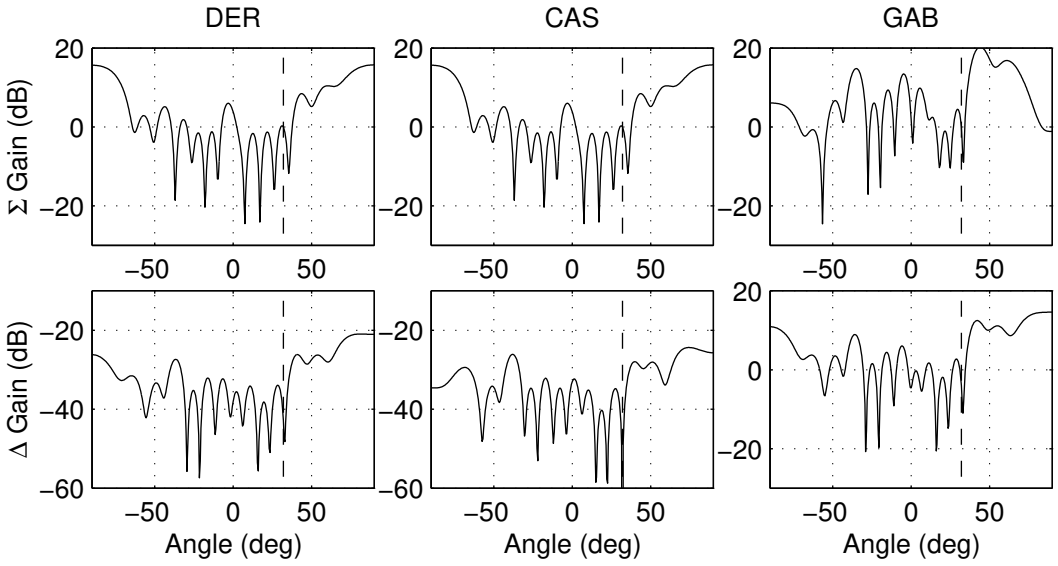

Figure 4.3: Sum and Difference Beampatterns.

shown later that the high sidelobes appear much lower when both the transmit and receive beampatterns are taken into consideration. Therefore, for the time being, the focus is on the mainbeam which is positioned about the look direction. In a conventional processor the mainbeam is symmetric about the look direction. However, for any of the adaptive processors the mainbeam appears skewed, bulging to the left of the look direction. This is particularly problematic in the Σ beampattern of GAB. The sinusoid tapering originally intended to widen the mainbeam in exchange for reduced sidelobes has apparently caused a degradation in both the sidelobes and the mainbeam of the resulting Σ beampattern.

The bottom row of Fig. 4.3 has the corresponding Δ beampatterns of the three processors. Once again, the discussion of high sidelobes is deferred to a later point, and the focus is on the split mainbeam. In the case of the DER processor, the split in the mainbeam occurs slightly offset from the look direction, which ultimately results in a biased monopulse response curve. The CAS processor, however, solves this problem by placing a null constraint at the look direction, thus resulting in a zero-bias MRC. Finally, the Δ beampattern in the GAB processor appears not much different then its corresponding Σ beampattern, with the null in the Δ pattern being very near the null of the Σ beampattern. As will be shown next, the MRC of the GAB processor suffers degradation as a result of the highly skewed beampatterns.

Monopulse response curves for the three processors are shown in Fig. 4.4. The MRCs for the DER and CAS processors are very similar. The solid line indicates the region where the MRC is usable (i.e., invertible). The dashed line indicates the look azimuth. In the tapered processor it is noted that the usable portion of the MRC curve intersects the look azimuth close to its right edge. This highly biased MRC is in effect only useful for estimating angles to the left of the look azimuth, and hence, for this particular mainbeam jamming scenario the GAB processor is not very useful.

Monopulse performance curves are shown in Fig. 4.5. Monopulse performance is measured in terms of the standard deviation of angle error (STDAE) as defined

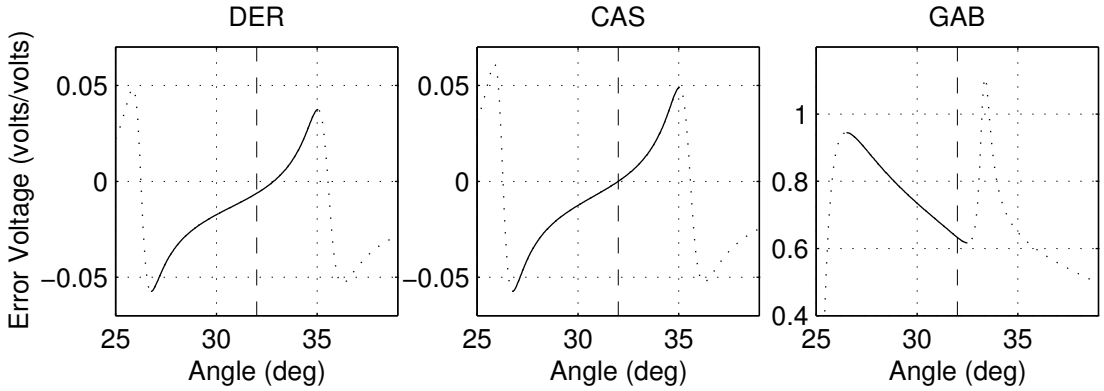

Figure 4.4: Monopulse Response Curves.

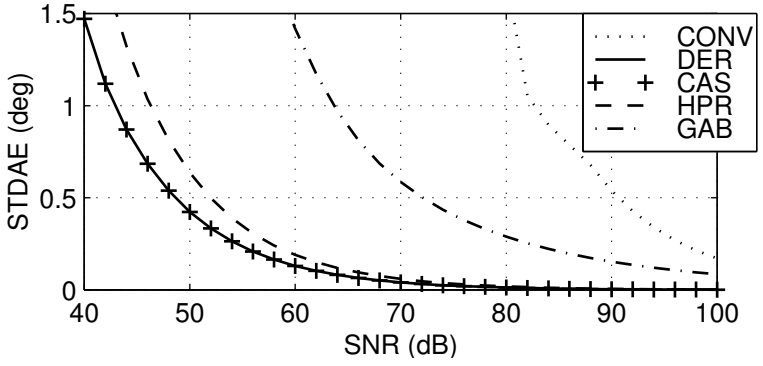

Figure 4.5: Monopulse Performance Curves.

earlier in (3.24). As the SNR is increased, STDAE performance is expected to improve as demonstrated by the asymptotically down sloping curves.

From Fig. 4.5 it can be seen that the DER and CAS processors perform identically. The beampatterns and MRCs of the difference processors in Fig. 4.3 and 4.4, however, clearly showed that the two processors are different. It turns out that not only is the statistical performance of both processors identical, but also the deterministic angle estimates are themselves identical. An analytical proof for the equivalence of the two processors in terms of angle estimation is provided in Appendix A. Since DER and CAS are in fact equivalent whether a spatial or SFT implementation is opted, the CAS processor is not considered further.

The GAB processor performs rather poorly in terms of angle estimation with respect to the other adaptive processors in the mainbeam jamming environment. In the next subsection, where the extension of the spatial adaptive processors to SFT is considered, GAB is shown to suffer even further degradation and is considered only briefly because of its poor performance in the mainbeam jamming environment.

4.4.2 Space–Fast-Time Processing Results

Comparison of Processors

Here the DER, HPR, and GAB spatial processors are extended to SFT using the method introduced in Sec. 4.1. The extension employs 20 taps, a unity gain constraint at $T_0 = 0$, and a single set of range constraints at the look direction. A similar set of results to those in Sec. 4.4.1, contrasting the different processors is included here in order to determine a suitable candidate among DER, GAB, and HPR for further performance analysis of the SFT monopulse technique. Filtered outputs from the three processor are provided in Fig. 4.6. Note that once again the Σ component of DER and HPR are identical, and, thus, only one plot is provided for both. The SFT DER and HPR processors demonstrate a 9 dB improvement in performance over their spatial counterparts, and the GAB processor demonstrates a 5 dB improvement over

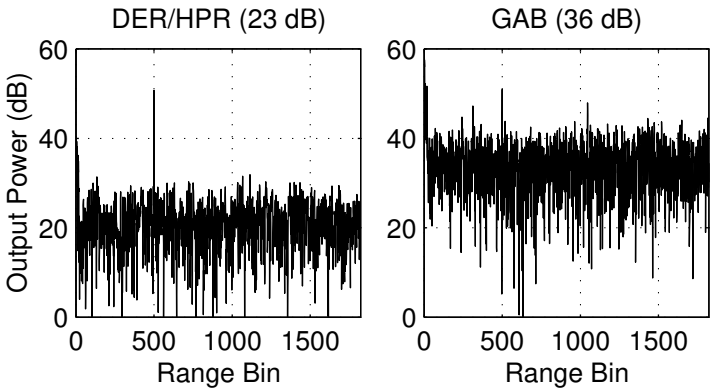

Figure 4.6: Sum (Σ) Outputs.

its spatial counterpart. This time a 50 dB synthetic target has been injected into the `mmit004v1` data, which shows up at the output of each of the three processors.

In contrast to the spatial processors, the SFT processors have two-dimensional beampatterns as shown in Fig. 4.7. The left and right-hand side plots correspond to the DER and GAB processors, respectively (HPR is omitted again because of its similarity to DER). The two-dimensional Σ and Δ beampatterns are shown for each processor. Spatial distortions at T_0 are present in the SFT beampatterns, as they were in the spatial case. In further analysis, it is shown that the overall spatial response and robustness of the SFT processor can be improved at the expense of OINR and angle estimation performance by applying spatial response constraints (SRCs).

Target spreading in range does not occur in the spatial case because a spatial processor is memoryless. In SFT, however, target spreading can be quite problematic. Even though range constraints have been applied at the look direction, both the DER and GAB difference processors suffer target leakage in the first few taps. Imposing a single set of range constraints is apparently not sufficient to ensure the required low gain throughout the split mainbeam of the difference processors at successive taps. In contrast to the Δ processors, the Σ processors are not as sensitive to target spreading, and a single set of range constraints is apparently sufficient for this particular tap configuration.

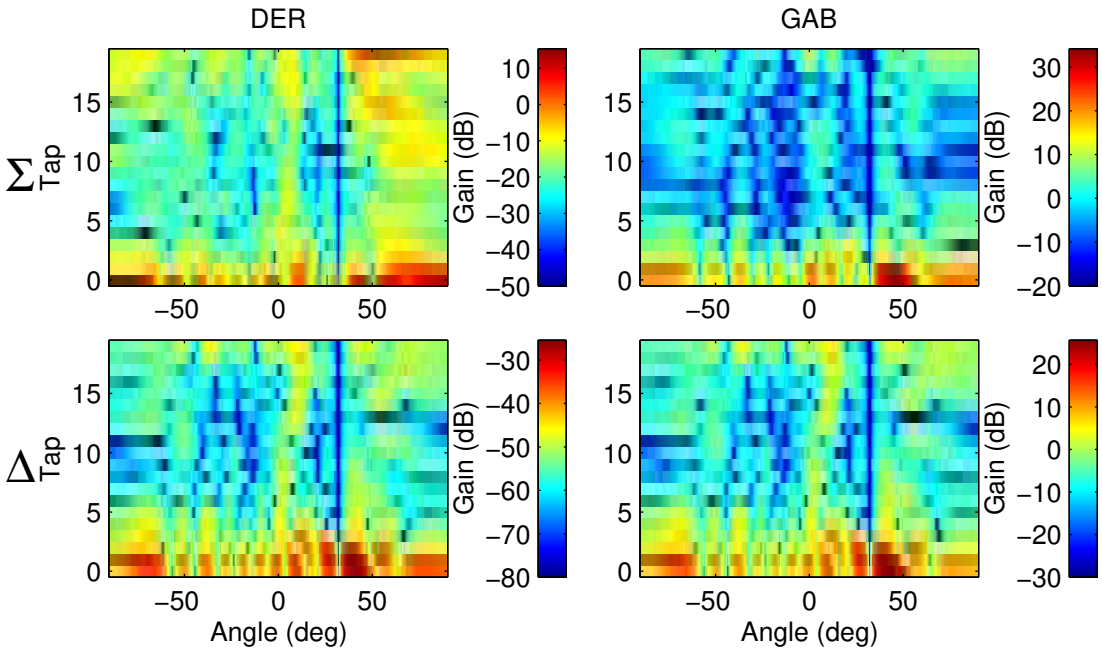

Figure 4.7: Sum and Difference Beampatterns.

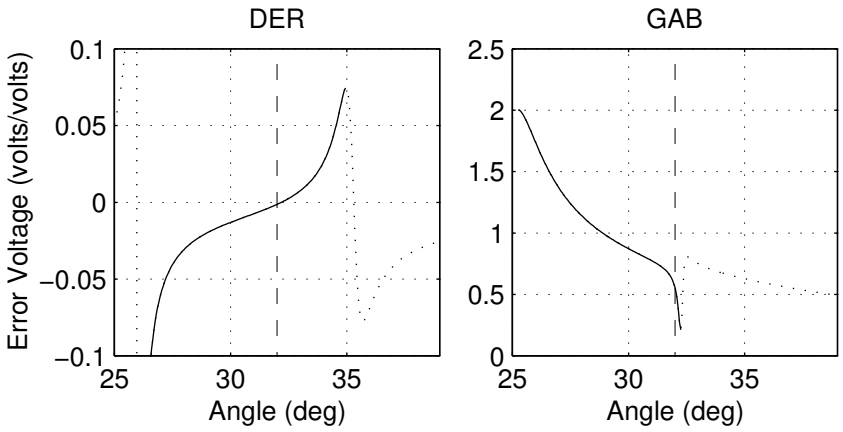

Figure 4.8: SFT Monopulse Response Curves.

As was noted earlier, the spatial GAB processor suffers mainbeam response degradation. The extension of the GAB processor to SFT makes this problem even more severe. In the sum processor a high gain artifact just to the right of the look direction overwhelms the mainbeam.

Monopulse response curves for the SFT DER and GAB processors are shown in Fig. 4.8. These monopulse curves appear very similar to those encountered in the spatial only case. The merit of SFT monopulse over spatial monopulse is demonstrated by comparing the angle estimation performance of the SFT processors, shown in Fig. 4.9, to that of the spatial processors shown in Fig. 4.5. Once again the DER and HPR processor demonstrate similar angle estimation performance whereas the GAB processor lags behind.

The DER and HPR processors have been demonstrated to be clearly superior to the GAB processor in terms of the various performance criteria adopted here. As a result, the GAB processor is not considered further. HPR is also not considered further because of its similarity to DER. A more in depth analysis of SFT monopulse using the DER method of generating difference beams follows.

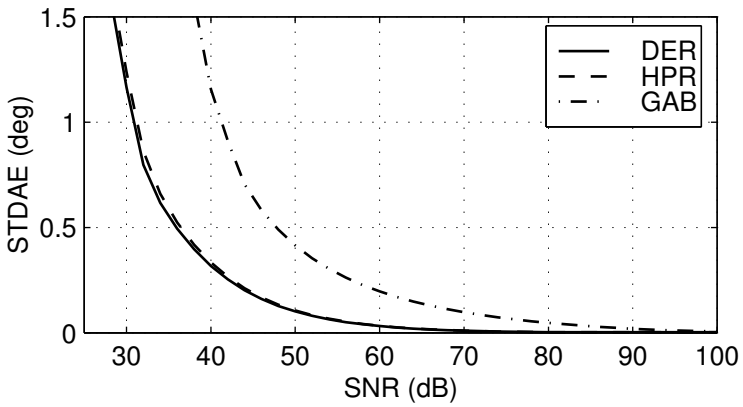

Figure 4.9: Monopulse performance curves for 20-Tap SFT processors.

Fully Constrained SFT Processor

In the preceding analysis an SFT processor with unity gain constraint at the first tap and a single set of range constraints at the look direction proved problematic in terms of target spreading. It also suffered from spatial distortion in conditions of mainbeam jamming as did the single tap processor. It was stated earlier that employing SFT processing with spatial response constraints and multiple sets of range constraints reduces that distortion. In this section a full spatial constraint tap-centered DER processor with three sets of range constraints about the look direction is investigated. The resulting sacrifice in performance is then justified in terms of improved robustness (e.g., fewer distortions and consistent behavior under varied conditions).

Filtered outputs for a 20 tap and a 50 tap processor are shown in Fig. 4.10. The resulting loss in OINR performance is apparent when comparing the 20 tap fully constrained processor to the 20 tap unity gain processor in Fig. 4.6. It takes an additional 30 taps (i.e., 50 taps) to regain the 23 dB OINR performance of the 20 tap unity gain processor. As will be shown, not only do the additional constraints take a toll on OINR performance but also on angle estimation performance. However, as shown in Fig. 4.11, the resulting spatial beampattern at T_0 is indeed that of a conventional processor and, hence, far improved over the distorted spatial beampatterns

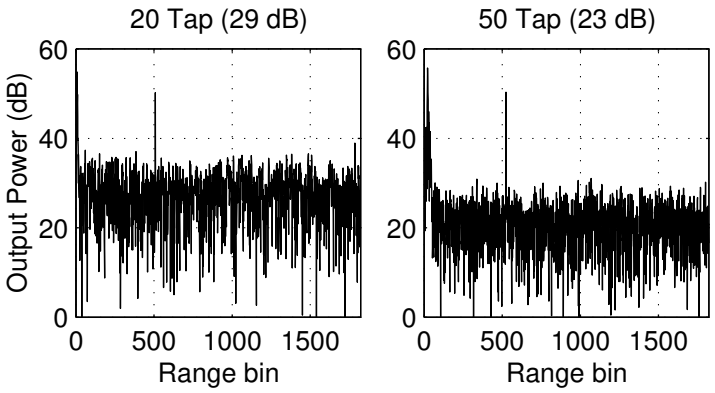

Figure 4.10: Outputs for 20 and 50 tap SFT Sum (Σ) Processors.

of the unity gain processors. Additionally, target spreading is eliminated throughout the extent of the mainbeam as demonstrated by the deep nulls cutting across range. Problems still exist with areas lying outside of the mainbeam region, but, as indicated earlier, the focus at this point is on the mainbeam, whereas issues regarding the outlying regions are treated later.

The angle estimation performance of the 20 and 50 tap SFT processors is shown in Fig. 4.12. Included for reference are the conventional processor and spatial adaptive processor. As mentioned earlier, the fully constrained SFT processor suffers mitigation performance degradation in exchange for increased robustness. This is true for angle estimation performance as well, where it is noted that the 20-tap fully constrained processor performs similarly to the unity gain spatial processor. All things being equal, the 20-tap processor should improve on the unity gain processor, as it does in Fig. 4.13. In the comparison of Fig. 4.13 the SFT processors have been constrained with a unity gain constraint at the first tap rather than a full set of SRCs at the center tap, and three sets of range constraints about the look direction for successive taps. The second comparison is thus a "fairer" comparison since the spatial beam patterns of the SFT processors are allowed to be distorted and, thus, possess narrower mainbeams much like those of the spatial adaptive processor. An explanation of why smaller beamwidths result in seemingly improved STDAE

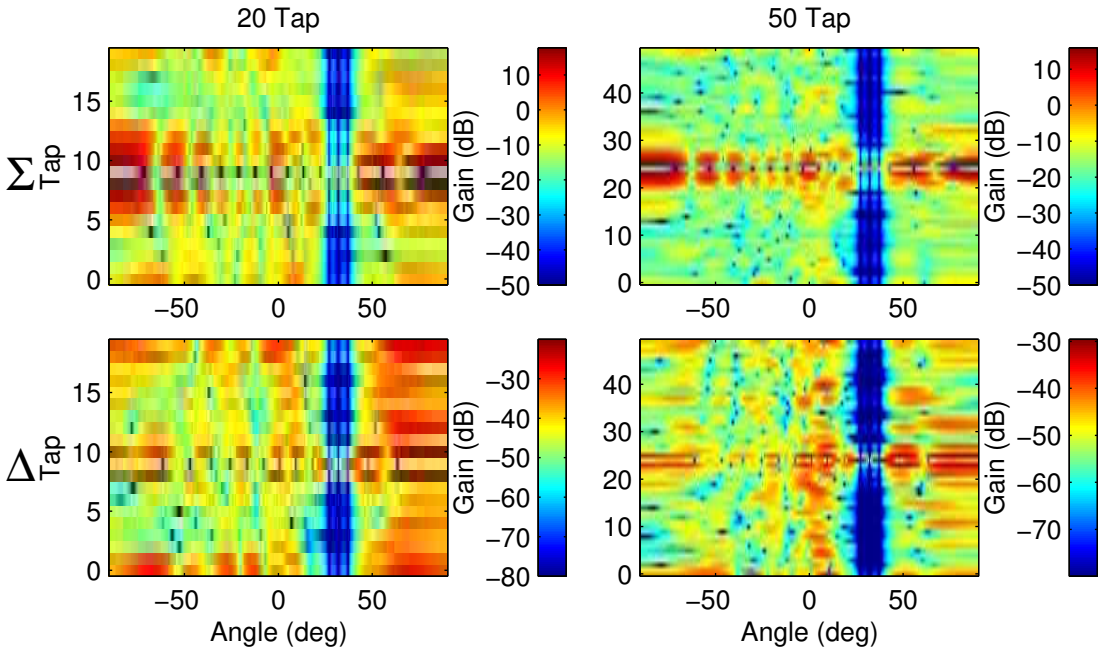

Figure 4.11: Sum and Difference Beampatterns for fully constrained SFT processors.

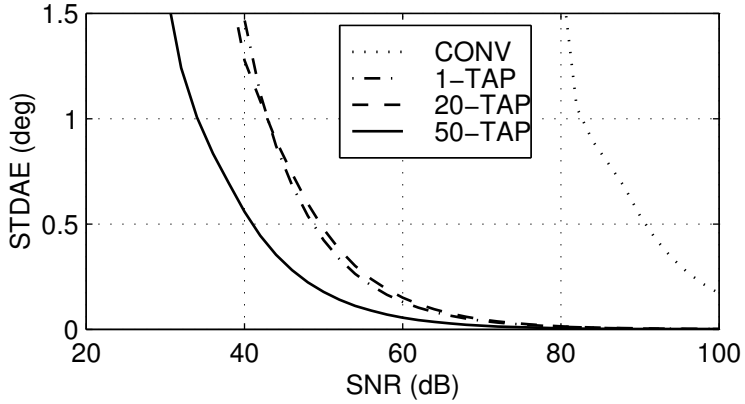

Figure 4.12: Monopulse performance curves for fully constrained SFT processors.

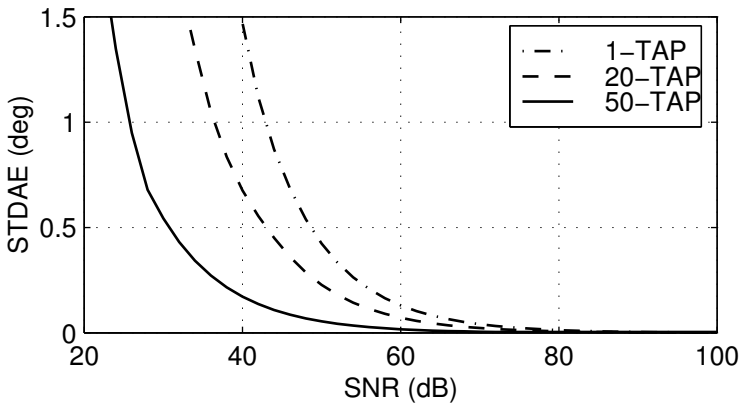

Figure 4.13: Monopulse performance curves for partially constrained SFT processors.

performance is offered in Sec. 4.4.5. The main point to keep in mind is that SFT filtering is able to enhance STDAE performance and/or robustness. If robustness (i.e., beamwidth integrity and consistent performance) is desired then a fully constrained SFT processor can offer it at the expense of STDAE performance.

In comparing angle-estimation performance, it is sometimes convenient to speak of *burnthrough* as discussed in Sec. 2.5.2. For instance, given a desired STDAE of 0.5°, the conventional processor requires 91 dB of SNR, whereas the 50-tap fully constrained SFT processor requires only 41 dB of SNR – an improvement of 50 dB! Burnthrough time is thus reduced by a factor of 100,000. That is, the conventional processor would have to transmit 100,000 pulses to achieve the same STDAE as the 50-tap processor does with 1 pulse. With respect to the spatial adaptive processor, the reduction in burnthrough time is approximately 5.

Tap Analysis

Figure 4.14 fixes the SNR at 50 dB and varies the number of taps from 1 to 50 for fully constrained and partially constrained SFT processors. The fully constrained SFT processor utilizes a full set of SRCs whereas the partially constrained SFT processor utilizes a single unity gain constraint. Both employ a tap-centered configuration with

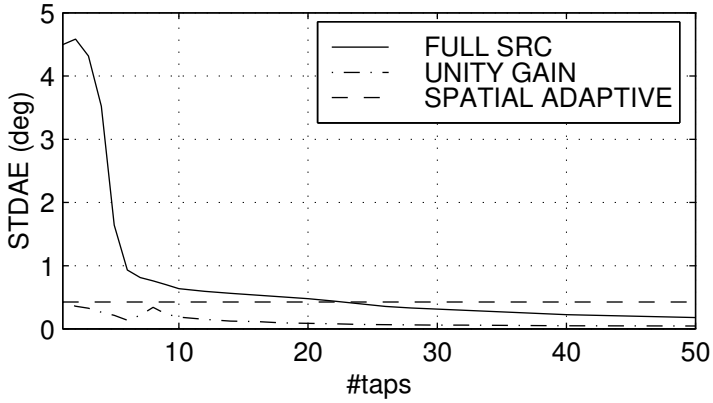

Figure 4.14: STDAE versus number of taps for fully and partially constrained SFT DER processors.

three sets of range constraints about the look direction. STDAE is plotted versus the number of taps in the processor. The solid and dash-dot line curves indicate performance for the fully constrained and partially constrained SFT processors, respectively. A horizontal dashed line indicates the performance of the 1-tap unity gain adaptive processor. The plot suggests that a 22 tap fully constrained SFT processor is necessary to achieve the same level of angle estimation performance as the 1 tap unity gain processor. As noted before, this is a necessary cost incurred for the increase in beamwidth and robustness afforded by the fully constrained SFT processor. On the other hand, any number of taps in the partially constrained SFT processor improves on the spatial adaptive processor.

The SFT curves demonstrate that, whether or not robustness is desired, employing additional taps ultimately results in improved angle estimation performance, whereas confinement to a single tap lacks potential for improvement. In practice, however, computational resources and availability of training data limit the potential for improvement with the SFT processors as well, by limiting the number of taps that can be employed and, thus, achievable performance. With a shortage of computational power and training data, the fully constrained implementation described in Sec. 4.3 might not be a viable option because of the large number of taps that

is necessary. However, if robustness is still desired, the method of relaxing spatial constraints can be employed as described in the following section.

4.4.3 Relaxing Spatial Constraints

In the previous analysis, a fully constrained SFT adaptive processor was implemented. The term "fully constrained" implied three sets of range constraints about the look direction and a set of N spatial constraints at T_0. In practice, the set of N spatial constraints at T_0 was implemented by a diagonal loading technique described in Sec. 4.3, whereby a large amount of diagonal loading (e.g., 100 dB) was applied to the portion of the covariance matrix corresponding to T_0. This was in addition to any diagonal loading that was applied to the entire covariance matrix as a whole. The effect of applying diagonal loading at T_0 is to prevent adaptivity from taking place at that tap, and, therefore, the weights and corresponding response at that tap will be those of the conventional processor.

The following is an investigation of the effect of varying the amount of diagonal loading at T_0. Figure 4.15 shows the two-dimensional Σ beampatterns of three processors with T_0 diagonal loading levels of 10 dB, 20 dB and 30 dB, respectively. Slices taken at T_0 are included underneath the two-dimensional beampatterns. The progression illustrates that as more diagonal loading is applied, the closer the spatial response resembles that of the conventional Σ processor. Conversely, the less diagonal loading is applied, the more "relaxed" the spatial constraints become, and the more distorted the spatial response. Similarly, the more diagonal loading at T_0 that is applied to the difference processor, the closer the spatial response resembles that of the conventional Δ processor.

There may be a number of reasons why it is beneficial to relax the spatial constraints at T_0. In terms of the beampattern, the application of full spatial constraints results in a sharp transition between the response at T_0 and neighboring taps. Such artificial boundaries suggest that full spatial constraints are themselves rather artifi-

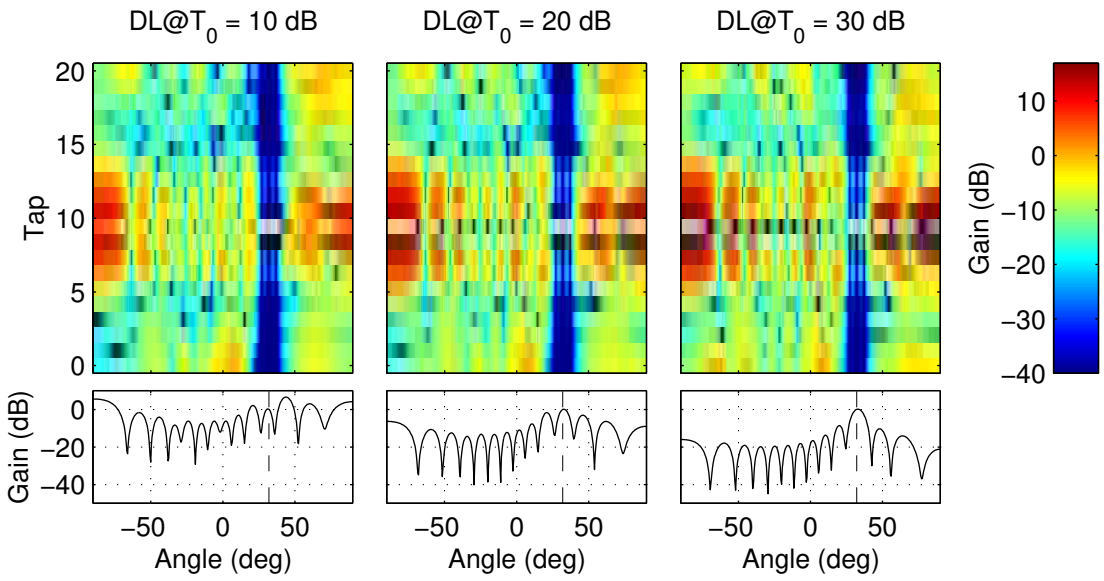

Figure 4.15: Sum Beampatterns for varying degrees of T_0 diagonal loading.

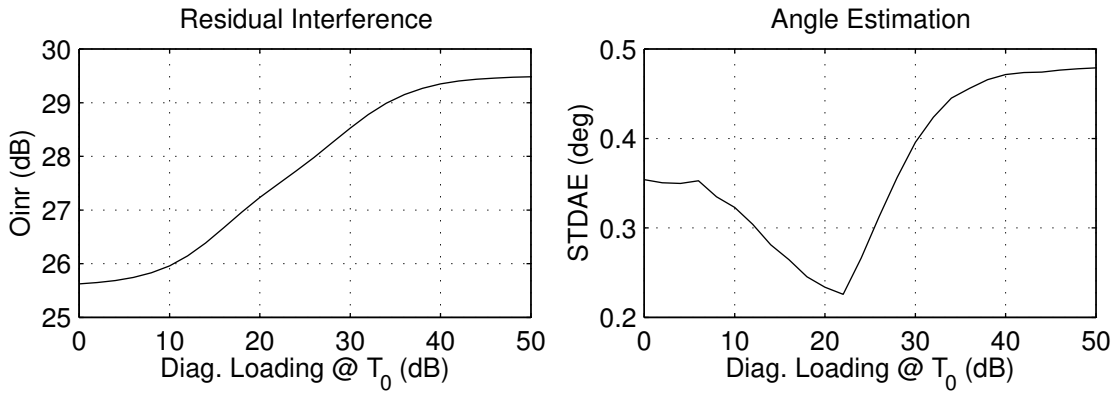

Figure 4.16: OINR and STDAE versus degree of T_0 diagonal loading (SNR = 50 dB).

cial. Inefficiency in the form of a large number of constraints may possibly contribute to loss of performance. Illustrated in Fig. 4.16 is the relationship between diagonal loading at T_0 and the resulting OINR and STDAE performance. As expected, an increase in diagonal loading at T_0 degrades OINR performance. However, STDAE performance is shown to improve up to a certain point, after which it begins to degrade again. The curve indicates that approximately 22 dB of diagonal loading at T_0 is optimal for angle estimation. This result suggests that relaxation of the constraints through the method of variable diagonal loading has some merit.

Other forms of relaxation are possible, however, not all prove feasible. One method of particular interest that is easily implemented is applying a reduced number of spatial constraints about the look direction at T_0. The resulting form of constraints is more stringent than the unity gain constraint, but more relaxed than the full set of constraints. In Fig. 4.17 the application of 3, 5 and 7 spatial constraints is illustrated for the DER Σ processor. The constraints are spaced at intervals of $\frac{1}{2N}$ in units of normalized spatial frequency. As expected, the resulting beampatterns demonstrate improvement in the spatial response at T_0 as more spatial constraints are added. Figure 4.18, however, indicates that the presence of three or more spatial constraints does not offer benefit in terms of STDAE performance.

Based on the analysis presented here, diagonal loading seems to be a more

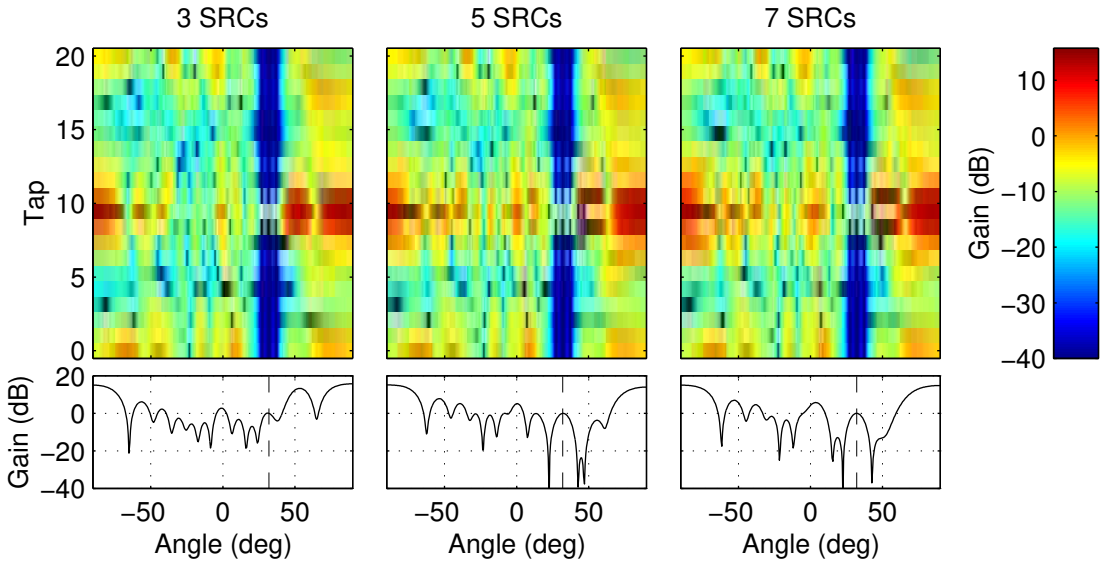

Figure 4.17: Sum beampatterns for reduced spatial constraints.

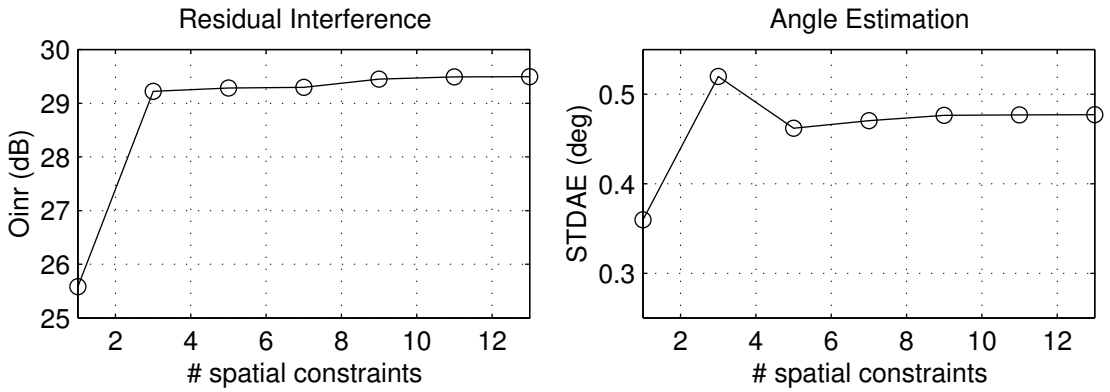

Figure 4.18: OINR and STDAE versus number of spatial constraints (SNR = 50 dB).

natural choice for spatial constraint relaxation. However, there is nothing precluding the use of a combination of the diagonal loading and reduced constraint techniques for further improvement in performance.

4.4.4 Other Results

Nonstationary TSI

Up to now, the dataset `mmit004v1` was used to evaluate SFT monopulse. This particular dataset contained TSI from a ground based jammer. Another dataset, `rio043v1`, contains TSI from an airborne jammer. Whether the radar is airborne or the jammer, it is expected that the resulting TSI will experience a Doppler shift and, therefore, can not be considered stationary [30, 28]. Provided here are a few results that verify the feasibility of the SFT monopulse processor in a nonstationary TSI and mainbeam jamming environment. In Fig. 4.19 mainbeam jamming filter outputs are shown for the conventional processor, spatial adaptive processor, and fully constrained SFT processors with 20 and 50 taps, respectively. A 50 dB synthetic target injected into the input data does not experience target cancellation, and, therefore, OINR can be used to represent mitigation performance. From the results in this figure and successive figures, it is apparent that SFT processing is even more critical for this particular dataset (containing nonstationary TSI) than for the `mmit004v1` dataset containing stationary TSI. In Fig. 4.20 STDAE versus SNR curves are shown for the four processors. For nonstationary data there is a more pronounced difference between employing 1 tap and multiple taps. In comparing Fig. 4.20 for `rio043v1` to that of Fig. 4.12 for `mmit004v1`, it becomes apparent that angle estimation performance is hampered by the nonstationarity of the TSI and mainbeam jamming. This is primarily a consequence of the reduced mitigation capability in the airborne interference environment. Recall that because reduced mitigation results in excessive interference in the sum and difference outputs and corresponding error voltage readings, angle estimates become corrupt.

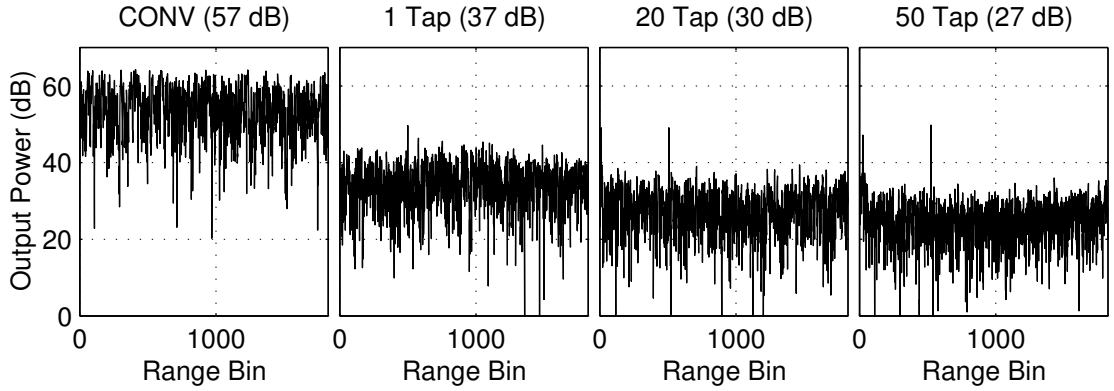

Figure 4.19: Outputs for conventional Σ processor, spatial adaptive Σ processor, and fully constrained 20 and 50 tap SFT Σ processors.

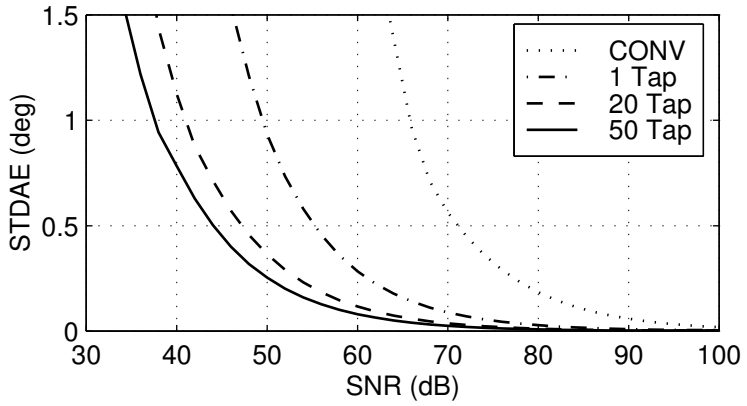

Figure 4.20: Monopulse performance curves for a conventional, spatial adaptive, 20 and 50 tap fully constrained SFT processors.

However, by no means should the results for nonstationary TSI presented here be considered a complete treatment of the topic. When considering nonstationary TSI, issues such as training interval selection and sample support have to be considered as well, topics that are beyond the scope of this thesis.

Summary from Mountaintop Datasets

Results from a number of MT datasets demonstrate that the fully constrained SFT adaptive monopulse processor does not always perform better then the spatial adaptive processor. Table 4.1 includes STDAE results for a variety of mountaintop datasets.

The 3 dB beamwidth (ϕ_{bw}) and OINR for the sum processor are provided as additional performance measures. The processors under consideration in Table 4.1 are a conventional processor (nonadaptive) and two fully constrained SFT processors with 20 and 50 taps, respectively. Note that with only one tap, the full set of constraints in a spatial processor occupy all available degrees of freedom and yield a nonadaptive processor. In Table 4.2 the processors are a unity gain spatial adaptive processor and two partially constrained SFT processors with 20 and 50 taps, respectively. For the most part Table 4.1 represents fully constrained or "robust" processing, whereas Table 4.2 represents partially constrained or "highly adaptive" processing. The majority of case entries represent mainbeam jamming scenarios. The exceptions are the entries for datasets `mmit109v1` and `mmit112v1` which both lack a direct path jammer signal [63].

In comparing OINR results in the respective tables it is clear that the SFT processors offer improvement over the corresponding spatial (1 tap) processors. For the most part this is true of STDAE performance as well. However, for some datasets neither of the fully constrained SFT processors in Table 4.1, particularly the 20-tap processor, offer an improvement in STDAE performance over the spatial adaptive processor in Table 4.2, even though OINR performance is improved. The answer

Table 4.1: Performance results for other MT datasets (SNR = 50 dB) using the full set of constraints.
[a]Contains TSI without a direct path jammer.
[b]Contains nonstationary TSI.

		Conventional			20 Tap Processor			50 Tap Processor		
Name	$\phi_{\mathbf{jam}}$	ϕ_{bw}	OINR	σ_{ϵ_ϕ}	ϕ_{bw}	OINR	σ_{ϵ_ϕ}	ϕ_{bw}	OINR	σ_{ϵ_ϕ}
mmit004v1	32.0	8.9	73.5	4.50	8.9	29.5	0.48	8.9	22.6	0.18
mmit013v1	66.2	20.6	66.3	7.73	20.6	31.7	1.35	20.6	23.1	0.43
mmit043v1	32.0	8.9	63.1	4.52	8.9	25.9	0.29	8.9	22.9	0.19
mmit044v1	32.0	8.9	63.4	4.52	8.9	25.8	0.30	8.9	23.0	0.21
mmit045v1	32.0	8.9	60.8	4.03	8.9	23.1	0.20	8.9	20.4	0.13
mmit048v1	32.0	8.9	63.4	4.58	8.9	25.9	0.30	8.9	23.2	0.21
mmit109v1[a]	32.0	8.9	46.5	2.83	8.9	30.3	0.55	8.9	21.5	0.15
mmit112v1[a]	32.0	8.9	46.3	2.84	8.9	29.5	0.48	8.9	21.5	0.16
rio042v1[b]	8.7	7.7	59.2	3.97	7.7	32.7	0.46	7.7	28.2	0.26
rio043v1[b]	10.7	7.7	57.0	3.52	7.7	30.3	0.35	7.7	26.9	0.24

Table 4.2: Performance results for other MT datasets (SNR = 50 dB) using partial constraints.
[a]Contains TSI without a direct path jammer.
[b]Contains nonstationary TSI.

		1 Tap Processor			20 Tap Processor			50 Tap Processor		
Name	$\phi_{\mathbf{jam}}$	ϕ_{bw}	OINR	σ_{ϵ_ϕ}	ϕ_{bw}	OINR	σ_{ϵ_ϕ}	ϕ_{bw}	OINR	σ_{ϵ_ϕ}
mmit004v1	32.0	4.9	32.1	0.42	4.8	25.6	0.36	4.7	17.7	0.06
mmit013v1	66.2	16.7	35.6	1.47	15.5	27.4	1.05	16.7	17.3	0.32
mmit043v1	32.0	4.7	26.2	0.15	4.6	22.3	0.12	4.8	18.8	0.06
mmit044v1	32.0	4.9	26.7	0.18	4.8	22.2	0.11	4.9	18.9	0.07
mmit045v1	32.0	5.0	24.3	0.13	4.8	19.1	0.09	4.8	16.0	0.04
mmit048v1	32.0	4.8	26.2	0.15	4.8	22.1	0.11	4.9	18.4	0.05
mmit109v1[a]	32.0	4.7	26.3	0.29	4.8	23.2	0.19	4.9	17.6	0.08
mmit112v1[a]	32.0	4.7	26.2	0.28	4.8	23.0	0.18	4.9	16.7	0.07
rio042v1[b]	8.7	6.8	39.5	0.92	5.4	31.9	0.49	4.9	27.0	0.17
rio043v1[b]	10.7	6.5	37.2	1.03	5.8	29.6	0.78	5.6	26.0	0.84

to this apparent discrepancy lies in the increased beamwidths afforded by the full constraint configuration. To motivate this hypothesis, consider the processors for datasets `rio042v1` and `rio043v1`, where the beamwidths are closer in value. For those datasets the fully constrained SFT processors offer significant improvement in STDAE performance over the unity gain spatial adaptive processor. An explanation of why the increased beamwidth makes the SFT processors appear at a disadvantage with respect to the spatial adaptive processor, even though OINR performance is clearly superior, is offered in Sec. 4.4.5.

At this point it is important to consider the consistent behavior, and, thus, robustness, of the fully constrained SFT processors under different interference conditions as represented by the different datasets. Whereas the spatial adaptive processor exhibits large variations in performance from one dataset to the next, the 50-tap fully constrained SFT processor is particularly stable. The exception is for dataset `mmit013v1` where the location of the jammer, namely at $\phi_0 = 66.2°$, results in reduced angular resolution and, hence, a loss of STDAE performance. In general, as the look direction is steered away from boresight, angular degradation results as demonstrated in the next subsection. For the partially constrained SFT processors STDAE is for the most part improved over those of the fully adaptive processors, again primarily because of the effect of reduced beamwidths (since OINR doesn't seem to suffer as much). However, robustness is clearly lost. This is most apparent from dataset `rio043v1` where the 50 tap partially constrained SFT processor fails to improve and, in fact, degrades over the 20 tap partially constrained SFT processor.

Nonmainbeam Jamming

It is interesting to note what happens when the radar gradually steers away from the jammer, and how SFT adaptive monopulse processing performs relative to spatial adaptive monopulse. The effect is shown in Fig. 4.21. Included for reference is Fig. 4.22 showing OINR and beamwidth performance for varying steer direction. The

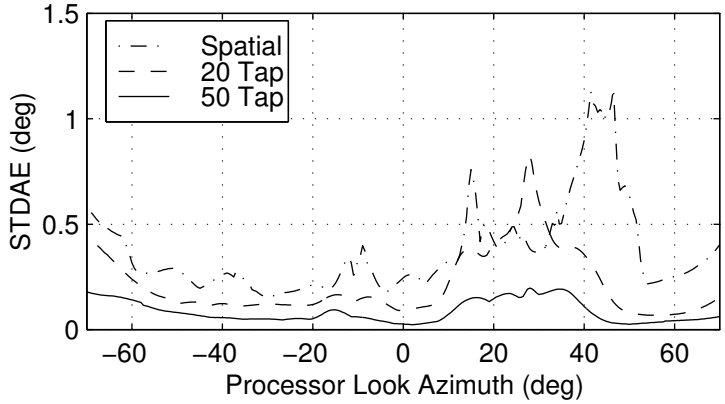

Figure 4.21: STDAE versus processor look direction (SNR = 50 dB).

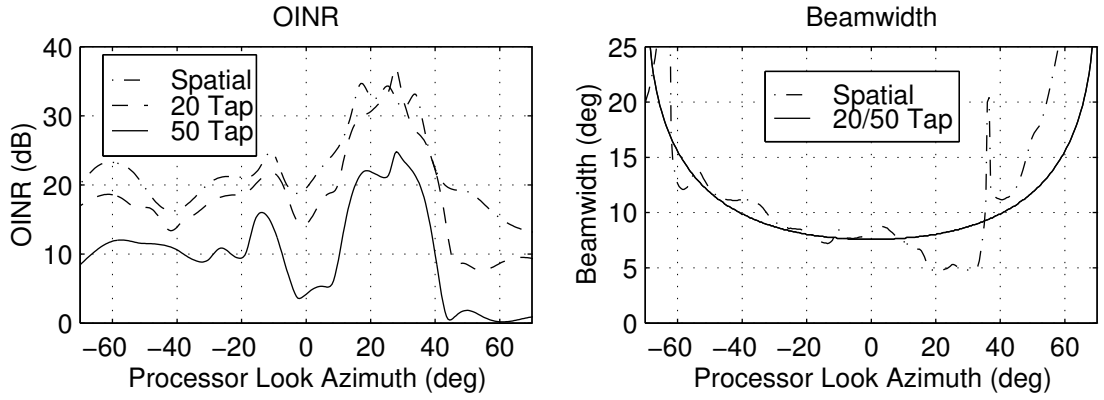

Figure 4.22: OINR and beamwidth versus processor look direction (SNR = 50 dB).

20-tap processor improves on the spatial adaptive processor everywhere except in the $20^\circ - 30^\circ$ region, which is heavy in TSI and jamming energy. The 50-tap processor, on the other hand, is equipped with sufficient TSI cancellation capability to offer improvement throughout the angular region shown.

In selecting an optimization criteria in Sec. 4.2 the argument for output power minimization rather than direct angle estimation optimization was that under most circumstances output power minimization is sufficient for near optimum angle estimation. Comparing Fig. 4.21 to Fig. 4.22 supports our assertion that STDAE performance is indeed consistent with OINR performance. In other words, where OINR performance is good, so is STDAE performance and vice versa.

Figure 4.22 shows the variation of processor beamwidth with steering direction. As the monopulse sum beam is steered away from boresight (0°), the Σ beamwidth increases for all processors; a consequence of diminishing angular resolution in the array at angles away from boresight. As will be explained in Sec. 4.4.5, increased beamwidths cause degradation to STDAE performance as measured here. Thus, STDAE performance degrades near the edges, whereas OINR performance remains constant. Of particular interest is that for most of the angular spectrum, the beamwidth of the spatial adaptive processor is roughly equivalent to that of the SFT processors, while in regions heavy in TSI and mainbeam jamming its beamwidth is diminished. Likewise, in regions of reduced angular resolution (i.e., at the edges), the spatial adaptive processor suffers from excessively large beamwidth. The SFT processors, on the other hand, exhibit consistent beamwidths because that is the nature of the constraints with which they are equipped.

4.4.5 Beamwidth Analysis

In comparing different processors it was noted that the angular extent of the mainbeam varies with processor configuration. For example, in Fig. 4.23 the conventional processor has a beamwidth of 8.9°, whereas the spatial adaptive processor has a

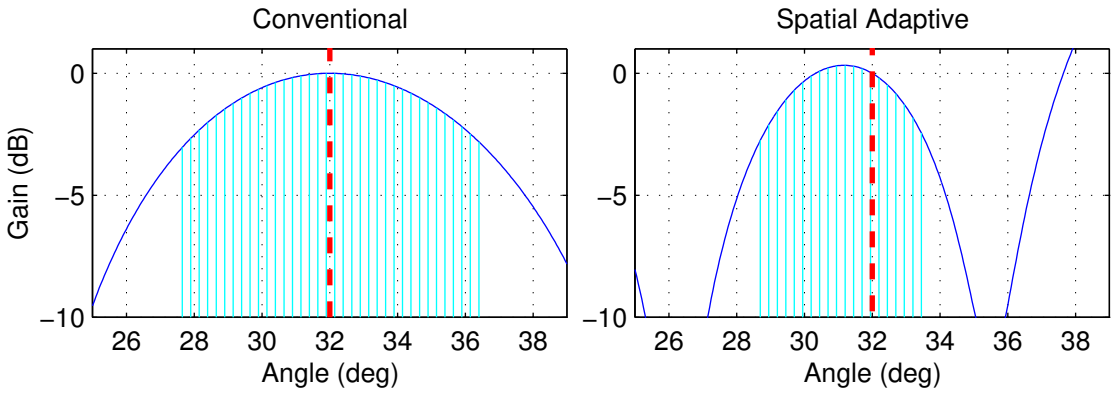

Figure 4.23: Mainbeams of a conventional and spatial adaptive processor with look direction marked in red (dashed line).

beamwidth of 4.85°. As discussed next, results used in comparing processors of different beamwidths may be biased, thus, favoring one processor over the other. Consider the 50 tap fully constrained SFT processor in Table 4.1 and the spatial adaptive processor in Table 4.2 both for dataset entry `mmit043v1`. The SFT processor resulted in an OINR of 22.9 dB and an STDAE of 0.19°, whereas the spatial processor resulted in an OINR of 26.2 dB and an STDAE of 0.15°. Thus, we have an improvement in OINR performance but a degradation in STDAE performance. Noting the different beamwidths of the two processors leads us to suspect that the discrepancy in performance lies in the variant beamwidths.

Experimentally, STDAE is determined through Monte Carlo simulations [49] with targets injected randomly across range and angle within the mainbeam and the corresponding angle errors averaged over range

$$\hat{\sigma}_{\epsilon_\phi}(\phi) = \sqrt{\sum_t |\hat{\phi}(\phi, t) - \phi|^2}, \tag{4.16}$$

where ϕ is an angle within the mainbeam and t is a fast-time index. When the angle dependency is not desired, a worst case STDAE is reported:

$$\hat{\sigma}_{\epsilon_\phi} = \max_{\phi} \left\{ \hat{\sigma}_{\epsilon_\phi}(\phi) \right\}. \tag{4.17}$$

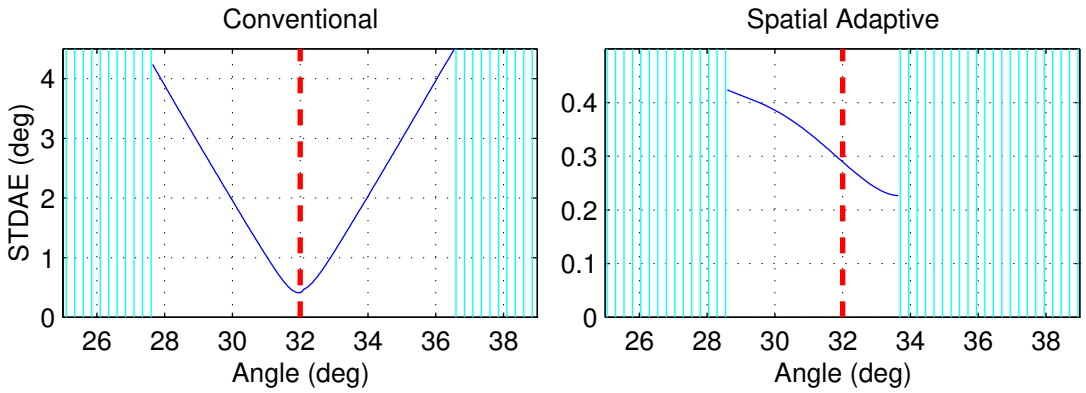

Figure 4.24: STDAE performance for SNR=50 dB as a function of true target angle. Look direction marked in red (dashed line).

Typically, the worst case occurs on the mainbeam edges where angle estimates are not as accurate. This effect is illustrated in Fig. 4.24.

In Fig. 4.24 STDAE is plotted for the spatial adaptive and conventional processors whose beampatterns were shown in Fig. 4.23. The target SNR was fixed at 50 dB and the angles at which targets are injected was varied across the mainbeam of the respective processors. It is evident that the resulting angle estimates become progressively worse for targets that are injected farther away from the look direction (i.e., 32°). This suggests that wide beamwidth processors may be at a disadvantage over narrow beamwidth processors for this method of measuring STDAE.

One way to eliminate such biasing is through beamwidth compensation. That is, rather than injecting targets throughout the mainbeam of each processor and then taking the worst case STDAE reading, inject targets only in an interval of the mainbeam shared by all processors. For example, consider Fig. 4.25 illustrating how the 3 dB points of the mainbeam shift as the diagonal loading at T_0 is gradually increased from 0 dB to 70 dB (diagonal loading at T_0 was discussed in the context of constraint relaxation in Sec. 4.4.3). The blue shaded area corresponds to the region of the mainbeam. Notice that for 0 dB diagonal loading the beam is biased to the left, at 25 dB the mainbeam is biased to the right, and beyond 50 dB it is balanced.

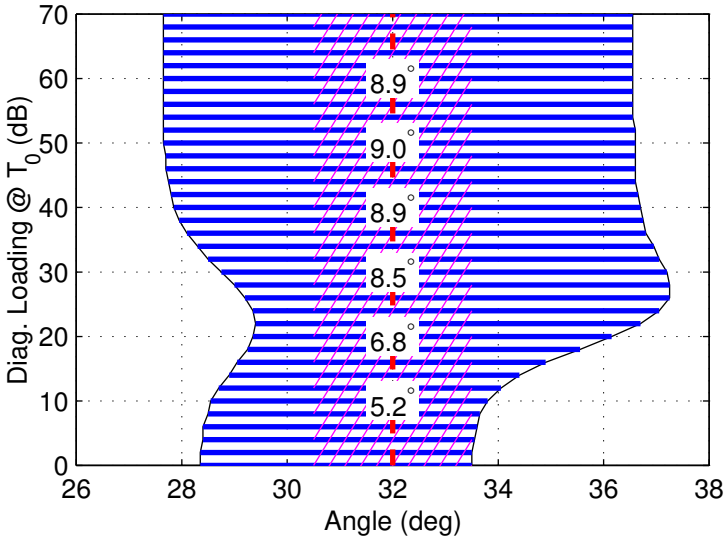

Figure 4.25: Effect of variable diagonal loading at T_0 on beamwidth. Look direction marked in red (dashed line).

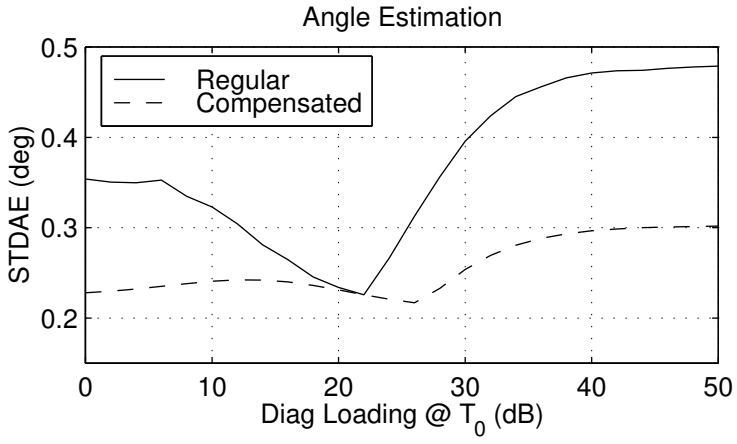

Figure 4.26: STDAE vs. diagonal loading at T_0 revisited – with and without beamwidth compensation.

Also note the gradual decrease of beamwidth as the amount of diagonal loading is decreased. When worst case STDAE results are reported across the entire mainbeam, the solid-line curve of Fig. 4.26 results. However, when worst case STDAE results are reported across a fixed interval about the look direction, as indicated by the cross hatched region in Fig. 4.25, the dashed-line curve of Fig. 4.26 results. Considering the uncompensated curve, roughly 22 dB of diagonal loading at T_0 results in peak performance, representing a dramatic improvement in performance over 0 dB diagonal loading. When considering the compensated curve, roughly 27 dB of diagonal loading results in peak performance, but the improvement is hardly significant. Clearly the dramatic results attained without the use of beamwidth compensation prove far less dramatic with compensation.

Despite the argument presented for beamwidth compensation, it was opted to not utilize it in this thesis. Results obtained from beamwidth compensation are not fully representative of the individual processors, because they do not test the processors in their full range of operation. Since we are interested in robustness, a comparison that does not apply to the full range of operation does not accurately reflect the sacrifice in performance incurred for the added robustness. Furthermore,

the use of beamwidth compensation can confuse the reader to think that the results presented are inconsistent. For instance, STDAE results for one particular processor might vary from one comparison to the next depending on what portion of its beamwidth is being utilized, which, in turn, depends on the processors under evaluation.

An alternative and simpler method for measuring angle estimation performance is to normalize the STDAE results to the processor's beamwidth, ϕ_{bw},

$$\bar{\sigma}_{\epsilon_\phi}(\phi) = \sqrt{\sum_t \left| \frac{\hat{\phi}(\phi, t) - \phi}{\phi_{bw}} \right|^2}. \tag{4.18}$$

Unlike beamwidth compensation, this measure of STDAE performance can test the processor in its full range of operation, and, yet, avoid being biased towards larger beamwidth processors. In fact, in the literature it is common for angles to be expressed in terms of beamwidths units rather than degrees [60, 20, 39, 41, 40].

Since the results in this thesis are largely experimental and the focus is on both angle estimation performance and robustness, neither beamwidth compensation nor the normalized STDAE measure are employed extensively. When comparing a spatial adaptive processor to SFT processors, instead of using beamwidth compensation or normalized STDAE, it was opted to include results for the fully constrained as well as the partially constrained SFT processor. The merit of SFT processing was demonstrated by comparing the spatially adaptive processor to partially constrained SFT processors, since both have similar beamwidths. On the other hand, comparing the spatially adaptive processor to fully constrained SFT processors provides a sense of the tradeoff involved between STDAE performance and robustness.

4.4.6 Transmit-Receive Patterns

Figure 4.27 illustrates the effect of a directional transmission beampattern such as the one found in the Mountaintop radar. The adapted receiver pattern is that of a unity gain spatial adaptive processor. For a processor performing detection, the

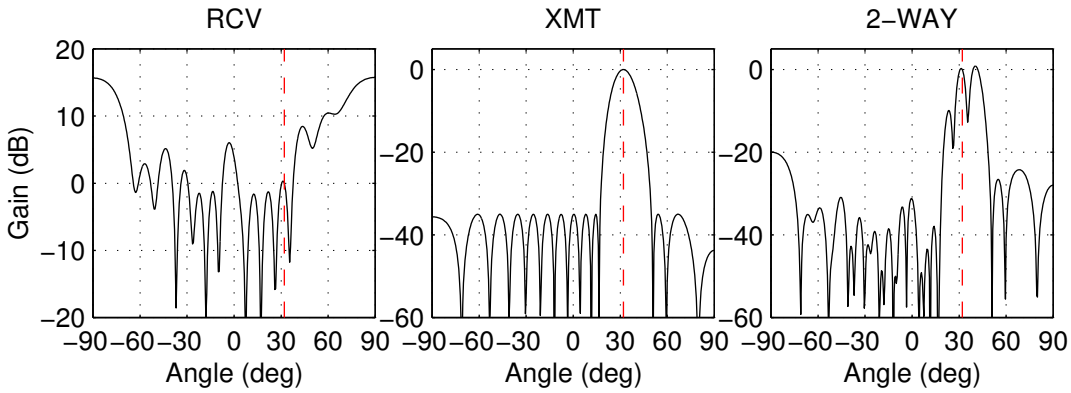

Figure 4.27: Adapted receive beampattern, transmit beampattern, and two-way receive beampattern. Look direction marked in red (dashed line).

high sidelobes pose a serious false alarm threat if additional targets are present in the sidelobes [33, 37]. For a monopulse processor, targets entering through the high sidelobes corrupt the monopulse output and, thus, angle estimates. Ordinarily, such a poor response would render a processor unacceptable. However, the severity of the problem is somewhat muted if the directional characteristics of the radar transmitter are taken into account. The directional transmission beampattern illustrated in the center of Fig. 4.27 is taken to be that of a 35 dB Chebyshev tapered steering vector in a look direction of 32°, such as was used for much of the Mountaintop data [33, 37].

As demonstrated by the two-way response in the right of Fig. 4.27, what used to be unacceptably high sidelobes are now at least 20 dB below the mainbeam. Despite the reduced sidelobes, however, certain vulnerabilities to false alarms still exist, particularly within the vicinity of the mainbeam. Reducing the high gain artifacts near the mainbeam requires a narrower transmission beam. For a fixed number of transmit/receive elements this has to come at the expense of higher sidelobes. Furthermore, the transmit pattern is typically fixed in the radar and is not subject to variation.

The two-dimensional two-way sum and difference patterns for a fully constrained 20 tap processor are shown in Fig. 4.28. Once again, what used to be

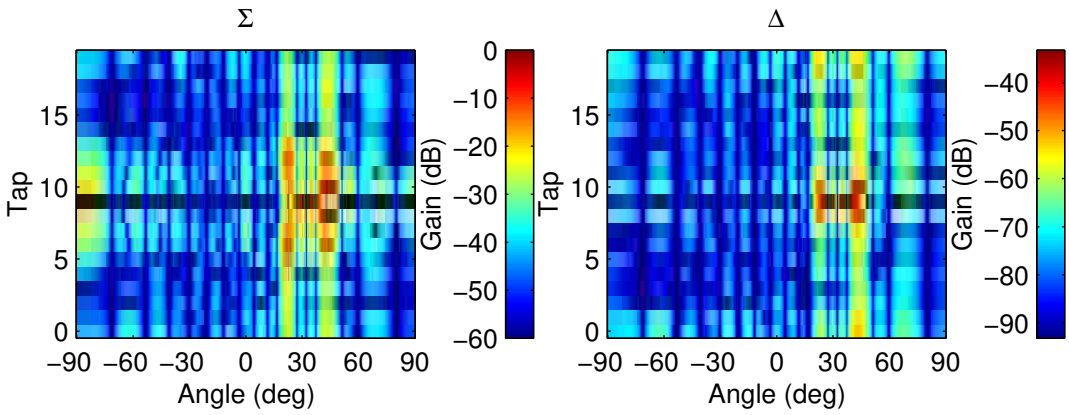

Figure 4.28: Two-way sum and difference beampatterns for 20 tap processor.

unacceptable sidelobes in Figure 4.11 are now far more acceptable. Certain gain artifacts near the mainbeam and successive taps, however, still remain as they did in the spatial case. Since the spatial constraints prevent the artifacts from showing up at T_0 they appear in the successive taps.

An issue that arises when employing a two-way beampattern is how to define the processor beamwidth. For identical transmit and receive beampatterns, a 6 dB beamwidth is most appropriate [61]. That is, the 3 dB beamwidth of the one-way pattern is equal to the 6 dB beamwidth of the two-way pattern, and, therefore, it is not necessary to indicate the type of beampattern to which the specified beamwidth applies. However, when the transmit and receive beampatterns differ, as in Fig. 4.27, the 3 dB beamwidth of the one-way or receive beampattern (left) is not equal to the 6 dB beamwidth of the two-way beampattern (right). In such cases, it is simplest to apply the 3 dB beamwidth definition to both the one-way and two-way beampatterns. When the receive beamwidth is narrower than the transmit beamwidth, as it typically is, then at least the two-way beamwidth is only slightly narrower than the one-way beamwidth.

4.5 Conclusions

The main innovation introduced in this chapter is a method by which a monopulse processor is combined with an adaptive space/fast-time processor to provide a precise angle tracking capability in the presence of TSI and mainbeam jamming. Key features of the new processor are a tap-centered configuration, extended range constraints, and spatial response constraints. Range constraints play a key role when the transmitted waveform is spread in time (e.g., LFM) and pulse compression follows TSI processing. Range constraints in the look direction are intended to prevent spreading throughout the mainbeam, but the application of spatial constraints at T_0 imposes such a burden on the processor that spreading within the mainbeam becomes a problem. Therefore, additional range constraints about the look direction become necessary.

Previous work has shown no clear advantage to using different tap configurations. Here, however, for monopulse it has been demonstrated that a combination of forward and backward prediction is essential when spatial response constraints are applied. As demonstrated through simulation results, spatial response constraints play a key role in maintaining consistent performance and low distortion in the sum and difference responses; particularly, in a mainbeam jamming scenario. Constraint relaxation via variable diagonal loading at the constraint tap was shown to offer slight advantage in terms of mitigation and angle estimation performance with little or no sacrifice in the sum and difference responses.

The majority of simulation results in this chapter were confined to two Mountaintop datasets containing stationary and nonstationary TSI. In either case, the SFT processor proved meritorious over the spatial adaptive processor. A limited set of simulation results for a more comprehensive set of datasets demonstrated the robustness of the proposed algorithm under different TSI conditions, including when a direct path jammer is lacking. The merit of the SFT processor was also demonstrated for the nonmainbeam jamming scenario.

The chapter concluded by addressing two concerns that arose in presenting

mainbeam jamming results. In particular, the high sidelobes in the beampattern responses were shown to be far less problematic when considering the directional transmit/receive characteristics of the Mountaintop radar. The favorable bias in angle estimation performance for processors possessing narrower beamwidths was shown to be an artifact of the method employed for measuring STDAE. Other methods of measuring STDAE were proposed but ultimately rejected on the grounds that they fail to consider the tradeoff between angle estimation performance and robustness.

CHAPTER 5

Combined TSI and MSC Processing

Monostatic clutter (MSC) is commonly encountered together with TSI and jamming. Since MSC is correlated in space and slow-time, the SFT processing used for TSI mitigation is ineffective for MSC. One approach suggested in [31, 36], the factored beamspace algorithm (FBA), cascades a set of TSI filters with an MSC filter. The resulting cascade architecture works by initially cleansing the data of TSI using SFT processing, and then removing the remaining MSC with SST processing. However, certain shortcomings of the FBA discussed below motivate us to search for alternatives. In this chapter we introduce a reduced rank algorithm, Beam Augmented STAP (BASTAP), that overcomes some of the shortcomings of the FBA. BASTAP is shown to offer improved performance under stationary conditions and equivalent performance under nonstationary conditions.

The chapter begins by pointing out the shortcomings of the FBA and motivating the need for an alternative. A discussion of STAP and some of its strengths ensues. The BASTAP filtering mechanism and optimization criteria are then presented. Various architectural interpretations are provided to supplement a further understanding of BASTAP. An extended BASTAP architecture is then presented for use with nonstationary TSI. Finally, extensive evaluations of BASTAP, FBA, and STAP are performed with combined experimental TSI and synthetic MSC data.

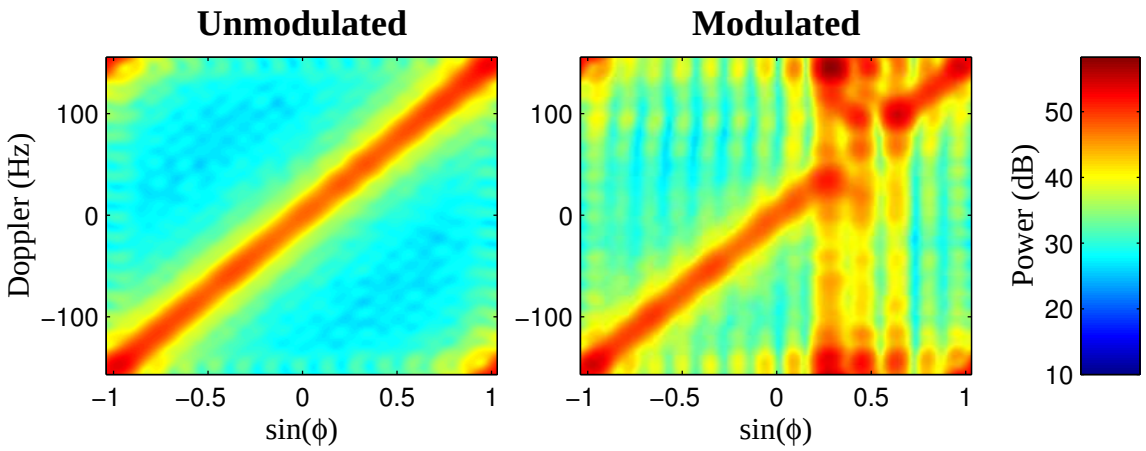

Figure 5.1: Modulation effect in the Factored Beamspace Algorithm.

5.1 Motivation for BASTAP

Two factors motivate us in the pursuit of an alternative architecture to FBA. The first goal is to take advantage of the benefits offered by STAP in terms of MSC and jamming cancellation. Avoiding the shortcomings of the FBA is the second goal. As discussed next, both of these criteria have an ultimate impact on the proposed architecture.

5.1.1 Shortcomings of the FBA

While the FBA is computationally more viable than the fully adaptive joint processor (i.e., one that adapts on all element and pulse data from T consecutive taps), it has some serious drawbacks. First of all, the FBA requires MSC-free training data [36]. Although such data can typically be obtained from far range cells, in a nonstationary TSI environment the TSI in far range cells may differ significantly from that in near range cells. The second and more severe problem is that of MSC modulation [51]. Modulation occurs as the spatial response of a TSI processor degrades dramatically when the look direction is on or near the jammer and TSI. Since in the factored approach there are N orthogonal beams, one or more of them will always point

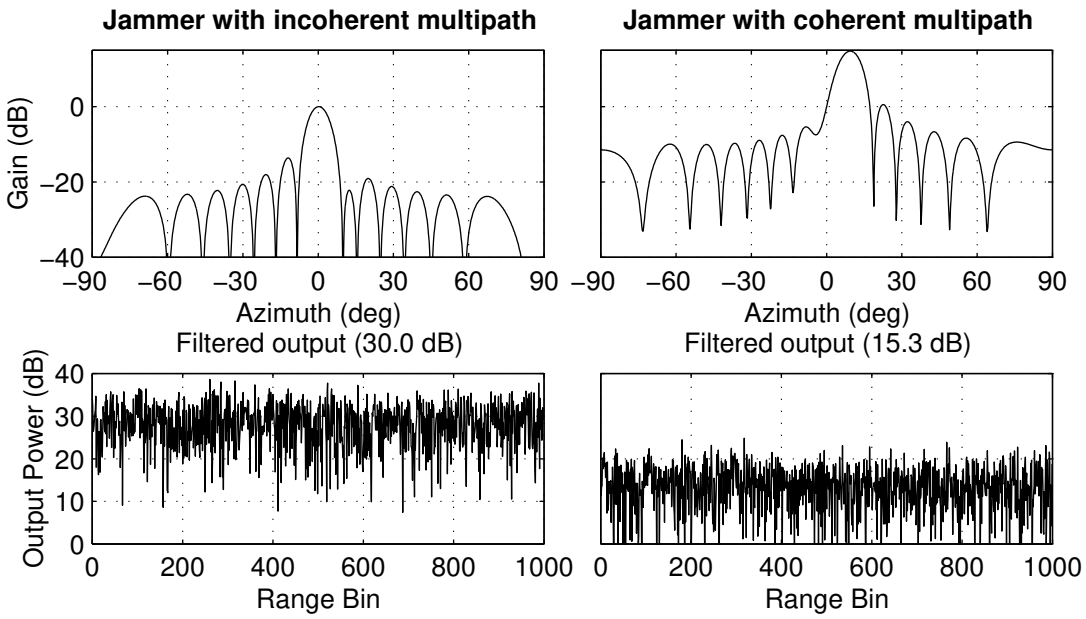

Figure 5.2: Mainbeam jamming with incoherent multipath and coherent multipath.

towards the jammer and TSI region. The distortions in the response of those beams in turn cause the MSC passing through the TSI processor to spread across angle – an effect referred to as modulation. In Fig. 5.1, the effect of modulation is demonstrated. Shown on the left is the power spectrum of data containing synthetic MSC. Shown on the right is the distorted MSC after TSI mitigation. The jammer and TSI in the original Mountaintop dataset `mmit004v1` occupy a region from approximately 0.2 to 0.6 of the $\sin(\phi)$ spectrum, which is where the resulting MSC artifacts appear strongest. Note that without the use of diagonal loading the artifacts appear even more pronounced than shown in the figure. The SST processor of the second stage of the FBA is not able to cope well with the modulated form of the MSC, and a significant loss of performance is incurred.

5.1.2 STAP in a Combined TSI, MSC, and Jamming Environment

Experimental results on Mountaintop data show that STAP does not perform as poorly as expected in the combined interference environments. This result is not altogether surprising since the major sources of interference are MSC and jamming, which can be removed through STAP. Furthermore, TSI can be partially mitigated with spatial processing. It is, however, surprising that STAP is still able to perform relatively well in the presence of mainbeam jamming. A target that lies in the direct path of a jammer is completely obscured, provided sufficient jamming power is available. Additionally, no degree of spatial nulling will help since any spatial nulling of the jammer consequently nulls the target. The reason that some amount of spatial suppression of mainbeam jamming is attained lies in the specifics of the Mountaintop radar. The Mountaintop radar utilizes 200 kHz bandpass filters at the front end of its receivers to reduce matched filter sidelobes [8]. Thus, TSI returns arriving from a few closely spaced directions effectively have the same delay, resulting in spatial correlation of the TSI with itself and the jammer signal. Once there is spatial correlation between the jammer and surrounding TSI, significant cancellation of the jamming can take place without ever using fast-time taps [32, 33, 37]. To demonstrate, consider a 30 dB jammer located at 0° and a 15 dB replica (multipath) located at 10°. For a white jammer signal, the jammer signal and its multipath replica are coherent when they have the same delay and incoherent otherwise. In one scenario, the replica is incoherent with the mainbeam jamming signal, and, therefore, it is not expected that the multipath will aid in suppressing it. In a second scenario, the replica is coherent with the mainbeam jamming signal. Figure 5.2 shows beampatterns and filtered outputs for the incoherent and coherent cases. As expected, no cancelation of the mainbeam jammer takes place when the multipath component is incoherent with the mainbeam jammer. On the other hand, if the multipath component is given the same delay as the mainbeam jamming signal and, thus, made coherent, then 15 dB

of suppression results. However, suppression of the mainbeam jammer comes at the expense of a distorted beampattern.

5.2 Beam Augmented STAP

Based on the argument for STAP, the resulting architecture has as its principal component a fully adaptive STAP processor. The spatial processing performed by the STAP processor can then accomplish significant spatial nulling of the mainbeam jammer. On the other hand, fast-time processing, expected to provide only marginal improvement in cancelation performance, is auxiliary and, therefore, need not be allotted the same degree of flexibility as the STAP processor. Consequently, for the proposed approach, fast-time taps are applied only to a single beam formed in space and slow-time, rather than to individual pulses and elements.

5.2.1 Filter Mechanism

Such a filter mechanism is illustrated in Fig. 5.3. In this architecture, MN weights are applied to all elements and pulses in the first tap (i.e., STAP weights). Additionally, an auxiliary beam in angle and Doppler is formed and weights applied to $T-1$ fast-time taps of that beam. The auxiliary beam is defined as

$$\mathbf{A}(t)^T = \mathbf{F}(\nu_1, \bar{f}_1)^H \left[\begin{array}{cccc} \mathbf{X}(t-1) & \mathbf{X}(t-2) & \cdots & \mathbf{X}(t-T+1) \end{array} \right], \tag{5.1}$$

where $\mathbf{F} = \mathbf{v}(\nu_1, \bar{f}_1)$ is a conventional, nonadaptive spatial/Doppler beamformer. In Eq. (2.21) which relates output to input, the input vector, $\mathbf{Y}(t)$, is defined as

$$\mathbf{Y}(t) = \left[\begin{array}{c} \mathbf{X}(t) \\ \mathbf{A}(t) \end{array} \right]. \tag{5.2}$$

With a filter architecture at hand, an adaptation scheme is required. It is most straight forward to optimize all the weights simultaneously using Eq. (2.24) and apply

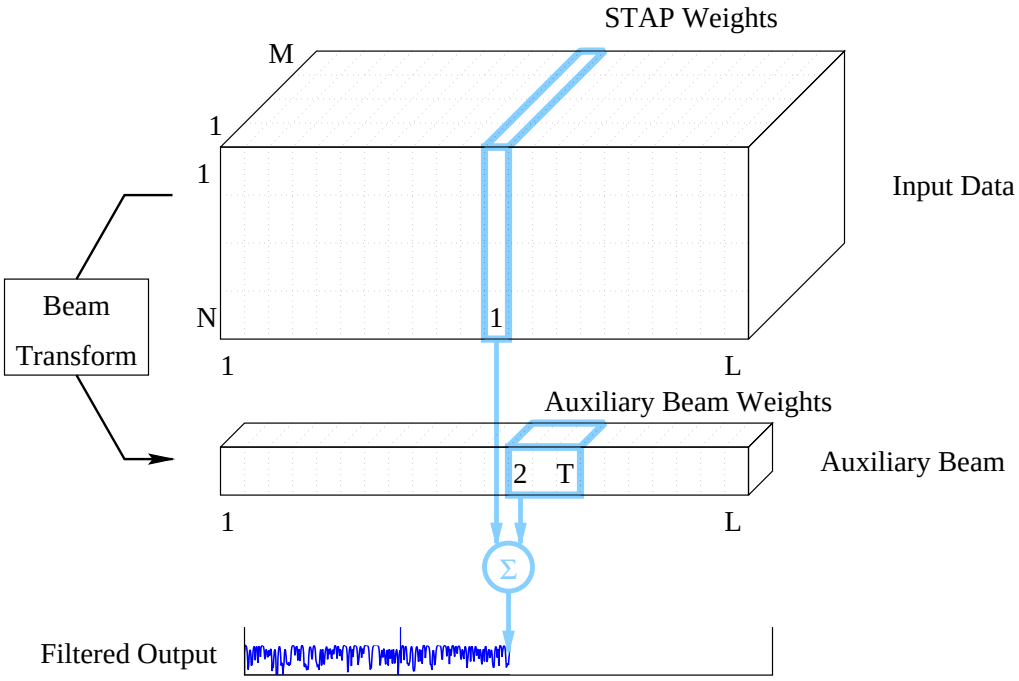

Figure 5.3: Beam Augmented STAP architecture.

a set of constraints to achieve the desired response characteristics. The unity gain constraint specified by constraint matrix and vector

$$\mathbf{C} = \mathbf{v}(\nu_0, \bar{f}_0)^H, \qquad \mathbf{c} = 1, \tag{5.3}$$

offers the most straight forward BASTAP design. The constraint guarantees that a target at the look direction and look Doppler passes through the filter with unity gain. Although no range constraints have been applied to prevent target spreading, it will become evident from the experimental results that none are needed. Estimation of the covariance matrix, $\bar{\mathbf{R}}_{\mathbf{Y}}$, can be accomplished using the SMI technique as discussed in Chapter 2. Unlike the FBA which requires an "MSC free" training dataset for training of the TSI filters in the first stage in addition to the combined TSI and MSC training dataset, BASTAP only requires the combined training dataset. Since both sets of STAP weights and auxiliary fast-time weights are optimized together, STAP performance can only be improved upon, and there is no concern that fast-time processing comes at the expense of STAP processing.

5.2.2 Block Diagram of BASTAP Architecture

The approach presented, *beam-augmented STAP* (BASTAP), employs both raw data in the main channel and beamformed data in the auxiliary channel. The structure has adaptive weights in the upper branch and adaptive tapped delay lines in the lower branches, as shown in Fig. 5.4.

The BASTAP architecture in Fig. 5.4 provides additional insight into the algorithm at hand and helps us identify where potential improvement to other architectures could be introduced. For instance, the single reference beam canceler in [46, 18, 31] presently utilizes a conventional beamformer in the upper branch and an adaptive tapped delay reference beam in the lower branch. As with BASTAP, it could be made to utilize adaptive spatial weights in the upper branch as well. The resulting architecture could then be viewed as a special case of BASTAP (i.e., one pulse

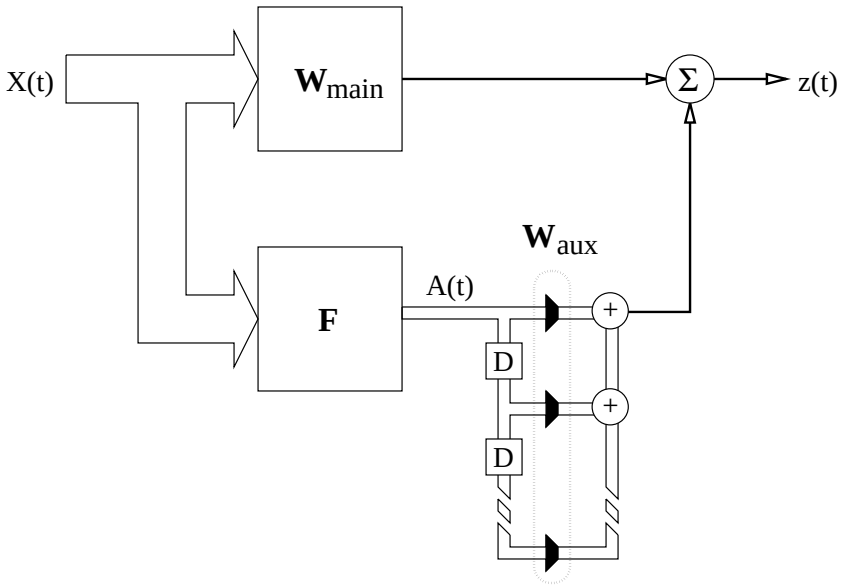

Figure 5.4: Block Diagram of BASTAP.

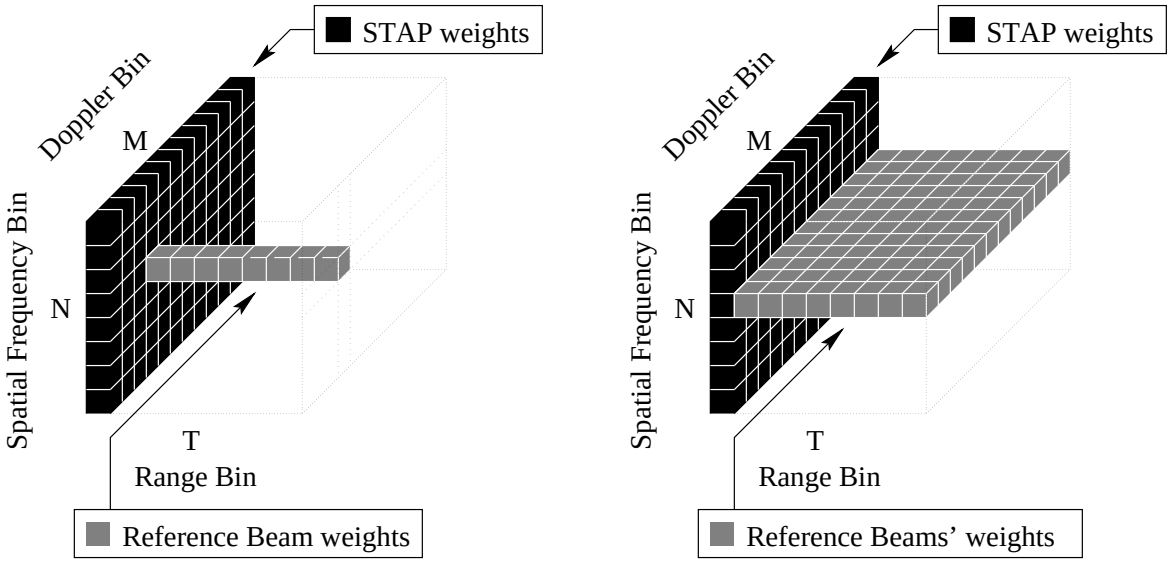

Figure 5.5: Alternative interpretation to BASTAP.

BASTAP). We see that BASTAP is a reduced rank space/fast-time/slow-time processor, in other words it operates in a three-dimensional subspace. The nature of the 3D subspace becomes even more evident with a beamspace-Doppler interpretation.

5.2.3 Alternative Interpretation

A different interpretation of BASTAP utilizing beamspace data is illustrated in Fig. 5.5a. A two-dimensional DFT is applied across all elements and PRIs at each range cell. Weights (shown in black) are then applied across all spatial and Doppler bins from the first tap, i.e., the STAP portion of the processor. Fast-time weights are then applied across $T-1$ taps from a single selected beam indicated by the gray shaded cubes.

5.3 Extended-BASTAP

The BASTAP architecture is not restricted to a single beam. Multiple beams can be used to enhance performance in the presence of nonstationary TSI, such as that present in airborne radar data. In fact, such TSI has correlation not only in fast-time but also in slow-time. Thus, it is necessary to apply beams across all Doppler bins from a single spatial frequency bin, as depicted in Fig. 5.5b. This structure is similar in concept to the application of Doppler compensation channels [19, 30, 28]. For multiple beams, $\mathbf{Y}(t)$ is defined as above in Eq. (5.2), with the beam transformation $\mathbf{F}$ having multiple spatial/Doppler filters:

$$\mathbf{F} = \left[\begin{array}{cccc} \mathbf{v}(\nu_1, \bar{f}_1) & \mathbf{v}(\nu_2, \bar{f}_2) & \cdots & \mathbf{v}(\nu_{N_b}, \bar{f}_{N_b}) \end{array} \right]. \tag{5.4}$$

Once we have introduced a multiple reference beam extension of BASTAP, it is easy to talk about any number of other architectures that utilize some odd combination of beams and taps. Referring to Fig. 5.5b it is not difficult to imagine beams in the beamspace-Doppler domain having thinned weights, multiple beams that span different lengths, or perhaps beams centered about the 0^{th} tap as we had with the tap-centered configuration in Sec. 4.4. Since the choices are seemingly endless this thesis considers only a selected number of extended BASTAP architectures.

5.4 Computational Issues

In order to provide a basis for the fair comparison of the three competing algorithms BASTAP, STAP and FBA, it is necessary to consider the computational and training requirements of each. Since all of the algorithms at hand in one way or another employ Eq. (2.24) for computing weights, the predominant source of computations are the estimation and inversion of the covariance matrix. Both estimation and inversion of a $D \times D$ covariance matrix require on the order of D^3 computations. For STAP only a single covariance matrix of dimension MN needs to be considered. For FBA

a set of M covariance matrices of dimension NT (one for each pulse) need to be considered for the first stage and one covariance matrix of dimension MN for the second stage. For BASTAP one covariance matrix of dimension $MN + N_b(T-1)$ needs to be considered, where N_b is the number of reference beams.

For STAP and FBA the associated covariances and their inverses are suitable for any processor look direction and Doppler. However, for BASTAP, since reference beam placement may depend on the assumed Doppler, it may be necessary to compute multiple processors utilizing different covariance matrices in order to cover the desired Doppler spectrum. For instance, BASTAP with a single reference beam only works well for targets possessing the same Doppler as the reference beam. Therefore, for complete Doppler coverage it is necessary to consider M covariance matrices. Extended BASTAP, on the other hand, already employs M reference beams distributed evenly across Doppler, and, therefore, only one covariance matrix need be considered.

With the ever increasing computational power of modern computing devices to meet the computational demands of radar processors, sample support or the availability of sufficient training samples for estimating the covariance matrix is often the limiting and, thus, critical factor in selecting a processor size. As a general rule of thumb, estimating a covariance matrix of dimension $D \times D$ requires the availability of $2D$ snapshots at successive time instants. An estimate employing $2D$ training snapshots results in a 3dB SINR performance loss with respect to the true covariance matrix in (2.24) [52, 4]. For STAP and BASTAP arriving at the sample support is straightforward, whereas with FBA it is slightly more complicated because of the more complicated structure involved. Furthermore, FBA requires an additional "clutter free" training set (i.e., containing only TSI).

Another useful and related performance parameter to consider is the blind interval [31]. The blind interval is defined here as the temporal extent of the filter, or, in other words, the number of snapshots necessary to fill up the extent of the filter [31]. Table 5.1 summarizes the computational requirements, degree of sample

Table 5.1: Computational and sample support requirements.

NAME	**BASTAP**	**FBA**	**STAP**
Computational Complexity	$[MN + N_b(T-1)]^3$	$M(NT)^3 + (MN)^3$	$(MN)^3$
Sample Support	$MN + N_b(T-1)$	$MN + NT$	MN
Blind Interval Length	T	T	1

support necessary for training, and blind intervals of the respective processors.

5.5 Simulation Results for BASTAP

Performance results for BASTAP were obtained for MT dataset `mmit004v1` containing a direct path jammer at 32° and stationary TSI, and for MT dataset `hot6067v1` containing a direct path jammer at −2° and nonstationary TSI. In both instances datasets were combined with 40 dB of synthetic MSC and injected with a 50 dB synthetic target with a −100 Hz Doppler shift. The three processors considered were BASTAP, fully adaptive STAP, and FBA.

The synthetic MSC was generated by the Mountain Top Matlab Toolbox[1] `simit` tool which utilizes a simple sandpaper monostatic clutter model. The power spectrum of the synthetic clutter was already shown in the MSC modulation example on the left hand side of Fig. 5.1. The clutter ridge has a slope of approximately 1, corresponding to the maximum allowable unambiguous platform velocity with no platform misalignment. When evaluating STAP and BASTAP, the synthetic MSC is injected throughout range. When evaluating FBA the MSC is only injected in the first 1000 samples, leaving sufficient MSC-free training samples for the TSI pre-processor.

Initially, the interference suppression performance of BASTAP is evaluated and compared to that of FBA and STAP for the case of stationarity TSI. Then, a qualitative evaluation and comparison of beampattern responses of the various

[1]The Mountain Top Matlab Toolbox is presently available on the Yaron Seliktar's web site at `www.ece.gatech.edu/users/yaron`

processors is given. A similar analysis of interference suppression and beampattern responses is provided for nonstationary TSI. Both sidelobe and mainbeam jamming are considered in all of the analyses. Additionally, a number of analyses that focus on a particular parameter and its effect on the performance of BASTAP, STAP, and FBA are included. Variation of look Doppler in a mainbeam jamming scenario demonstrates consistency and also provides additional insights into the workings of the various algorithms. Variation of MSC clutter power combined with the TSI and jamming provides additional insights into the workings of the various algorithms and places a perspective on how to view the other results presented. An analysis of reference beam placement then follows. As in the previous chapter, summary results for other MT datasets are tabulated.

5.5.1 Computational Issues

A fair comparison between BASTAP and FBA entails matching up the different performance parameters as best as possible. However, as can be inferred from Table 5.1, matching up one parameter results in a mismatch of another. Since it is, therefore, impossible to attain a completely fair comparison, the following analyses focus on the number of adaptive weights in BASTAP and the number of adaptive weights per pulse in the first stage of FBA. Tables 5.2 and 5.3 detail the performance parameters that apply to the comparitive analyses that follow. In order to facilitate reading the table entries, the computational requirement and sample support figures are expressed relative to those of STAP. Since BASTAP and extended BASTAP are employed under stationary and nonstationary conditions, respectively, it is necessary to consider the processor configurations separately for the different environments. Table 5.2 applies to processing under stationary conditions, whereas Table 5.3 applies to processing under nonstationary conditions.

Table 5.2: Computational complexity and sample support requirements for stationary configuration.

NAME	**BASTAP**	**FBA**	**STAP**
Computational Complexity	3x	32.5x	x
Sample Support	1.44y	2.25y	y
Blind Interval	100	25	1

Table 5.3: Computational complexity and sample support requirements for nonstationary configuration.

NAME	**BASTAP**	**FBA**	**STAP**
Computational Complexity	20x	251x	x
Sample Support	2.7y	3.5y	y
Blind Interval	25	40	1

5.5.2 Stationary TSI

In analyzing the three processors on stationary TSI data, the assumed target direction and Doppler were 0° and −100 Hz for sidelobe jamming and 32° and −100 Hz for mainbeam jamming. BASTAP was configured with a 99-tap reference beam ($T = 100$) pointed at the jammer (i.e., 32^o) for sidelobe jamming and at 10° for mainbeam jamming and in both cases tuned to −100 Hz. FBA was configured with 25 taps in the first stage and a fully adaptive STAP processor in the second. For these configurations BASTAP totaled 323 adaptive weights, STAP 224 adaptive weights, and FBA had 350 adaptive weights in the first stage and 224 adaptive weights in the second stage. Despite requiring fewer computations and less sample support, the results, nonetheless, favor BASTAP over FBA.

Filtered Outputs

Conventional (nonadaptive) filter outputs for sidelobe and mainbeam jamming are shown in Fig. 5.6. In neither case was the 50 dB target revealed by the nonadaptive processor. Figure 5.7 demonstrates the outputs of the adaptive processors for sidelobe jamming. All three adaptive processors unmasked the 50 dB target at range bin 500 with BASTAP achieving the best cancellation performance. With a residual output interference to noise ratio (OINR) of 11.7 dB, BASTAP improved over STAP by 5.8 dB and over FBA by 6.3 dB. In a more difficult scenario of mainbeam jamming where the target was obscured by the direct path jammer (i.e., at 32°), Fig. 5.8 shows that BASTAP at 24.2 dB still offered an improvement of 7.1 dB over STAP and 4.7 dB over FBA.

For both sidelobe and mainbeam jamming, the added reference beam taps in BASTAP clearly work to its advantage over STAP and FBA. The fact that the TSI is stationary makes a single Doppler reference beam sufficient, thus allowing more taps to be utilized than in FBA. Additionally, as discussed earlier in Sec. 5.1.1, FBA suffers from the modulation effect and, as a result, suffers slight degradation over

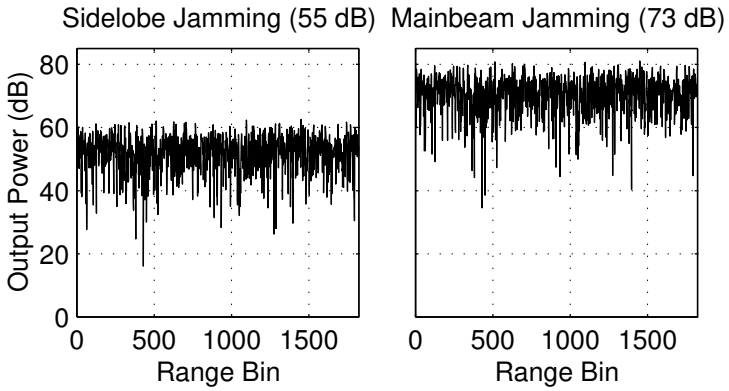

Figure 5.6: Nonadaptive filtered outputs for sidelobe and mainbeam jamming with stationary TSI and synthetic MSC.

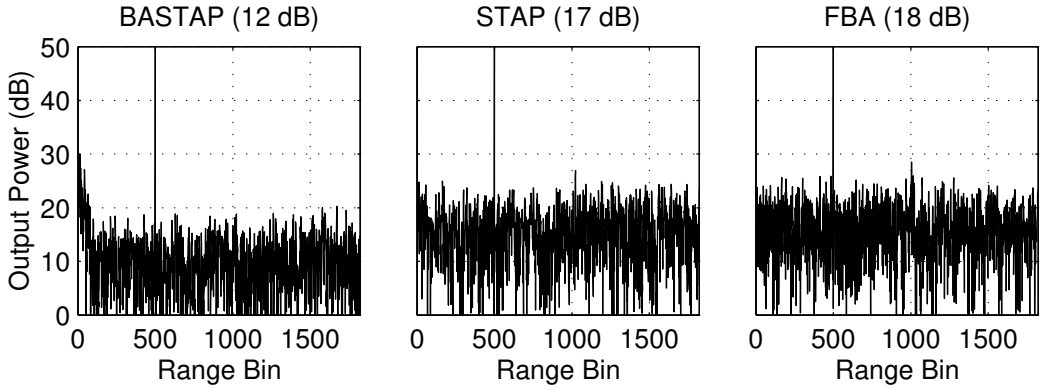

Figure 5.7: Adaptive filtered outputs for sidelobe jamming with stationary TSI and synthetic MSC.

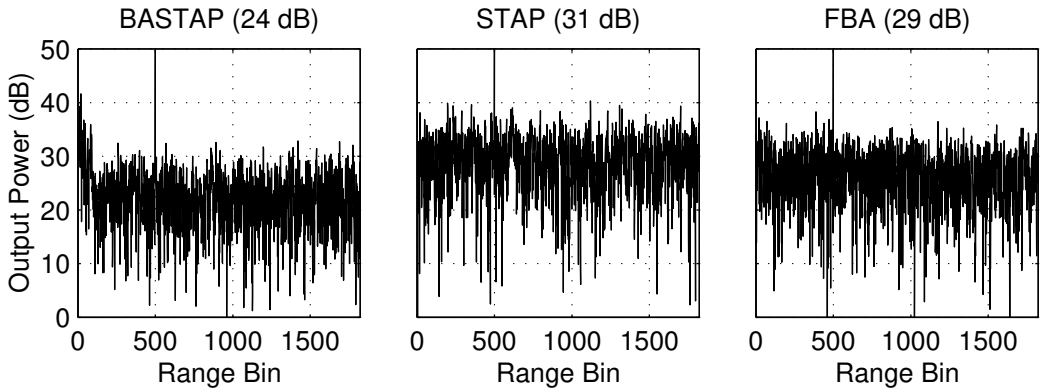

Figure 5.8: Adaptive filtered outputs for mainbeam jamming with stationary TSI and synthetic MSC.

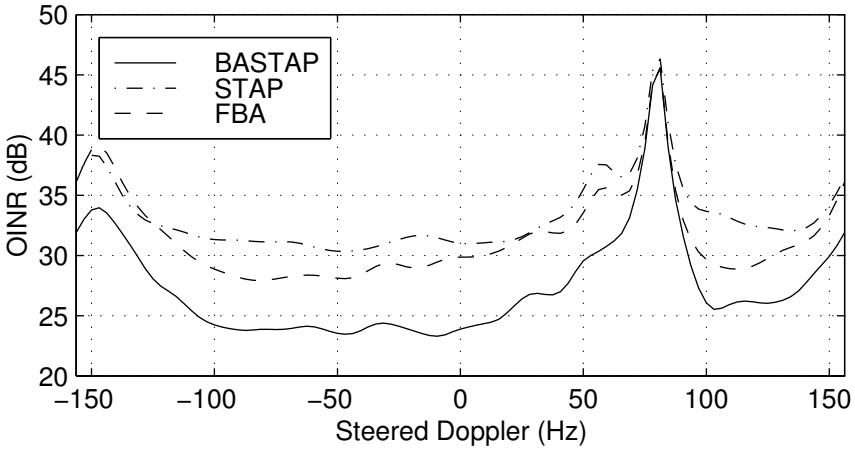

Figure 5.9: Mitigation performance versus Doppler for stationary mainbeam jamming scenario.

STAP for sidelobe jamming.

Variation Across Doppler

In the previous examples mitigation performance was only considered for a single azimuth and Doppler. In the following analysis a more comprehensive evaluation is conducted for the mainbeam jamming scenario by varying Doppler frequency and observing mitigation performance. By doing so we intend to demonstrate consistent behavior for the three processors for more than just a single Doppler frequency, as was done previously. The procedure is to fix the angle at 32° (i.e., mainbeam jamming) and obtain OINR measurements as the processor look Doppler is varied incrementally from −156.25 Hz to 156.25 Hz. Naturally, as the look Doppler is varied, the auxiliary beam in BASTAP has to be updated accordingly, otherwise BASTAP will result in performance degradation due to a mismatch in Doppler compensation.

Figure 5.9 shows OINR vs. Doppler for the three processors under consideration: BASTAP, STAP and FBA. For all three processors, the worst performance occurs at the Doppler range corresponding to the mainbeam clutter (i.e., MSC entering the processor's mainbeam at 32°). The MSC power spectrum in Fig. 5.1 indicates that

the Doppler range occupies approximately 70 Hz to 90 Hz. While TSI and mainbeam jamming mitigation still take place in the mainbeam clutter region, MSC mitigation clearly does not! This is not due to any particular shortcoming of the processors under evaluation, but, rather, because the MSC is uncorrelated with energy elsewhere in the three-dimensional spectrum and, thus, cannot be mitigated, even with full rank three-dimensional processing.

Aside from reduced mitigation in the mainbeam clutter region, reduced mitigation at the edges of the Doppler spectrum occurs as well. This is true for all three processors and, therefore, is attributed to the nature of the interference, rather than to the processing itself. The consistency in the relative performance of the three processors thus serves to further validate the initial observations made based on the sample filter outputs. This is of particular importance, since further analyses evaluate OINR performance as a function of other parameters by fixing the look angle and Doppler, and we wish to make our other comparisons conclusive.

Beam and Tap Analysis

Figure 5.10 illustrates OINR performance for BASTAP having between 1 and 300 taps. For sidelobe jamming (solid line) roughly 14 dB of improvement was attained in going from 1 tap (i.e., STAP) to 300 taps. Most of the curve is fairly flat with sharp drop offs occurring at roughly 50 and 140 taps. Thus, a majority of the cancellation can be achieved by incorporating only a select number of taps. A priori determination of these taps could result in computational savings and a reduction in the required sample support. In contrast to sidelobe jamming, however, mainbeam jamming (dashed line) does not have the sharp drop offs necessary to consider weight thinning strategies. Furthermore, in going from 1 to 300 taps, only 10 dB of improvement was attained.

To this point only a single auxiliary beam has been considered. The tradeoff between the number of auxiliary beams and the number of taps is briefly examined in

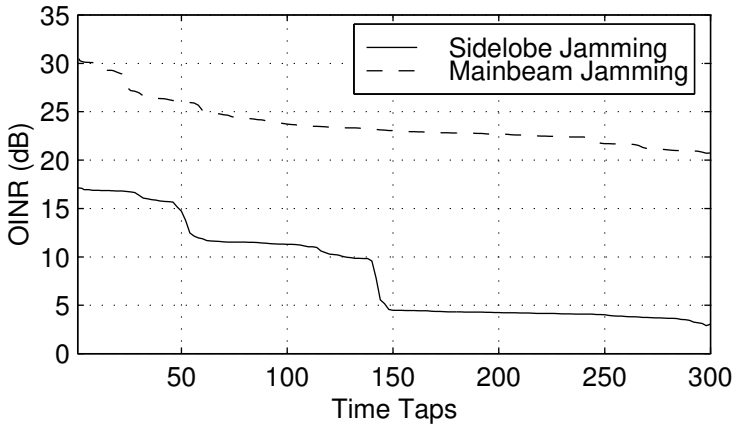

Figure 5.10: OINR vs. taps in BASTAP for sidelobe and mainbeam jamming scenarios.

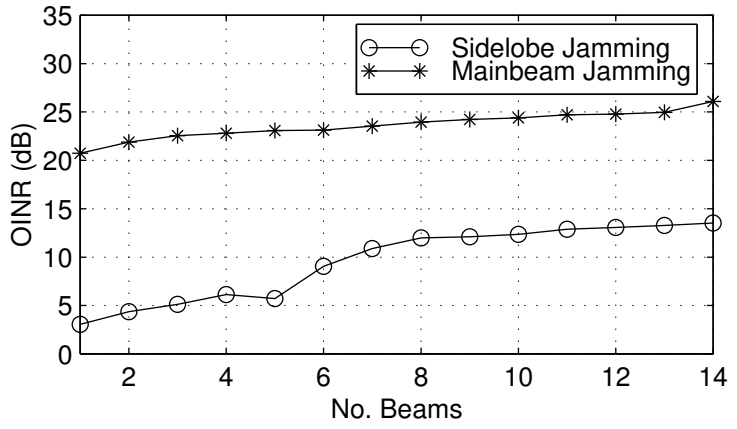

Figure 5.11: OINR performance for number of beams vs. number of taps with fixed adaptive DOF in BASTAP for sidelobe and mainbeam jamming scenarios.

the following. In Fig. 5.11 the number of beams is varied from 1 to 14. The strategy for beam placement is merely to select the first beam location and follow with successive orthogonal beam placement interchangably on both sides. It should be noted that this beam placement strategy does not consider the "best" set of spatial beams. The adaptive degrees of freedom (DOF) are kept at approximately 525. This means that as more auxiliary beams are added, fewer taps can be alloted to these beams. As the results demonstrate, exchanging taps for spatial beams hurts performance for both sidelobe and mainbeam jamming.

In contrast, a similar analysis in [31] finds favor in exchanging spatial degrees of freedom for temporal degrees of freedom for the two-dimensional SFT problem. For equal DOF, the multiple-beam "beamspace TSI canceler" is shown to offer roughly equivalent mitgation performance with the "single reference beam canceler" when there is a direct path jammer and improved mitigation performance when there is no direct path jammer. A shorter blind interval further motivates the multiple beam architecture. However, we see that in the three-dimensional interference environment in which BASTAP operates, temporal DOF are favored over spatial DOF. It should also be taken into consideration that the single reference beam canceler posseses only one adaptive spatial DOF in the first tap, whereas BASTAP possesses full spatial adaptivity in the first tap. If the single reference beam canceler was to be modified so that it possesses full spatial adaptivity in the first tap (i.e., a one-pulse version of BASTAP) then the outcome might be different.

Beam Response

In the examples for both sidelobe and mainbeam jamming BASTAP improved interference mitigation over STAP and FBA. As shown next, the improved interference mitigation does not come at the expense of the processor response (i.e., its beampattern). The beampattern responses of BASTAP and FBA are three dimensional; however, two-dimensional cross-sectional slices are sufficient to indicate the behav-

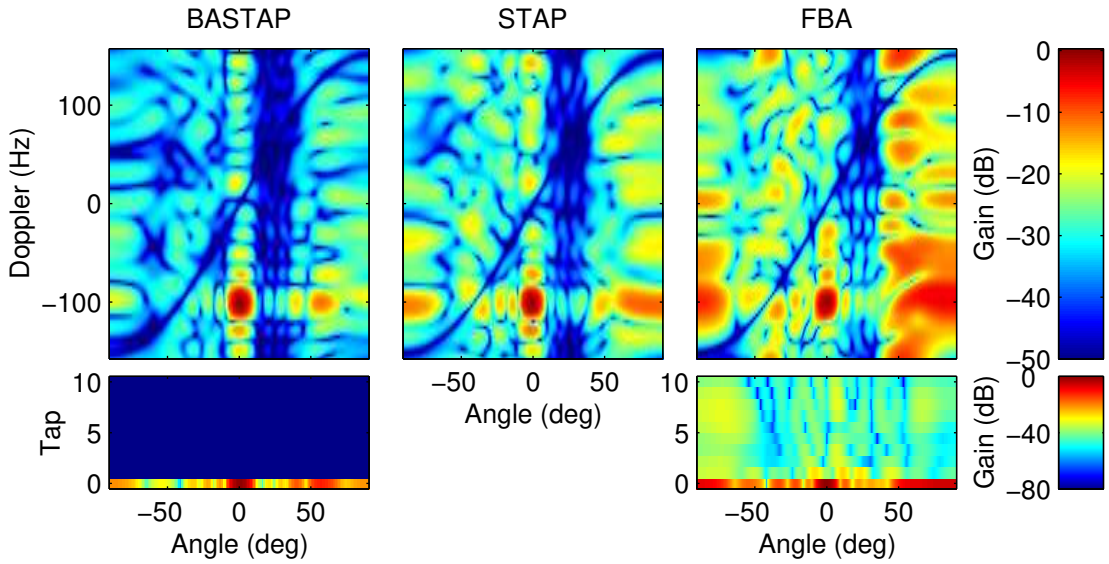

Figure 5.12: Select cross-sections of the 3D response for the stationary sidelobe jamming problem.

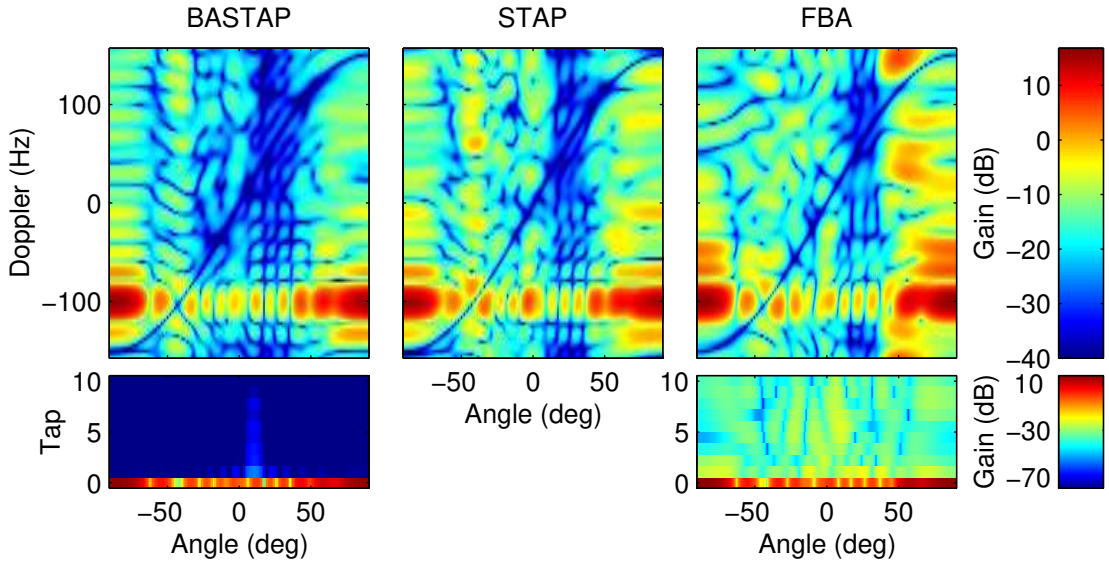

Figure 5.13: Select cross-sections of the 3D response for the stationary mainbeam jamming problem.

ioral response of the processors. The top of Fig. 5.12 shows the space-Doppler cross-section at the zeroth lag for BASTAP and FBA. The response of BASTAP shows improvement over that of FBA and STAP as discerned by the reduced gain in regions away from the target's look direction (0°) and Doppler frequency (-100 Hz). Both responses have a visible monostatic clutter null cutting across diagonally.[2] The mainbeam (at 0° and -100 Hz) can be discerned easily, although more clearly in the BASTAP response. At the bottom of Fig. 5.12 is the SFT response of BASTAP and FBA shown for the first ten time taps at -100 Hz (i.e., target Doppler). The well-behaved response of BASTAP is characterized by the absence of target spreading and overall low gain in successive taps. The fact that FBA introduces excess gain throughout the SFT region and, yet, does not achieve the level of cancellation offered by BASTAP suggests that BASTAP is a more natural and efficient choice for the combined TSI, MSC, and mainbeam jamming problem. Note that lower gain in regions away from the look direction make the processor less susceptible to false alarms, hence improving robustness.

The mainbeam jamming scenario is illustrated in Fig. 5.13. The look direction and corresponding mainbeam is at 32° and -100 Hz. The spatial response at -100 Hz suffers from the same high sidelobes that were present in the mainbeam jamming examples of the previous chapter. However, it was noted in the previous chapter that if one considers the two-way response the high sidelobes are not truly a threat, and, in fact, for the examples of Fig. 4.27 and Fig. 4.28 the two-way sidelobes were shown to peak at about -20 dB. Once again, BASTAP demonstrates the least amount of high gain artifacts throughout space and Doppler. Similarly the SFT response of BASTAP is far improved over that of FBA. Only slightly increased gain appears where the auxiliary channel is positioned, that is at 10° and -100 Hz.

In conclusion, for the stationary jamming scenario BASTAP outperforms STAP and FBA, both in terms of interference suppression and by a qualitative assessment of

[2]Note that the clutter null appears warped when plotted against azimuth angle.

the space-Doppler beampattern responses. BASTAP also outperforms FBA in terms of the SFT response, thus assuring far less target spreading.

5.5.3 Results for Nonstationary Jamming and TSI

In a nonstationary interference environment the jammer multipath components that make up the composite TSI signal experience Doppler shifts from radar platform and jammer motion. The Doppler spread in the TSI necessitates Doppler compensation in BASTAP, and, therefore, a single reference beam at one select Doppler is no longer sufficient. In analyzing the three processors on nonstationary data, FBA was configured with 40 taps, while extended-BASTAP was configured as shown in Fig. 5.5b with sixteen 25-tap reference beams. The added Doppler beams come at the expense of reduced temporal taps.

Adaptive weights for each of the three processors are computed for mountaintop dataset `hot6067v1` injected with 40 dB of synthetic MSC. The look direction considered was at 30° and −100 Hz for the sidelobe jamming scenario and at −2° and −100 Hz for the mainbeam jamming scenario. For sidelobe jamming the auxiliary beams of the BASTAP processor were positioned pointing at the jammer at −2° at sixteen equally spaced Dopplers spanning the 312.5 Hz Doppler spectrum (i.e., $-156.25, -136.71, -117.19, ..., 136.71$) For mainbeam jamming the auxiliary beams were positioned pointing at a region heavy in TSI, namely at −15°, with the same Doppler distribution.

Filtered Outputs

Conventional filter outputs for sidelobe and mainbeam jamming are shown in Fig. 5.14. Once again, neither of the conventional processors were able to unmask the 50 dB target. The filtered outputs for the three adaptive processors for sidelobe jamming are shown in Fig. 5.15. The residual OINR is 21 dB for BASTAP, 27 dB for STAP, and 21 dB for FBA. In the nonstationary environment the need for additional

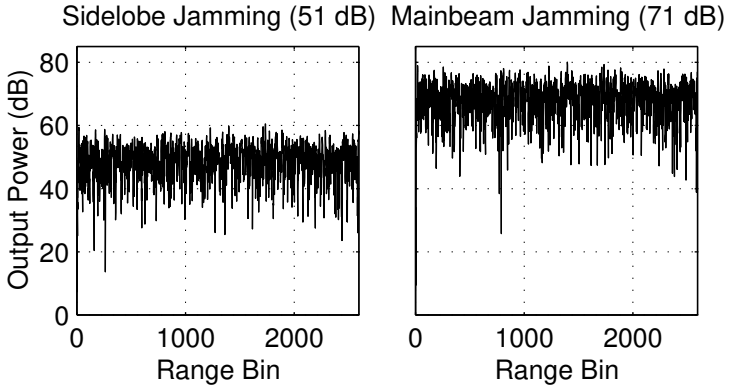

Figure 5.14: Nonadaptive filtered outputs for sidelobe and mainbeam jamming with nonstationary TSI and synthetic MSC.

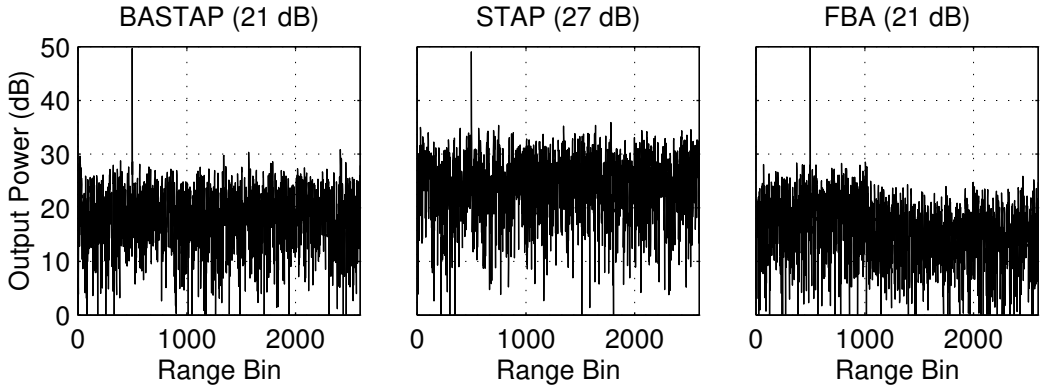

Figure 5.15: Filtered outputs for sidelobe jamming with non-stationary TSI combined with synthetic MSC.

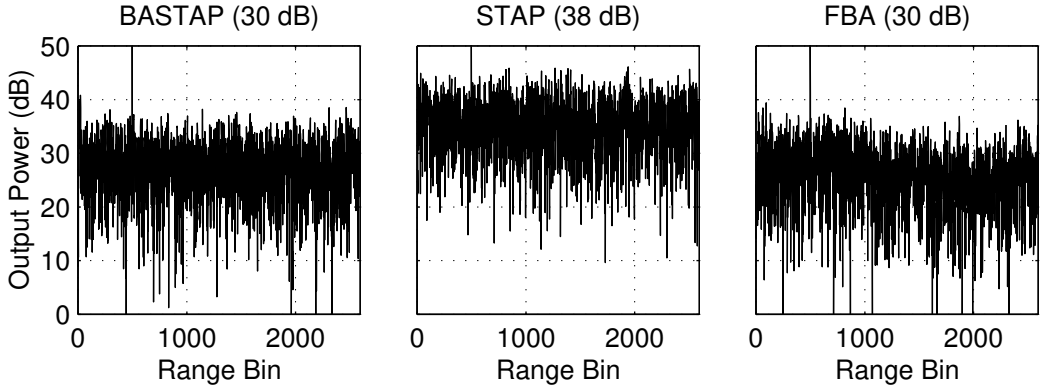

Figure 5.16: Filtered outputs for the mainbeam jamming scenario with non-stationary TSI combined with synthetic MSC.

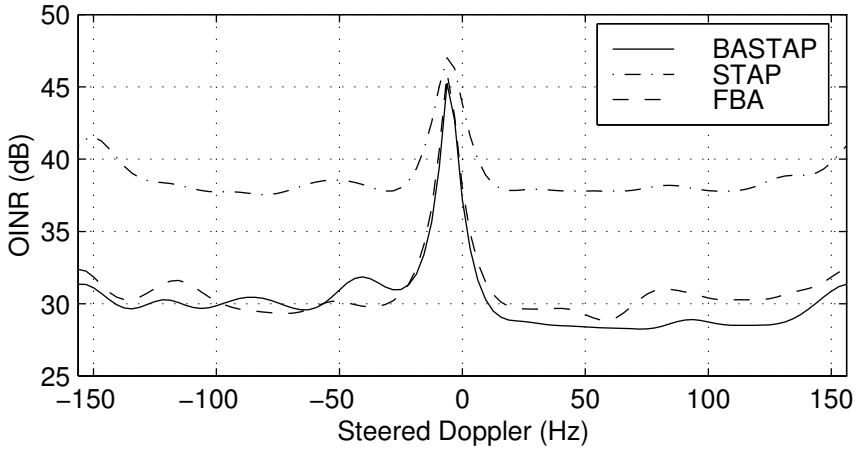

Figure 5.17: Mitigation performance versus Doppler for nonstationary mainbeam jamming scenario.

reference beams in BASTAP and the resulting reduction in taps clearly worked to its disadvantage over FBA. However, as expected BASTAP still outperforms STAP.

Sample filter outputs for the mainbeam jamming scenario are shown in Fig. 5.16. The residual OINR is 30 dB for BASTAP, 38 dB for STAP, and 30 dB for FBA. As with sidelobe jamming, in the mainbeam jamming scenario BASTAP and FBA are approximately equivalent in terms of interference mitigation. However, in general, all suffered performance degradation in terms of interference rejection caused by the increasingly complicated correlation structure of the interference. When comparing the nonadaptive outputs for the stationary and nonstationary datasets to those of the adaptive outputs, we observe that all the adaptive processors accomplish significantly less interference rejection under nonstationary conditions.

Variation Across Doppler

Similar to the stationary environment, the variation of target Doppler for mainbeam jamming in the nonstationary environment is considered here. For a fixed look direction of -2° (i.e., mainbeam jamming) the target Doppler is varied from -156.25 to 156.25 Hz, and OINR measurements are taken incrementally, as shown in Fig. 5.17.

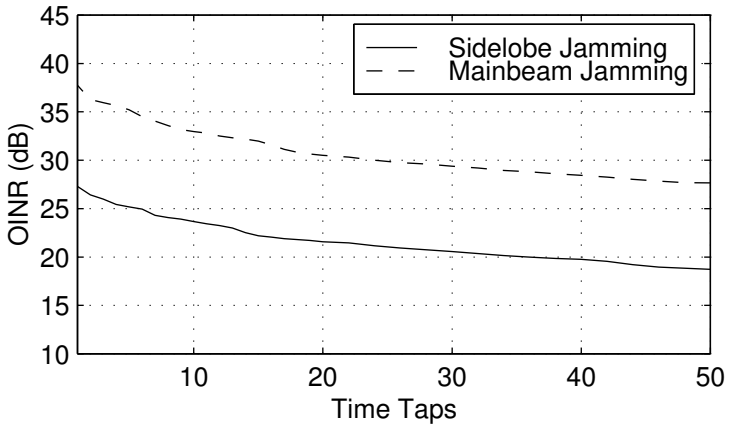

Figure 5.18: OINR vs. taps in BASTAP for sidelobe and mainbeam jamming.

For BASTAP, sixteen auxiliary beams distributed evenly across Doppler were pointed at $-15°$. Since the auxiliary beams cover the entire Doppler spectrum, there is no need to continuously update beams with changing Doppler as was necessary for the stationary environment.

This time, the mainbeam clutter appears at $-2°$ or, equivalently, in the approximate range between -20 and 0 Hz, once again obstructing mitigation in that region. The effect of reduced mitigation at the Doppler edges is far less pronounced in the nonstationary environment than it was in the stationary environment (Fig. 5.9). However, in general the OINR performance throughout the Doppler region has been degraded because of the more difficult nature of the nonstationary interference. Overall OINR performance for BASTAP, STAP, and FBA is fairly consistent across Doppler (even more so than for the stationary environment). Therefore, it is safe to continue to rely on results from selected sample Doppler and angle, allowing other parameters to be varied as OINR performance is evaluated for those parameters.

Tap Analysis

Just as with stationary data, adding taps is expected to enhance performance. Figure 5.18 illustrates OINR performance for BASTAP having between 1 and 50 taps. In

the analysis we were not able to extend the filter in fast-time to the extent that was done for BASTAP in stationary TSI. This is because each tap in the nonstationary configuration is applied to 16 reference beams which cover the Doppler spectrum. As a result, the number of degrees of freedom associated with each fast-time tap is 16 times as many. For the nonmainbeam jamming scenario (solid line) roughly 9 dB improvement is attained in going from 1 tap (STAP) to 50 taps. The increase in performance is fairly uniform throughout the region of evaluation, so there is no point in searching for the most effective taps for weight thinning purposes. In the mainbeam jamming scenario (dashed line), a 10 dB improvement is attained in going from 1 to 50 taps.

Beam Response

In the examples of both sidelobe and mainbeam jamming BASTAP performed equivalent to FBA in terms of interference mitigation. As will be shown next, the space-Doppler responses of BASTAP are also roughly equivalent to those of FBA but still maintaining an edge over STAP. At the top of Fig. 5.19 the space-Doppler beampattern response for the first tap of each of the three processors in the sidelobe jamming example is shown. The look direction is at 30° and -100 Hz, as indicated by the mainlobe appearing at that location. Qualitatively, the space-Doppler beampattern response of BASTAP appears about the same as that of FBA. Both show a slight improvement over STAP. The nonstationarity of the problem introduced higher sidelobes and gain artifacts into the respective responses, as the possibility of efficient utilization of the TSI energy from the different regions of the space-Doppler spectrum is diminished. The clutter null appears equally well in all three responses. The improvement of BASTAP over FBA is still apparent from its SFT response, shown for the first 10 taps at the bottom of Fig. 5.19. Once again, excess gain at successive taps for BASTAP is practically unnoticable even for auxiliary beams at $-2°$.

The mainbeam jamming scenario is illustrated in Fig. 5.20. The look direction

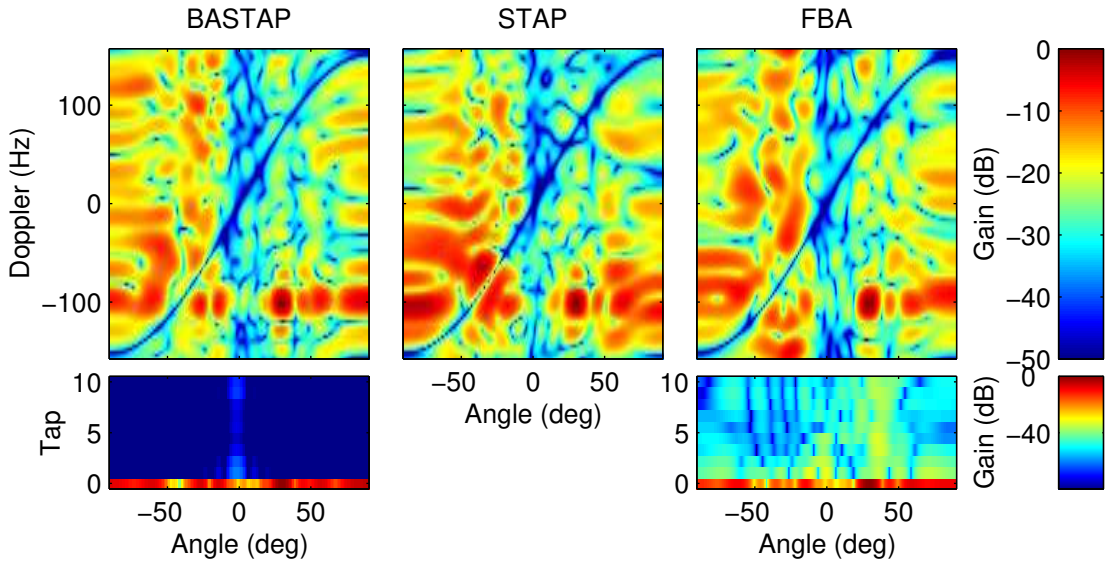

Figure 5.19: Select cross-sections of the 3D response for the nonstationary sidelobe jamming problem.

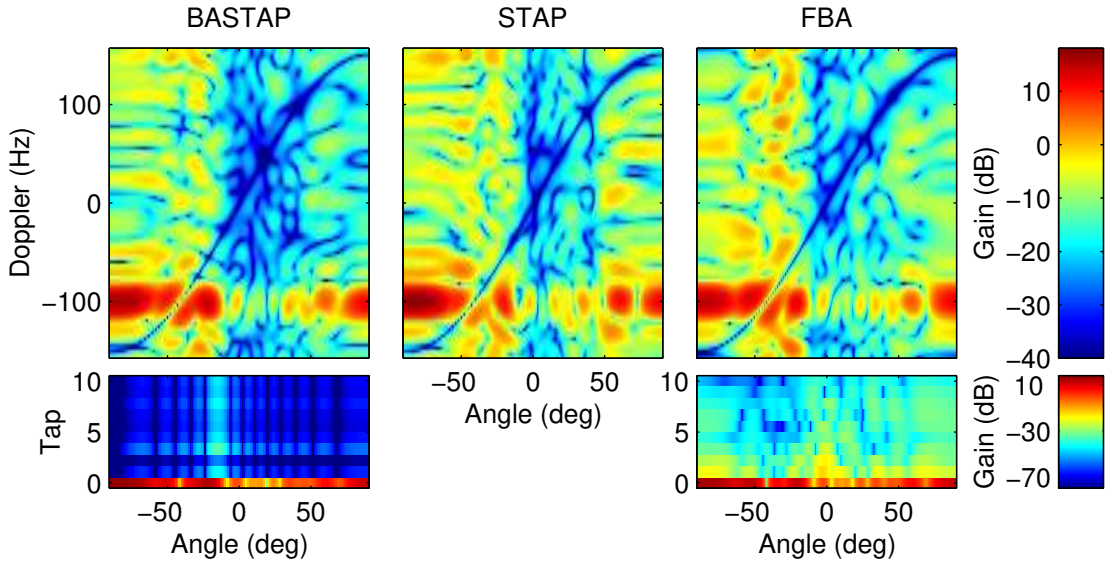

Figure 5.20: Select cross-sections of the 3D response for the nonstationary mainbeam jamming problem.

Table 5.4: Processor configurations for the variable clutter experiment.

			BASTAP		FBA
Jamming	ϕ_0	f_0	(ϕ_{aux}, f_{aux})	Taps	Taps
`stat`	0	-100	$(32, -100)$	100	25
`stat/mbj`	32	-100	$(10, -100)$	100	25
`nstat`	30	-100	$(-15, \texttt{all})$	25	40
`nstat/mbj`	-2	-100	$(-2, \texttt{all})$	25	40

and corresponding mainbeam is at $-2°$ and -100 Hz. In terms of the space-Doppler response there is no apparent improvement or degradation of BASTAP over FBA or STAP. In terms of the SFT response BASTAP does demonstrate improvement over FBA. This time the majority of the gain at successive taps of BASTAP appears at $-15°$, the location of the auxiliary channel.

Despite its clear advantage over FBA in the stationary environment, BASTAP results to this point proved far less dramatic in the nonstationary environment, as the comparisons with STAP and FBA demonstrated. In the next section important insight into BASTAP and FBA is provided in terms of varying MSC power.

5.6 Other Results

5.6.1 Varying Clutter Power

So far, evaluation and comparison of the three processors has been restricted to experimental TSI datasets combined with synthetic MSC at 40 dB. In reality, the degree of clutter power relative to the TSI and jamming varies significantly with the surrounding conditions. Clutter power also varies substantially with distance from the radar [66, 59]. Ignoring the latter effect, we evaluate mitigation performance for the `mmit004v1` dataset combined with synthetic MSC ranging in power from 0 to 60 dB. The three processors are configured according to the parameters in Table 5.4. For the nonstationary experiments, "all" signifies sixteen Doppler compensation beams dis-

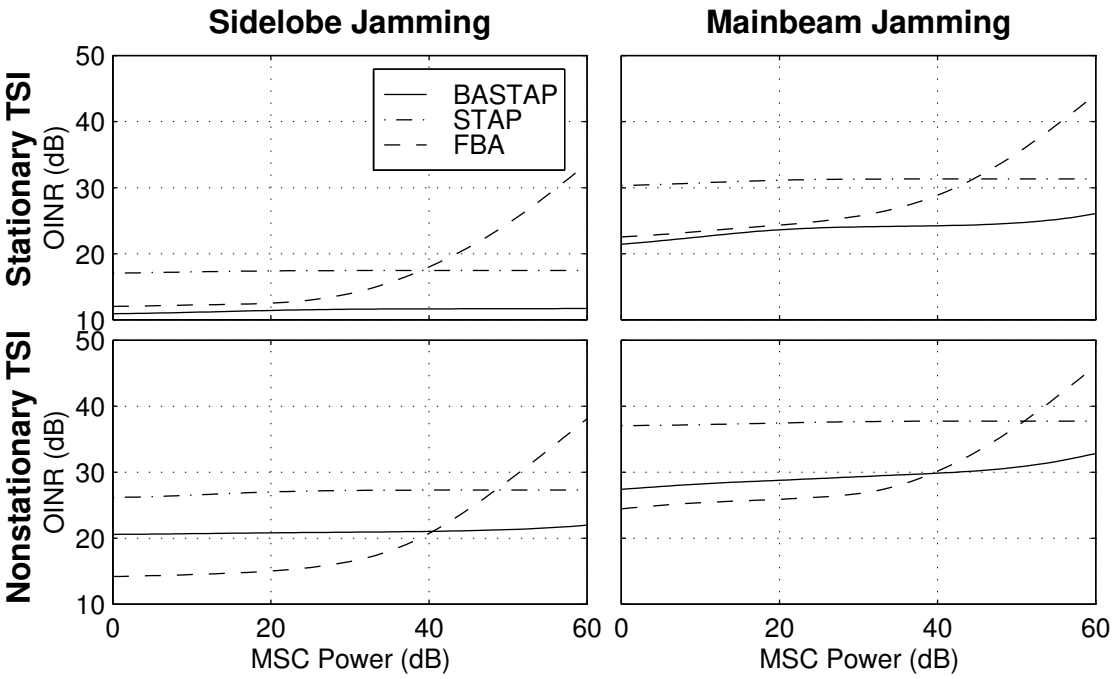

Figure 5.21: OINR vs. clutter power for BASTAP, STAP, and FBA.

tributed evenly across the 312.5 Hz Doppler spectrum. Figure 5.21 illustrates results for the sidelobe and mainbeam jamming scenarios under stationary and nonstationary conditions. Under stationary conditions, BASTAP outperforms both STAP and FBA for the given MSC power range. The more interesting results occur for nonstationary TSI and jamming. The sidelobe and mainbeam jamming scenarios are considered together since their outcomes are similar. For less than approximately 40 dB of synthetic MSC, FBA outperforms BASTAP and STAP, whereas beyond 40 dB BASTAP outperforms FBA. For sufficiently high MSC levels in nonstationary TSI, FBA loses out to STAP as well.

From the figure it can be observed that STAP and BASTAP are quite insensitive to the level of MSC. The reason being that STAP is extremely adept at contending with MSC and, in particular, with synthetic MSC. STAP's performance is, thus, dictated primarily by the TSI and mainbeam jamming present in the data. Similarly, BASTAP, which possesses as a principal component a fully adaptive STAP processor, tends to handle the MSC better than the TSI and mainbeam jamming, which are only handled in a reduced rank fashion. In contrast, FBA is extremely sensitive to levels of MSC. The high sensitivity is due to the modulation effect described earlier in Sec. 5.1.1 that distorts the MSC. The distorted clutter in turn imposes an ever increasing burden on the second stage of the FBA as its power is increased.

5.6.2 Varying Auxiliary Beam Position

For all of the previous analyses, the angular position of the auxiliary beam was selected through a general knowledge of the interference environment without, however, much consideration for optimality. In the following analysis the position of the auxiliary beam(s) for BASTAP is varied across angle while maintaining a fixed look direction. Figure 5.22 illustrates the results for stationary and nonstationary environments and sidelobe and mainbeam jamming scenarios. Note that for the nonstationary simulations, the look direction of all sixteen reference beams was varied together. A red

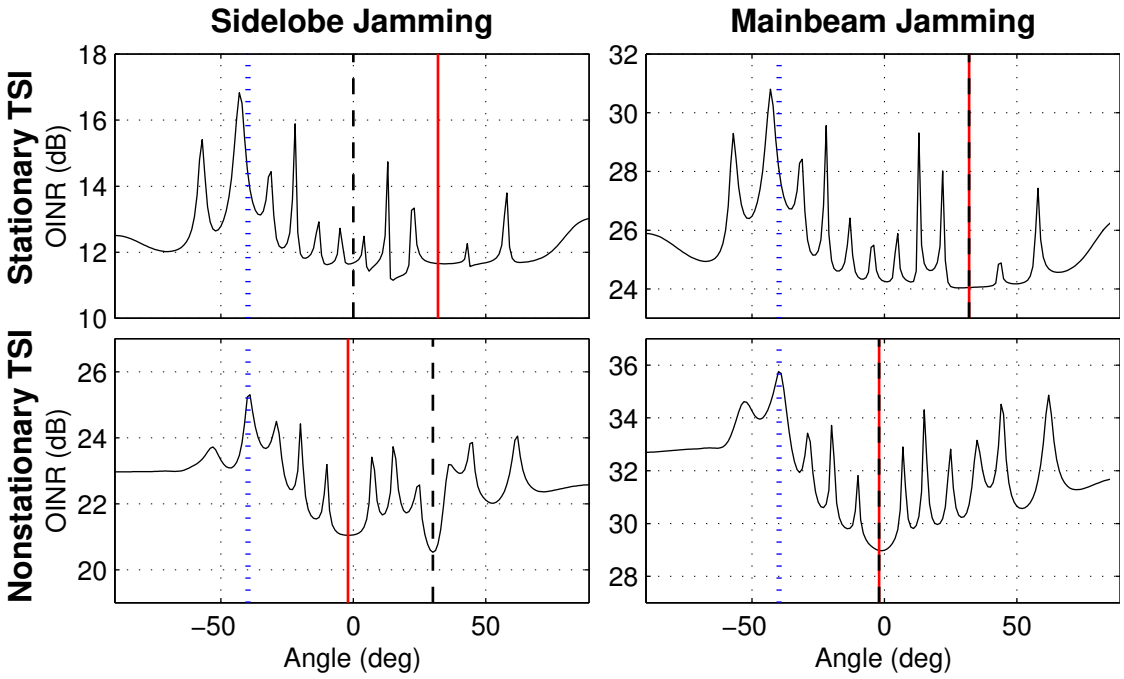

Figure 5.22: OINR vs. auxiliary beam angle in BASTAP. A red vertical line indicates the jammer position, a blue dotted line the mainbeam clutter position, and a dashed line indicates the look direction.

vertical line indicates the jammer position, a blue dotted line the mainbeam clutter position (i.e., clutter sharing the same Doppler as the target), and a dashed line indicates the look direction.

The results reveal some surprising observations. In particular, that OINR performance is not adversely affected by the angular position of the reference beam(s). Prior to the simulation it was assumed that for sidelobe jamming it was best to orient the reference beam in the direction of the jammer, whereas for mainbeam jamming it was best to orient it towards a region heavy in TSI. The results, however, indicate the converse. Optimal beam placement for the sidelobe jamming scenario is not at the position of the jammer and for the mainbeam jamming scenario is not at adjacent TSI, but rather at the jammer itself. From the figure plots it seems that the safest approach is to point the reference beam(s) either at the look direction or jammer, and, indeed, the given approach yields near optimal to optimal performance.

Another observation is that pointing the reference beam at the mainbeam clutter (blue dotted line) does not significantly degrade performance for BASTAP. Consider BASTAP with only a single reference beam (under stationary conditions). Since the purpose of the reference beam is to collect delayed TSI and/or mainbeam jamming energy to use in predicting and, thus, cancelling TSI and/or direct path jamming in the look direction, we might assume that MSC in the reference beam taps will not allow the necessary prediction mechanism to operate properly. However, this assumption is false, since the MSC, which is uncorrelated in fast-time, tends to integrate incoherently in the processor output and, thus, average out. Whereas the TSI and jamming, which are correlated in fast-time, tend to integrate constructively because of the choice of filter weights.

Finally, it can be observed that the plots are characterized by peaks and valleys. If plotted on a spatial frequency axis, the peaks would appear equidistant from each other with an approximate spacing of 1/N; all with the exception of the two peaks surrounding the jammer and some of the outlying peaks. The spacing between

peaks surrounding the jammer are equidistant from the jammer at a spacing of approximately 1/N. If a conventional beampattern (pointed at the jammer) would be superimposed on any of the four plots, the nulls of the conventional beampatterns would approximately coincide with the peaks in the OINR plots (less the outlying peaks). Thus, the resulting pattern of peaks and valleys indicates that the jammer direct path and multipath in its proximity play an essential role in mitigation. Whenever the reference beam places a null in the direction of the jammer, performance plummets down. Considering the filter outputs in Fig. 5.16, BASTAP and FBA perform approximately the same. Had we considered placing the auxiliary beam at the jammer location rather than at 15°, from Fig. 5.22 we see that our processor would have fared approximately 1 dB better.

5.6.3 Results for Other Datasets

So far only two TSI datasets have been considered; stationary dataset `mmit004v1` and nonstationary dataset `hot6067v1`. Tables 5.5 and 5.6 summarize results from these and other datasets combined with 40 dB of synthetic MSC. In each table, the individual datasets are evaluated at a look angle, ϕ_0, and Doppler frequency, f_0. For BASTAP the reference beam parameters are listed as an angle-Doppler pair (ϕ_{aux}, f_{aux}). For nonstationary datasets `hot6067v1`, `rio042v1` and `rio043v1`, "all" signifies sixteen Doppler compensation beams distributed evenly across the 312.5 Hz Doppler spectrum. For both sidelobe and mainbeam jamming, BASTAP consistently outperforms STAP and FBA under stationary TSI and jamming conditions, as represented by the `mmit` datasets. Under nonstationary conditions, BASTAP outperforms FBA for datasets `rio042v1` and `rio043v1`, and also `hot6067v1` with mainbeam jamming.

Table 5.5: Sidelobe jamming performance results for other MT datasets.
[a]Contains TSI without a direct path jammer.
[b]Contains nonstationary TSI.

			BASTAP		STAP	FBA
Name	ϕ_0	f_0	(ϕ_{aux}, f_{aux})	OINR	OINR	OINR
mmit004v1	−30.0	0.0	(32.0,0)	17.2	18.6	18.8
mmit013v1	0.0	100.0	(66.2,100)	13.5	14.7	15.8
mmit043v1	−30.0	0.0	(32.0,0)	6.0	7.3	8.7
mmit044v1	−30.0	0.0	(32.0,0)	6.4	7.7	8.0
mmit045v1	−30.0	0.0	(32.0,0)	5.1	6.4	7.3
mmit048v1	−30.0	0.0	(32.0,0)	6.4	7.6	8.0
mmit109v1[a]	−30.0	0.0	(32.0,0)	21.8	23.1	22.9
mmit112v1[a]	−30.0	0.0	(32.0,0)	21.5	22.7	23.3
hot6067v1[b]	40.0	0.0	(−1.6, all)	24.4	27.5	22.4
rio042v1[b]	−30.0	0.0	(8.7, all)	8.6	13.1	10.7
rio043v1[b]	−40.0	0.0	(10.7, all)	4.5	8.6	7.4

Table 5.6: Mainbeam jamming performance results for other MT datasets.
[a]Contains TSI without a direct path jammer.
[b]Contains nonstationary TSI.

			BASTAP		STAP	FBA
Name	ϕ_0	f_0	(ϕ_{aux}, f_{aux})	OINR	OINR	OINR
mmit004v1	32.0	0.0	(32.0,0)	23.4	31.0	29.9
mmit013v1	66.2	0.0	(66.2,0)	24.8	34.4	27.9
mmit043v1	32.0	0.0	(32.0,0)	21.5	26.2	24.8
mmit044v1	32.0	0.0	(32.0,0)	21.3	25.9	24.0
mmit045v1	32.0	0.0	(32.0,0)	18.2	24.3	21.8
mmit048v1	32.0	0.0	(32.0,0)	21.8	26.4	24.3
mmit109v1[a]	32.0	0.0	(32.0,0)	24.7	26.4	27.4
mmit112v1[a]	32.0	0.0	(32.0,0)	24.0	26.1	27.5
hot6067v1[b]	−1.6	100.0	(−1.6, all)	28.4	38.0	30.7
rio042v1[b]	8.7	100.0	(8.7, all)	32.8	37.4	37.7
rio043v1[b]	10.7	100.0	(10.7, all)	31.6	36.7	37.1

5.7 Conclusions

The main innovation introduced in this chapter is a reduced rank technique for the joint mitigation of jamming, TSI, and monostatic clutter. A STAP filter accomplishes the majority of interference rejection, with further TSI suppression accomplished via an additional tapped reference beam. Simultaneous optimization of the MSC filter weights and reference beam weights yields the desired BASTAP processor. A single reference beam configuration proves effective for stationary TSI, whereas a multiple reference beam configuration proves effective for nonstationary TSI.

It was demonstrated through a number of examples that the processor performs quite well under conditions of stationary TSI, offering improved cancellation and beampattern response performance over existing techniques. In the case of nonstationary TSI, extended-BASTAP still maintained superiority over STAP but evened off with the factored beamspace approach. Although the results on nonstationary data initially proved less promising for BASTAP, additional analyses that were conducted indicated other possible advantages for BASTAP. In particular, variation of clutter power demonstrated that STAP and BASTAP maintain consistent performance with varying clutter levels, whereas the factored beamspace approach degraded dramatically over both STAP and BASTAP as the clutter level increased beyond 40 dB. Additionally, without a beam selection strategy for BASTAP the results for BASTAP were less than optimal. Variation of the auxiliary beam position showed that with a proper beam placement strategy BASTAP performance can be enhanced beyond what earlier results had demonstrated.

CHAPTER 6

Monopulse Processing Using BASTAP

As in Chapter 4 we wish to extend the monopulse concept to processing in three dimensions: space, fast-time, and slow-time. This extension will allow us to perform adaptive monopulse processing in the combined presence of TSI, MSC, and mainbeam jamming. As seen earlier, mainbeam jamming introduces distortions into the mainbeam of the sum processor and, likewise, into the split mainbeam in the difference processor, thus, degrading the MRC. We would like to develop a three-dimensional monopulse processor that has undistorted target response characteristics in the mainbeam and, yet, provides adequate suppression of TSI, MSC, and mainbeam jamming with minimal target spreading. Furthermore, we would like the processor to be robust to Doppler mismatch. The processor under consideration is Beam-Augmented STAP (BASTAP) with sum and difference constraints chosen to achieve these criteria. In this chapter we present a development of the BASTAP monopulse processor followed by an evaluation of various performance aspects of the new processor through simulation on experimental TSI and synthetic MSC data.

6.1 Extending BASTAP to Monopulse

Following a similar approach to that of Chapter 4 we wish to reinterpret some of the spatial quantities defined in Sec. 3.2 for three-dimensional processing, in particular for use with the BASTAP processor. Sum and difference outputs are given in terms

of the respective sum and difference BASTAP processors,

$$z_\Sigma(t) = \mathbf{W}_\Sigma^H \mathbf{Y}(t) \qquad z_\Delta(t) = \mathbf{W}_\Delta^H \mathbf{Y}(t), \tag{6.1}$$

where $\mathbf{Y}(t)$ was defined in (5.2). As with SFT monopulse, the definition of the error voltage remains the same: the real part of the ratio of difference-to-sum outputs

$$\epsilon_v(t) = \Re\left\{\frac{z_\Delta(t)}{z_\Sigma(t)}\right\}. \tag{6.2}$$

The error voltage here conveys purely directional information that must be converted to angular form via an MRC. The MRC was defined in Chapter 3 as the ratio of difference to sum beampatterns and represented the ideal error voltage response to targets arriving from a particular angular region about boresight. BASTAP sum and difference processors have beampattern responses that are functions of angle, fast-time, and Doppler

$$\mathcal{W}(\phi, f, \tau) = \begin{cases} \mathbf{W}_{main}^H \mathbf{v}(\phi, f) & \tau = 0, \\ \mathbf{W}_{aux}(\tau)^H \left(\mathbf{F}^H \mathbf{v}(\phi, f)\right) & 1 \le \tau \le T-1 \end{cases}, \tag{6.3}$$

where $\mathbf{W}_{main}$ is a vector comprised of the first MN weights of $\mathbf{W}$ (i.e., the STAP component of BASTAP or main channel weights), and $\mathbf{W}_{aux}(\tau)$ is a vector (or scalar for single beam BASTAP) comprised of the auxiliary weights of $\mathbf{W}$ from the τ^{th} lag. In BASTAP the target response is constrained to have a specific gain at a given angle and Doppler at the first tap. It is, thus, anticipated that the response has a peak at the first tap, where the gain constraints are applied. If the response is indeed strongest at the first tap, then it is reasonable to consider the response at only that tap in the definition of the MRC. Furthermore, since angle estimation is taking place independently of Doppler estimation, we only consider the spatial response at a fixed Doppler frequency, f_0. The desired spatial beampattern response is, thus, $\mathcal{W}(\phi, f_0) = \mathbf{W}_{main}^H \mathbf{v}(\phi, f_0)$, where for notational convenience the parameter representing temporal (range) dependency, l, has been left out. Once again, the MRC is defined as the real part of the ratio of difference to sum spatial responses at the

assumed Doppler frequency,

$$\mathcal{M}(\phi) = \Re\left\{\frac{\mathcal{W}_{\Delta}(\phi, f_0)}{\mathcal{W}_{\Sigma}(\phi, f_0)}\right\}. \tag{6.4}$$

Now that the MRC has been defined for the three-dimensional BASTAP processor, we consider a design approach for the respective sum and difference processors.

6.2 Constraint Design for BASTAP Monopulse

Angle estimation performance is governed by two factors: the mitigation performance of the respective sum and difference processors and, in a qualitative sense, the integrity of the MRC. In the previous chapter it was demonstrated that BASTAP performs quite well in terms of interference mitigation. However, experimental results on Mountaintop (MT) data in Chapter 4 showed that an SFT processor with a single unity gain constraint introduced significant distortion into the sum and difference beampatterns when staring directly at the TSI or jammer, which holds true for BASTAP as well. The distortions manifested themselves not only in the sidelobes, but also in the processor mainbeam. Distortions in the mainbeam pose the greatest threat to angle estimation, and, as such, it is necessary to alleviate them.

The approach taken in Chapter 4 for SFT monopulse was through application of spatial response constraints at T_0 and range constraints at successive taps. For BASTAP, target spreading was demonstrated to be negligible and, therefore, range constraints are not required. Specifying a full set of spatial response constraints at T_0 entailed giving up adaptivity completely at T_0. However, because of the presence of MSC, specifying a completely conventional beampattern response at the first tap of BASTAP is not an option, since no MSC cancellation could be achieved. Rather, a preferred choice is to implement a reduced set of spatial constraints within the mainbeam as shown in Fig. 6.1. In the figure, constraint locations in the space-Doppler spectrum are marked by "$\times$" symbols, where those in black denote a primary "on-Doppler" set of spatial response constraints (SRCs) and those in gray denote a

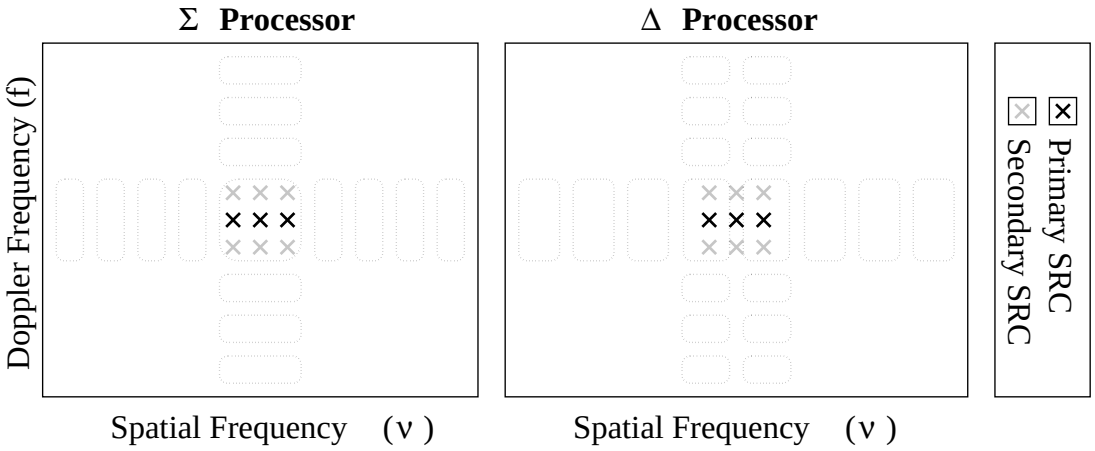

Figure 6.1: Constraint design for sum and difference BASTAP processors.

secondary "off-Doppler" set of SRCs. At the "×" locations the beampattern response is constrained to be that of the respective sum and difference conventional processors,

$$\mathbf{v}_\Sigma = \mathbf{v}(\nu_0, \bar{f}_0), \quad \mathbf{v}_\Delta = \left.\frac{\partial \mathbf{v}(\nu, \bar{f}_0)}{\partial \nu}\right|_{\nu_0}. \tag{6.5}$$

The constraint matrix and vector are given by

$$\mathbf{C}_\Sigma = \mathbf{C}_\Delta = \left[\begin{array}{cc} (\mathbf{B} \otimes \mathbf{A})^H & \mathbf{0}_{9\times T-1} \end{array} \right], \tag{6.6}$$

$$\mathbf{c}_\Sigma = (\mathbf{B} \otimes \mathbf{A})^H \mathbf{v}_\Sigma, \qquad \mathbf{c}_\Delta = (\mathbf{B} \otimes \mathbf{A})^H \mathbf{v}_\Delta, \tag{6.7}$$

where,

$$\begin{aligned} \mathbf{A} &= \left[\begin{array}{ccc} \mathbf{a}(\nu_0 - \frac{1}{2N}) & \mathbf{a}(\nu_0) & \mathbf{a}(\nu_0 + \frac{1}{2N}) \end{array} \right], \\ \mathbf{B} &= \left[\begin{array}{ccc} \mathbf{b}(\bar{f}_0 - \frac{1}{2M}) & \mathbf{b}(\bar{f}_0) & \mathbf{b}(\bar{f}_0 + \frac{1}{2M}) \end{array} \right]. \end{aligned} \tag{6.8}$$

The primary SRCs ensure that the MRC at the assumed Doppler, denoted as $\mathcal{M}_0$, "resembles" that of the conventional processor in Fig. 3.5.

The secondary, "off-Doppler" SRCs are chosen to address a different concern. In practice, the precise Doppler frequency of the target, f_t, is unknown, and all that is available is an estimate of the target Doppler, f_0. By employing the MRC for the

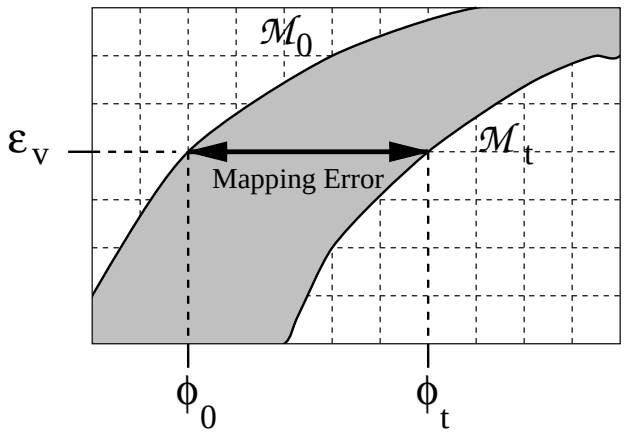

Figure 6.2: Illustration of a mapping error.

assumed Doppler, $\mathcal{M}_0$, in place of the MRC for the target Doppler, $\mathcal{M}_t$, a mapping error is introduced into the angle estimate. That is unless $\mathcal{M}_0 = \mathcal{M}_t$! To demonstrate the effect of a mapping error consider Fig. 6.2. An error voltage uncorrupted by interference maps through $\mathcal{M}_0$ to a corresponding angle, ϕ_0. Had the error voltage been used together with the correct MRC, $\mathcal{M}_t$, the correct angle measurement of ϕ_t would have been obtained. The resulting bias in angle estimate, $\hat{\phi}_0 - \phi_t$, is due purely to an error in the mapping function.

One of the advantages of the conventional processor defined in (2.10) is that it has a separable space-Doppler response (i.e., $\mathcal{W}(\phi, f) = \mathcal{W}(\phi)\mathcal{W}(f)$). Furthermore, the temporal (Doppler) components of the sum and difference vectors in (6.5) are equal, $\mathbf{b}_\Sigma(f) = \mathbf{b}_\Delta(f) = \mathbf{b}(f)$, and, thus, the temporal responses are equal, $\mathcal{W}_\Sigma(f) = \mathcal{W}_\Delta(f)$. As a result the temporal components in the MRC cancel out

$$\mathcal{M}(\phi) = \Re\left\{\frac{\mathcal{W}_\Delta(\phi)\mathcal{W}_\Delta(f)}{\mathcal{W}_\Sigma(\phi)\mathcal{W}_\Sigma(f)}\right\} = \Re\left\{\frac{\mathcal{W}_\Delta(\phi)}{\mathcal{W}_\Sigma(\phi)}\right\}, \tag{6.9}$$

making the MRC independent of the assumed Doppler frequency. In the design of the BASTAP sum and difference processors, because of the additional "anchor" points at $f_0 \pm \frac{1}{2M}$ as indicated by the gray marked $\times$ symbols in Fig. 6.1, the entire mainbeam surface is expected to resemble that of the conventional processor. Thus, the resulting

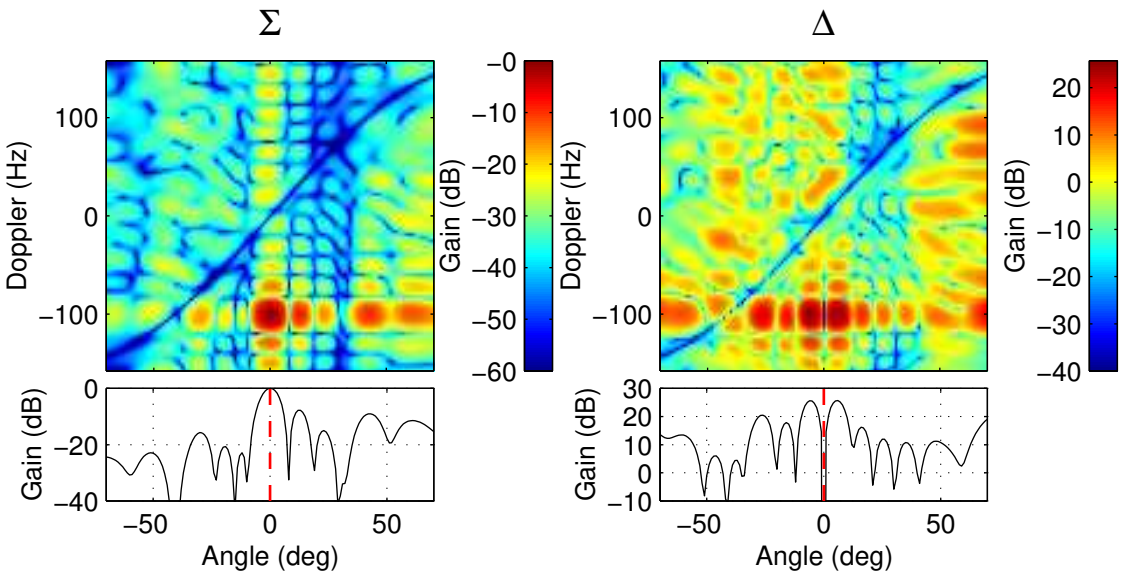

Figure 6.3: Beampattern responses for sidelobe jamming under stationary conditions with slices taken at −100 Hz.

adaptive monopulse processor possesses in an approximate sense (and only within the scope of the mainbeam region) the desired temporal independent MRC property of the conventional processor.

6.3 Simulation Results

As observed in the previous chapter, BASTAP performed quite well in terms of interference mitigation with respect to other processors. In this section various aspects of angle estimation performance and robustness of BASTAP monopulse are investigated through experimentation on MT TSI-data combined with synthetic MSC. Both sidelobe and mainbeam jamming scenarios are considered. Dataset `mmit004v1` is used to demonstrate results for stationary conditions and dataset `hot6067v1` is used to demonstrate results for nonstationary conditions.

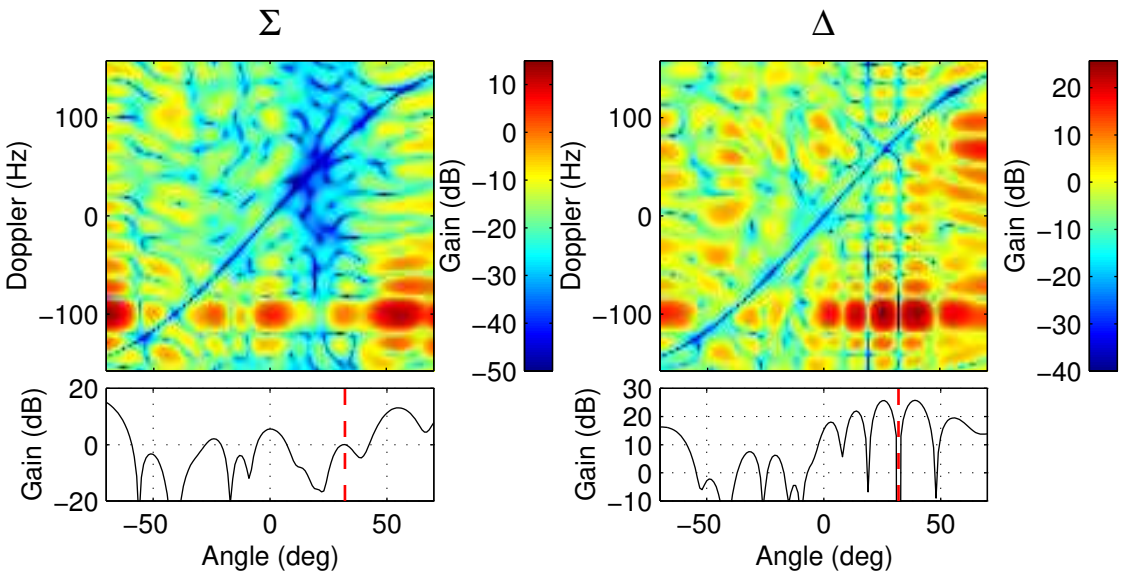

Figure 6.4: Beampattern responses for mainbeam jamming under stationary conditions with slices taken at −100 Hz.

6.3.1 Beampattern Response

Before proceeding to evaluate angle estimation performance, we wish to qualitatively evaluate beampattern responses under various conditions. The processor under consideration is a 300 tap BASTAP processor with 9 SRCs tuned to 0° and −100 Hz. The resulting sum and difference beampatterns are shown in Fig. 6.3. As expected the processors are well behaved throughout the space-Doppler spectrum. Doppler cuts at −100 Hz reveal low-distortion spatial beampatterns, which ultimately play an important role in maintaining the integrity of the MRC.

The mainbeam jamming scenario is considered in Fig. 6.4. As expected, the sidelobe levels are very poor. However, they have not degraded (in a noticeable fashion) beyond what was observed for the unity gain BASTAP processor of the previous chapter. On the other hand, the stability of the response within the mainbeam at 32° and −100 Hz is far improved for both sum and difference BASTAP processors with nine SRCs than what it would be with only a unity gain constraint.

Results for the nonstationary case are very similar to those presented for the

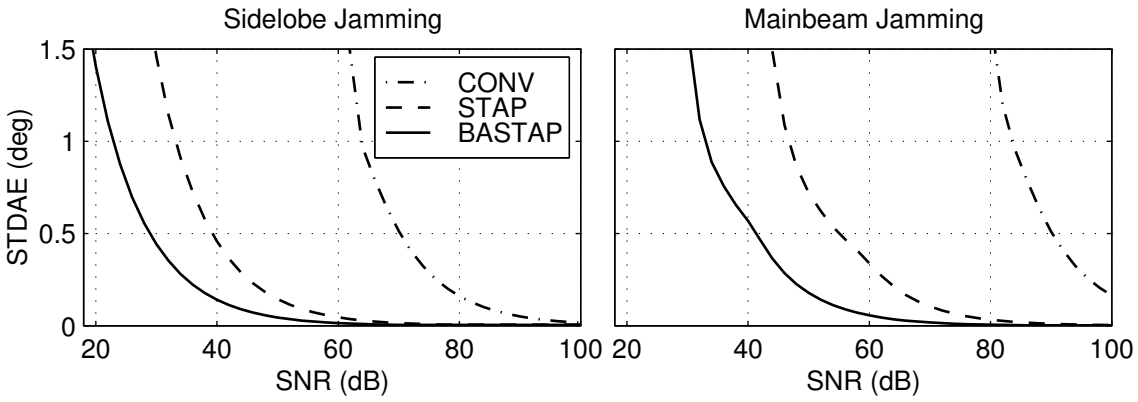

Figure 6.5: Angle estimation performance for sidelobe jamming and mainbeam jamming under stationary conditions.

stationary case and are therefore omitted.

6.3.2 Angle Estimation Performance

After having verified that the SRCs are able to maintain the integrity of the mainbeam in the sum processor and, likewise, of the split mainbeam in the difference processor, we proceed to evaluate angle estimation performance. We consider for the stationary environment a 300 tap BASTAP processor as before. Figure 6.5 illustrates results for the sidelobe and mainbeam jamming scenarios. The target SNR is varied from 20 to 100 dB and the worst case STDAE performance is recorded at each SNR increment. Angle estimation performance of BASTAP is clearly better than that of the other processors under consideration for both the sidelobe and mainbeam jamming scenarios.

In a nonstationary environment a 25 tap BASTAP processor with 16 reference beams was evaluated. Figure 6.6 illustrates results for the sidelobe and mainbeam jamming scenarios in the nonstationary environment. Although it is clear that the adaptive processors are less effective in the nonstationary case, still, the angle estimation performance is still far improved over that of the conventional processor. Once again BASTAP prevails over STAP for both sidelobe and mainbeam jamming.

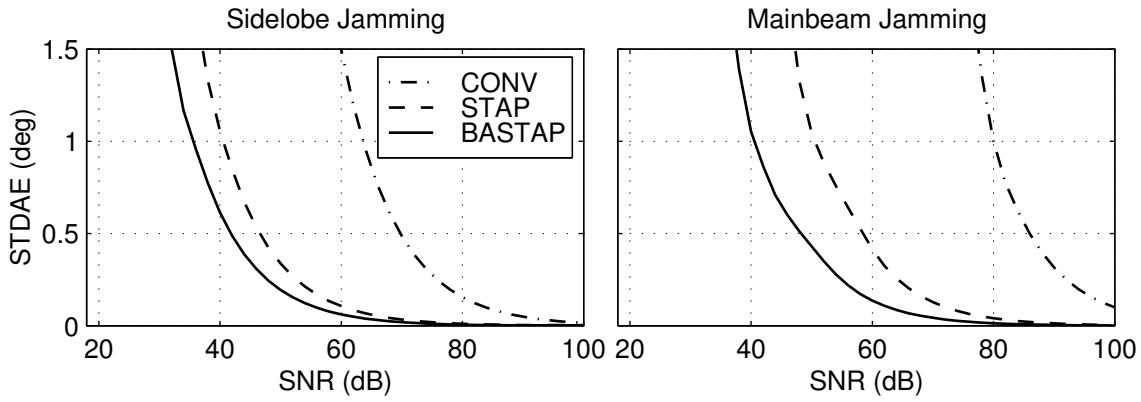

Figure 6.6: Angle estimation performance for sidelobe jamming and mainbeam jamming under nonstationary conditions.

6.3.3 MRC Spreading

It was stated earlier that the purpose of the secondary SRCs was to guard the MRC from small variations in Doppler. As shown next, in lacking a secondary set of "off-Doppler" SRCs, the MRC is subject to significant variation, consequently limiting STDAE performance. Figure 6.7 shows the effect of MRC spreading in a mainbeam jamming scenario for BASTAP with three and nine SRCs, respectively. The MRCs at the assumed Doppler frequency, $\mathcal{M}_0$, are indicated in black whereas MRCs in the range $0 < \left|\bar{f} - \bar{f}_0\right| < \frac{1}{2M}$ are indicated in gray. The extent of variation in the shape of the MRC is quite significant when only three SRCs are employed, as demonstrated by the "thick gray shadow" about $\mathcal{M}_0$. Unless the Doppler estimate can be refined further, STDAE performance is bound by the uncertainty of the MRC. For instance, assuming the error voltage output is uncorrupted by interference, the uncertainty in the mapping function alone introduces an uncertainty in the angle estimate, which for the three SRC example can be as high as 0.5° (taken to be the "thickest" horizontal width of the gray region). When all nine SRCs are utilized, the uncertainty in the MRC is diminished by a factor of approximately five, thus limiting angle estimation accuracy to 0.1°.

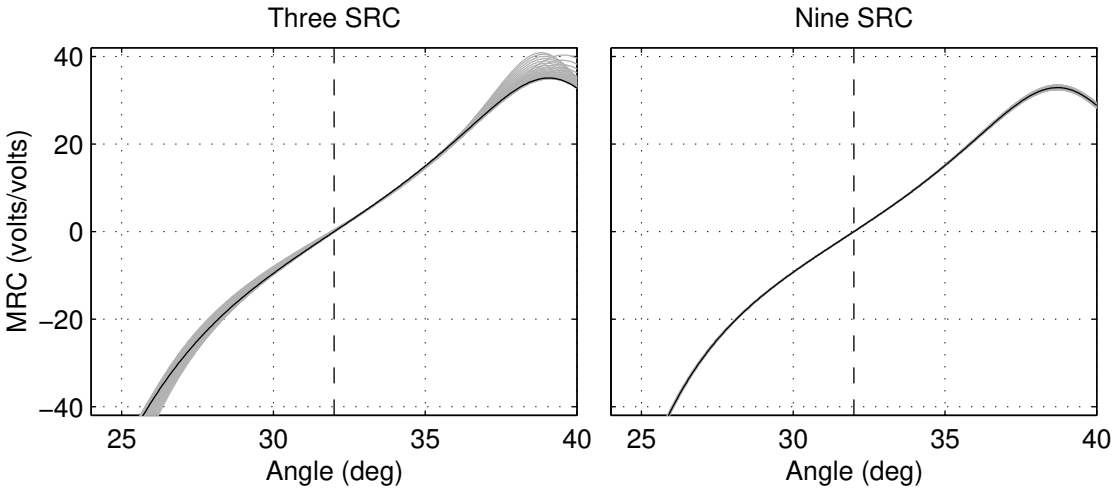

Figure 6.7: MRC Spreading (dashed line indicates look direction).

6.4 Joint Angle and Doppler Estimation

In [60] the principle behind joint azimuth and elevation angle estimation is described. The monopulse processor at hand employs a single sum beam output and two difference beam outputs. The ratio of each of the difference outputs to the sum output results in two error voltage outputs. Similarly, the ratio of each of the two difference beams to the sum beam results in two monopulse response curves (MRCs) to be used with the corresponding error voltage outputs. If the difference beams with respect to the sum beam lie in two separate planes, then each MRC maps the corresponding error voltage output to an angle in the associated plane (i.e., azimuth or elevation). However, this mapping only works if the MRCs in the corresponding planes are independent of the angle in the other plane. As noted before, a conventional beampattern possesses the separability property that guarantees the MRC to be independent of variation in the other plane, whether the other plane is an angle plane or a Doppler plane. Since BASTAP with nine SRCs is approximately separable within the mainbeam, as evidenced by the lack of MRC spreading in Fig. 6.7, the principle of joint azimuth-elevation estimation can be applied to joint angle-Doppler estimation for our BASTAP processor.

In a nonadaptive configuration the sum processor remains as a steering vector and the difference processors are derived from the steering vector by differentiating it with respect to the spatial and Doppler frequency variables, respectively,

$$\mathbf{W}_\Sigma = \mathbf{v}_\Sigma = \mathbf{v}(\nu_0, \bar{f}_0), \quad \mathbf{W}_{\Delta_1} = \mathbf{v}_{\Delta_1} = \left.\frac{\partial \mathbf{v}(\nu, \bar{f}_0)}{\partial \nu}\right|_{\nu_0}, \quad \mathbf{W}_{\Delta_2} = \mathbf{v}_{\Delta_2} = \left.\frac{\partial \mathbf{v}(\nu_0, \bar{f})}{\partial \bar{f}}\right|_{\bar{f}_0}. \tag{6.10}$$

The effect of taking the derivative with respect to each frequency variable can be observed in Fig. 6.8, where a horizontal and vertical null each split the mainbeam in a different plane. The sum and two difference outputs are given in terms of the respective processors

$$z_\Sigma(t) = \mathbf{W}_\Sigma^H \mathbf{Y}(t), \qquad z_{\Delta_1}(t) = \mathbf{W}_{\Delta_1}^H \mathbf{Y}(t), \qquad z_{\Delta_2}(t) = \mathbf{W}_{\Delta_2}^H \mathbf{Y}(t). \tag{6.11}$$

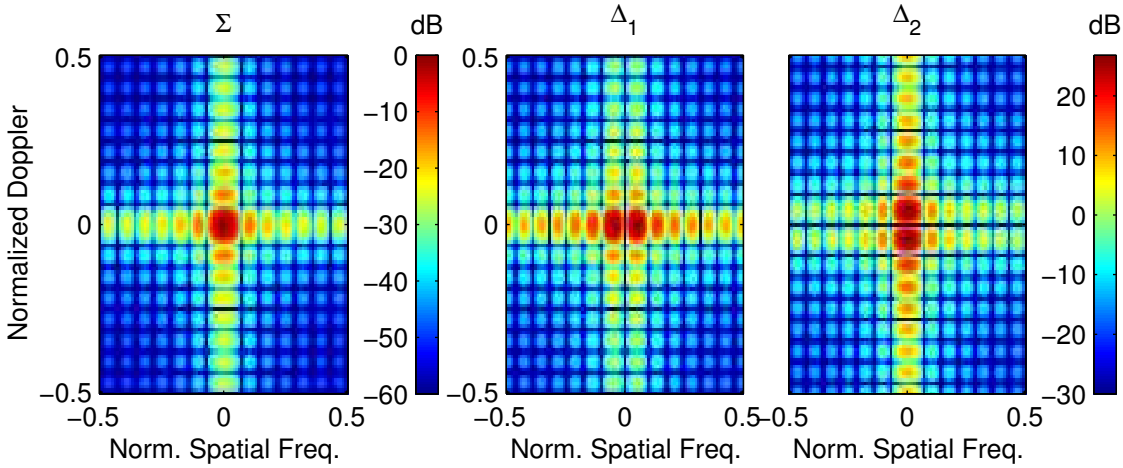

Figure 6.8: Beampattern responses of joint angle-Doppler monopulse components.

The real part of the ratio of each difference output to sum output gives us two error voltage outputs

$$\epsilon_1(t) = \Re\left\{\frac{z_{\Delta_1}(t)}{z_\Sigma(t)}\right\}, \qquad \epsilon_2(t) = \Re\left\{\frac{z_{\Delta_2}(t)}{z_\Sigma(t)}\right\}. \tag{6.12}$$

Similarly two MRCs are obtained by taking the real part of each of the difference to sum spatial responses

$$\mathcal{M}_1(\phi) = \Re\left\{\frac{\mathcal{W}_{\Delta_1}(\phi, f_0)}{\mathcal{W}_\Sigma(\phi, f_0)}\right\}, \qquad \mathcal{M}_2(\phi) = \Re\left\{\frac{\mathcal{W}_{\Delta_2}(\phi, f_0)}{\mathcal{W}_\Sigma(\phi, f_0)}\right\}. \tag{6.13}$$

Design of an adaptive joint angle-Doppler monopulse processor entails constraining the sum and two difference BASTAP beampattern responses in the first tap to match those of the corresponding conventional processors within the mainbeam.

$$\mathbf{C}_\Sigma = \mathbf{C}_{\Delta_1} = \mathbf{C}_{\Delta_2} = \left[\begin{array}{cc} (\mathbf{B}\otimes\mathbf{A})^H & \mathbf{0}_{9\times T-1} \end{array}\right], \tag{6.14}$$

$$\mathbf{c}_\Sigma = (\mathbf{B}\otimes\mathbf{A})^H \mathbf{v}_\Sigma, \qquad \mathbf{c}_{\Delta_1} = (\mathbf{B}\otimes\mathbf{A})^H \mathbf{v}_{\Delta_1}, \qquad \mathbf{c}_{\Delta_2} = (\mathbf{B}\otimes\mathbf{A})^H \mathbf{v}_{\Delta_2} \tag{6.15}$$

where $\mathbf{A}$ and $\mathbf{B}$ have been defined earlier in (6.8) and $\mathbf{v}_\Sigma$, $\mathbf{v}_{\Delta_1}$ and $\mathbf{v}_{\Delta_2}$ in (6.10).

6.5 Conclusions

This chapter extended the BASTAP architecture of the BASTAP processor in the previous chapter to perform monopulse processing. Initially, the monopulse concept was extended to three-dimensions to enable its use with BASTAP. Sum and difference processors employing BASTAP were designed through proper selection of constraints and successfully implemented in a monopulse system. Simulation results demonstrated the merit of BASTAP monopulse over STAP monopulse for both stationary and nonstationary conditions. At negligible expense to angle estimation performance it was shown that additional "off-Doppler" constraints provide stability to the MRC.

Although the design chosen for the BASTAP components of the monopulse system has been specifically tailored for robustness in a mainbeam jamming and TSI environment, its use under ordinary jamming conditions comes at little or no expense to angle estimation performance and also serves to stabilize the MRC. An added advantage of the nine-constraint design is that within the extent of the mainbeam the beampattern is approximately separable in the space and Doppler dimensions; thus allowing direct (non-iterative) joint angle-Doppler estimation to take place by employing an additional difference processor.

CHAPTER 7

Conclusions

The main topic addressed in this thesis is that of angle estimation in the presence of jamming (including mainbeam jamming), TSI and MSC. The methodology adopted was to extend the monopulse technique for angle estimation, traditionally employed in the spatial domain, to the space-time domain. In the presence of mainbeam jamming and TSI, this entailed generalizing the monopulse concept to SFT and then designing the sum and difference processor components. Linearly constrained optimization was employed to maximize interference rejection in the individual sum and difference components. Key features of the SFT processor included a tap-centered configuration along with extended range constraints and spatial response constraints. The tap-centered configuration was necessary because TSI and jammer samples were correlated at both forward and backward time lags as a result of analog baseband filters at the front end of the channel receivers. Extended range constraints were necessary to prevent target spreading across the entire mainbeam region at successive taps. Finally, spatial response constraints were necessary to ensure a robust MRC.

A comparison of SFT monopulse with spatial monopulse was conducted to demonstrate its merit over spatial monopulse. An extensive evaluation of SFT monopulse itself was conducted and various tradeoffs in performance and robustness were reported. A full set of constraints, for instance, was shown to offer increased robustness. However, at least twenty fast-time taps were necessary to provide advantage in terms of angle estimation performance over the nonrobust spatial adaptive monopulse pro-

cessor. Further analysis showed that the basis of the comparison was partly faulty and that the increased beamwidths of the more robust processors put them at an apparent disadvantage. The poor spatial response characteristics of all processors for mainbeam jamming conditions was shown to be far less problematic when considering the directional nature of the radar's transmission characteristics.

For an interference environment containing jamming, TSI, and MSC, an extra processing dimension was required. Because of the excessive computational and training requirements of a full rank three-dimensional processor, reduced rank alternatives were sought, ultimately leading to the development of Beam-Augmented STAP. STAP by itself was able to achieve a significant amount of cancellation in the combined interference environment, even in a mainbeam jamming scenario. Through the addition of one or more tapped reference beams and simultaneous optimization of all weights, the resulting BASTAP processor was able to enhance TSI and MSC mitigation over STAP. A comprehensive evaluation in a stationary TSI environment demonstrated the merit of BASTAP over STAP as well as over FBA. In a nonstationary TSI environment BASTAP performed on par with FBA but still fared better than STAP. Further analyses demonstrated the merit of BASTAP with respect to FBA even in the nonstationary TSI environment. The first of two such experiments demonstrated that beyond 40 dB of MSC (while maintaining the TSI level constant) FBA performance degrades significantly below that of BASTAP. In a second experiment it was demonstrated that a further increase in performance of BASTAP was possible by considering an optimal pointing direction for the reference beam.

A similar methodology for extending spatial monopulse to SFT monopulse was used in arriving at a BASTAP monopulse architecture. The sum and difference processor components were designed to have low-distortion in the mainbeam region of the space-Doppler response at the first tap, thus ensuring a robust MRC for angle estimation. Additional care was taken to minimize the effect of Doppler mismatch on the resulting angle estimates through the use of added constraints in the mainbeam

region. Performance evaluation of the resulting three-dimensional monopulse processor demonstrated a clear advantage in employing BASTAP over ordinary STAP for angle estimation. Finally, an algorithm employing a sum beam and two difference beams for performing joint angle-Doppler estimation was derived.

7.1 Contributions

The contributions of this thesis include:

- A method by which a monopulse processor is combined with an adaptive space-time processor to provide a precise angle tracking capability in the presence of TSI and mainbeam jamming.
- An innovative three-dimensional processor that offers improved mitigation performance in the presence of combined MSC, TSI, and mainbeam jamming.
- A generalization of this algorithm to operate in the presence of nonstationary jamming generated by airborne jammers.
- An extension of this algorithm to perform joint angle-Doppler estimation.
- A complete package for monopulse processing in MSC, TSI, and mainbeam jamming for both ground based and airborne radar and jammers.

7.2 Future Work

The main objectives of this thesis – to develop an SFT monopulse algorithm and a three-dimensional reduced rank algorithm for mitigation and monopulse processing in the combined presence of MSC, TSI, and mainbeam jamming – were met. A comprehensive evaluation of the proposed algorithms was conducted but much remains to be investigated and improved upon. Some possibilities for future research include:

- Investigation of a means by which to reduce the high gain artifacts present in the beampattern responses of the sum and difference processors in a mainbeam jamming scenario. The high gain artifacts pose a significant threat if a second target enters and corrupts the monopulse output through the artifact. In such cases it may be necessary to artificially suppress that artifact through added constraints.

- Exploration of BASTAP with alternative tap configurations and thinned weights. A tap-centered configuration proved beneficial to SFT monopulse. Likewise, it could prove beneficial in conjunction with BASTAP, whereas weight thinning could prove beneficial by way of rank reduction.

- Development of improved beam placement strategies. As demonstrated in the thesis, optimal beam placement can improve mitigation performance.

- Exploration of partial dimension BASTAP architectures. At present BASTAP requires solving simultaneously for a full set of STAP and reference beam weights. Although a significant reduction in rank was achieved with BASTAP, the computational and training resource demands are, nonetheless, still significant. One possibility is to implement extended-BASTAP in an element-space post-Doppler configuration [66, 12, 64], where each Doppler partition receives its own reference beam(s).

- Employment of experimental TSI in conjunction with experimental MSC in evaluating BASTAP. Only synthetic MSC has been used in this thesis.

- Investigation of various training strategies for SFT monopulse and BASTAP. At present no particular consideration has been given to the method of training. Different training strategies might not only prove more efficient, but will be necessary when considering nonstationary experimental MSC and the need for target free training data [59].

APPENDIX A

Zero-Bias Constraint Vs. No Constraint

In comparing the standard monopulse algorithm to its zero-bias variation developed by Castella in [10], it was noted that the performance curves came out precisely the same. In fact, it can be shown that not only are the statistical performance curves identical but that the deterministic angle estimates are equivalent. This implies that imposing the additional zero-bias constraint does not benefit angle estimation performance, despite what appears to be an improved difference beampattern response. An analytical proof of this result follows.

Let $\mathbf{W}_S$ and $\mathbf{W}_D$ represent the standard adaptive sum and difference weight vectors, and $\bar{\mathbf{W}}_S$ and $\bar{\mathbf{W}}_D$ represent the zero-bias adaptive sum and difference weight vectors. Also, let $\mathbf{S}$ represent a conventional sum processor and $\mathbf{D}$ a conventional difference processor. Applying Castella's difference processor constraints to (2.24),

$$\begin{aligned}
\bar{\mathbf{W}}_{\mathbf{D}} &= \mathbf{R}^{-1}\begin{bmatrix}\mathbf{D} & \mathbf{S}\end{bmatrix}\left(\begin{bmatrix}\mathbf{D} & \mathbf{S}\end{bmatrix}^H\mathbf{R}^{-1}\begin{bmatrix}\mathbf{D} & \mathbf{S}\end{bmatrix}\right)^{-1}\begin{bmatrix}1\\0\end{bmatrix} \qquad \text{(A.1)}\\
&= \mathbf{R}^{-1}\begin{bmatrix}\mathbf{D} & \mathbf{S}\end{bmatrix}\frac{\begin{bmatrix}\mathbf{S}^H\mathbf{R}^{-1}\mathbf{S} & -\mathbf{D}^H\mathbf{R}^{-1}\mathbf{S}\\ -\mathbf{S}^H\mathbf{R}^{-1}\mathbf{D} & \mathbf{D}^H\mathbf{R}^{-1}\mathbf{D}\end{bmatrix}}{(\mathbf{S}^H\mathbf{R}^{-1}\mathbf{S})(\mathbf{D}^H\mathbf{R}^{-1}\mathbf{D})-(\mathbf{D}^H\mathbf{R}^{-1}\mathbf{S})(\mathbf{S}^H\mathbf{R}^{-1}\mathbf{D})}\begin{bmatrix}1\\0\end{bmatrix}\\
&= k_1\frac{\mathbf{R}^{-1}\mathbf{D}}{\mathbf{D}^H\mathbf{R}^{-1}\mathbf{D}}+k_2\frac{\mathbf{R}^{-1}\mathbf{S}}{\mathbf{S}^H\mathbf{R}^{-1}\mathbf{S}}\\
&= k_1\mathbf{W}_{\mathbf{D}}+k_2\mathbf{W}_{\mathbf{S}}
\end{aligned}$$

where,

$$k_1 = \frac{(\mathbf{S}^H\mathbf{R}^{-1}\mathbf{S})(\mathbf{D}^H\mathbf{R}^{-1}\mathbf{D})}{(\mathbf{S}^H\mathbf{R}^{-1}\mathbf{S})(\mathbf{D}^H\mathbf{R}^{-1}\mathbf{D}) - (\mathbf{D}^H\mathbf{R}^{-1}\mathbf{S})(\mathbf{S}^H\mathbf{R}^{-1}\mathbf{D})}$$
$$k_2 = \frac{-(\mathbf{S}^H\mathbf{R}^{-1}\mathbf{D})(\mathbf{S}^H\mathbf{R}^{-1}\mathbf{S})}{(\mathbf{S}^H\mathbf{R}^{-1}\mathbf{S})(\mathbf{D}^H\mathbf{R}^{-1}\mathbf{D}) - (\mathbf{D}^H\mathbf{R}^{-1}\mathbf{S})(\mathbf{S}^H\mathbf{R}^{-1}\mathbf{D})}. \tag{A.2}$$

Both the standard and Castella's version of the sum processor are equal.

$$\bar{\mathbf{W}}_S = \mathbf{W}_S \tag{A.3}$$

The error voltage of Castella's processor can be expressed in terms of the error voltage of the standard processor,

$$\bar{\epsilon}_v(\mathbf{x}) = \frac{\bar{\mathbf{W}}_D^H\mathbf{x}}{\bar{\mathbf{W}}_S^H\mathbf{x}} = \frac{\bar{\mathbf{W}}_D^H\mathbf{x}}{\mathbf{W}_S^H\mathbf{x}} = k_1^*\epsilon_v(\mathbf{x}) + k_2^*, \tag{A.4}$$

where the error voltage of the standard processor is

$$\epsilon_v(\mathbf{x}) = \frac{\mathbf{W}_D^H\mathbf{x}}{\mathbf{W}_S^H\mathbf{x}}. \tag{A.5}$$

Similarly, the MRC of Castella's processor can be expressed as a function of the MRC of the standard processor

$$\bar{\mathcal{M}}(\phi) = \frac{\bar{\mathbf{W}}_D^H\mathbf{a}(\phi)}{\bar{\mathbf{W}}_S^H\mathbf{a}(\phi)} = \frac{\bar{\mathbf{W}}_D^H\mathbf{a}(\phi)}{\mathbf{W}_S^H\mathbf{a}(\phi)} = k_1^*\mathcal{M}(\phi) + k_2^*, \tag{A.6}$$

where the MRC of the standard processor is

$$\mathcal{M}(\phi) = \frac{\mathbf{W}_D^H\mathbf{a}(\phi)}{\mathbf{W}_S^H\mathbf{a}(\phi)}. \tag{A.7}$$

What remains to be shown is that $\bar{\phi}(\mathbf{x}) = \phi(\mathbf{x})$.

$$\begin{aligned}
\bar{\phi}(\mathbf{x}) &= \bar{\mathcal{M}}^{-1}\left\{\bar{\epsilon}_v(\mathbf{x})\right\} \qquad (A.8)\\
&= \bar{\mathcal{M}}^{-1}\left\{k_1^*\epsilon_v(\mathbf{x}) + k_2^*\right\}\\
&= \mathcal{M}^{-1}\left\{\frac{1}{k_1^*}\left[(k_1^*\epsilon_v(\mathbf{x}) + k_2^*) - k_2^*\right]\right\}\\
&= \mathcal{M}^{-1}\left\{\epsilon_v(\mathbf{x})\right\}\\
&= \phi(\mathbf{x})
\end{aligned}$$

One of the steps in (A.8) assumes that $\bar{\mathcal{M}}^{-1}\{y\} = \mathcal{M}^{-1}\left\{\frac{1}{k_1^*}(y - k_2^*)\right\}$. This is in fact only true when $\mathcal{M}(y)$ is a continuous monotone increasing or decreasing function (i.e., invertible), which is the case for any valid monopulse function.

Since no conditions have been placed on the difference processor, $\mathbf{D}$, the proof provided in this appendix applies to arbitrary difference weights, including space-time weights.

APPENDIX B

Acronyms

Table B.1: Acronyms used in the thesis.

Acronym	Meaning
AEW	airborne early warning
BASTAP	beam augmented STAP
CPI	coherent processing interval
dB	decibel
DFT	discrete Fourier transform
DOF	degrees of freedom
FBA	factored beamspace algorithm
INR	interference-to-noise ratio
KHz	kilohertz
KW	kilowatt
LFM	linear frequency modulation
MC	Monte Carlo
MHz	megahertz

continued on next page

continued from previous page

Symbol	Definition
MF	monopulse formula
ML	maximum likelihood
MRC	monopulse response curve
MSC	monostatic clutter
MT	mountaintop
MV	minimum variance
OINR	output interference-to-noise ratio
pdf	probability density function
PRI	pulse repetition interval
RF	radio frequency
rms	root mean square
SFT	space/fast-time
SINR	signal-to-interference plus noise ratio
SMI	sample matrix inversion
SNR	signal-to-noise ratio
SRC	spatial response constraint
SRB	single reference beam canceler
SST	space/slow-time
STD	standard deviation
STDAE	standard deviation of angle error
STAP	space-time adaptive processing
TSI	terrain scattered interference

continued on next page

continued from previous page	
Symbol	Definition
UHF	ultra high frequency
ULA	uniform linear array

Bibliography

[1] Edward J. Baranoski. Improved pre-doppler STAP algorithm for adaptive clutter nulling in airborne radars. In *Proc. Asilomar Conf. on Signals, Systems, and Computers*, volume 2, pages 1173–1177, 1995.

[2] David. K. Barton and Harold R. Ward. *Handbook of Radar Measurement*. Artech House Inc., Dedham, MA, 1984.

[3] E. T. Bayliss. Design of monopulse antenna difference patterns with low sidelobes. *The Bell System Technical Journal*, 47:623–650, May–Jun. 1968.

[4] D. M. Boroson. Sample size considerations for adaptive arrays. *IEEE Transactions on Aerospace and Electronic Systems*, 16(4):446–451, July 1980.

[5] L. E. Brennan. Angular accuracy of a phased array radar. *IRE Transactions on Antennas and Propagation*, 9:268–275, May 1961.

[6] L. E. Brennan, J. D. Mallet, and I. S. Reed. Adaptive arrays in airborne MTI radar. *IEEE Transactions on Aerospace and Electronic Systems*, 12(5):607–615, September 1976.

[7] L. E. Brennan and I. S. Reed. Theory of adaptive radar. *IEEE Transactions on Aerospace and Electronic Systems*, 9(2):237–252, March 1973.

[8] B. D. Carlson, L. M. Goodman, J. Austin, M. W. Ganz., and L. O. Upton. An ultralow-sidelobe adaptive array antenna. *The Lincoln Laboratory Journal*, 3(2):291–310, Summer 1990.

[9] Blair D. Carlson. Covariance matrix estimation errors and diagonal loading in adaptive arrays. *IEEE Transactions on Aerospace and Electronic Systems*, 24(4):397–401, July 1988.

[10] F. R. Castella. Adaptive antenna nulling for a phased array monopulse radar. In *Proc. of IEEE International Radar Conference*, pages 320–323, Brighton, UK, October 1992.

[11] R. C. Davis, L. E. Brennan, and L. S. Reed. Angle estimation with adaptive arrays in external noise fields. *IEEE Transactions on Aerospace and Electronic Systems*, 12(2):179–186, March 1976.

[12] R. C. DiPietro. Extended factored space-time processing for airborne radar systems. In *Proc. Asilomar Conf. on Signals, Systems, and Computers*, volume 1, pages 425–430, 1992.

[13] Ronald L. Fante. Cancellation of specular and diffuse jammer multipath using a hybrid adaptive array. *IEEE Transactions on Aerospace and Electronic Systems*, 27(5):823–837, September 1991.

[14] Ronald L. Fante. A simple approach for canceling diffuse jammer multipath. Technical Report MTR 94B0000085, MITRE, August 1994.

[15] Ronald L. Fante, Richard M. Davis, and Thomas P. Guell. Wideband cancellation of multiple mainbeam jammers. *IEEE Transactions on Antennas and Propagation*, 44(10):1402–1413, October 1996.

[16] Ronald L. Fante and Jose A. Torres. Cancellation of diffuse jammer multipath by an airborne adaptive radar. *IEEE Transactions on Aerospace and Electronic Systems*, 31(2):805–820, April 1995.

[17] O. L. Frost. An algorithm for linearly constrained adaptive array processing. *Proceedings of the IEEE*, 60(8):926–935, August 1972.

[18] R. A. Gabel. Mountaintop bistatic jamming experiments and analysis. In *Proc. of Adaptive Sensor Array Processing (ASAP) Workshop*, pages 491–513. MIT Lincoln Laboratory, March 1995.

[19] R. A. Gabel. TSI mitigation weight training experiments. In *Proc. of 3rd ARPA Mountaintop Hot Clutter TIM*, pages 249–294. USAF Rome Laboratory, August 1995.

[20] W. F. Gabriel. A high-resolution target-tracking concept using spectral estimation techniques. NRL Report 8797, Naval Research Laboratory, 1984.

[21] Lloyd J. Griffiths. Adaptive monopulse beamforming. *Proceedings of the IEEE*, 64(8):1260–1261, August 1976.

[22] Lloyd J. Griffiths. Linear constraints in hot clutter cancellation. In *Proc. of 3rd ARPA Mountaintop Hot Clutter TIM*, pages 297–326. USAF Rome Laboratory, August 1995.

[23] Lloyd J. Griffiths. Adaptive hot clutter mitigation using multiple linear constraints. In *Proc. of Adaptive Sensor Array Processing (ASAP) Workshop*. MIT Lincoln Laboratory, March 1996.

[24] Lloyd J. Griffiths. Linear constraints in hot clutter cancellation. In *Proc. of IEEE Int. Conf. on Acoustics, Speech, and Signal Processing*, volume 2, pages 1181–1184, May 1996.

[25] Lloyd J. Griffiths and Charles W. Jim. Alternative approach to linearly constrained adaptive beamforming. *IEEE Transactions on Antennas and Propagation*, 30(1):27–34, January 1982.

[26] S. Haykin, J. Litva, and T. J. Shepherd. *Radar Array Processing*. Springer-Verlag, NY, NY, 1993.

[27] Roger A. Horn and Charles R. Johnson. *Topics in matrix analysis*. Cambridge University Press, NY, NY, 1991.

[28] Mary Ann Ingram, Johan Kullstam, and Ho Yang. Fading model for terrain-scattered interference. In *Proc. of 3rd ARPA Mountaintop Hot Clutter TIM*, pages 130–169. USAF Rome Laboratory, August 1995.

[29] Don H. Johnson and D. E. Dudgeon. *Array Signal Processing*. Prentice Hall, Englewood Cliffs, NJ, 1993.

[30] William C. Jones, Jr. Cancellation of TSI in airborne fire-control radars. In *Proc. of Adaptive Sensor Array Processing (ASAP) Workshop*, pages 475–490. MIT Lincoln Laboratory, March 1995.

[31] Stephen M. Kogon. *Adaptive Array Processing Techniques for Terrain Scattered Interference Mitigation*. PhD thesis, Georgia Institute of Technology, 1996.

[32] Stephen M. Kogon, E. Jeff Holder, and Douglas B. Williams. On the use of terrain scattered interference for mainbeam jammer suppression. In *Proc. of Adaptive Sensor Array Processing (ASAP) Workshop*. MIT Lincoln Laboratory, March 1997.

[33] Stephen M. Kogon, E. Jeff Holder, Douglas B. Williams, M. P. Fargues, and R. D. Hippenstiel. Mainbeam jammer suppression using multipath returns. In *Proc. Asilomar Conf. on Signals, Systems, and Computers*, volume 1, pages 279–283, 1997.

[34] Stephen M. Kogon, Douglas B. Williams, and E. Jeff Holder. Beamspace techniques for hot clutter cancellation. In *Proc. of IEEE Int. Conf. on Acoustics, Speech, and Signal Processing*, volume 2, pages 1177–1180, May 1996.

[35] Stephen M. Kogon, Douglas B. Williams, and E. Jeff Holder. Hot clutter cancellation with orthogonal beamspace transforms. In *Proc. of Adaptive Sensor Array Processing (ASAP) Workshop*. MIT Lincoln Laboratory, March 1996.

[36] Stephen M. Kogon, Douglas B. Williams, and James H. McClellan. Factored mitigation of terrain scattered interference and monostatic clutter. In *Proc. Asilomar Conf. on Signals, Systems, and Computers*, pages 526–530, 1996.

[37] Stephen M. Kogon, Douglas B. Williams, and James H. McClellan. Exploiting coherent multipath for mainbeam jammer suppression. *IEE Proceedings – Radar, Sonar and Navigation*, 145(5):303–308, October 1998.

[38] A. I. Leonov and K. I. Fomichev. *Monopulse Radar*. Artech House Inc., Norwood, MA, 1986.

[39] Feng-Ling C. Lin and Frank F. Kretschmer, Jr. Angle estimation in the presence of mainbeam interference. Technical Report 9234, NRL, 1989.

[40] Feng-Ling C. Lin and Frank F. Kretschmer, Jr. Angle measurement in the presence of mainbeam interference. In *Proc. of IEEE International Radar Conference*, pages 444–450, Arlington, VA, May 1990.

[41] Feng-Ling C. Lin and Frank F. Kretschmer, Jr. Performance of an angle-of-arrival estimator in the presence of a mainbeam interference source. Technical Report 9345, NRL, August 1992.

[42] Robert J. Mailloux. *Phased Array Antenna Handbook*. Artech House Inc., Norwood, MA, 1994.

[43] Daniel F. Marshall. A two step adaptive interference nulling algorithm for use with airborne sensor arrays. In *Proc. of the Seventh SP Workshop on Statistical Signal and Array Processing*, pages 301–304, 1994.

[44] Daniel F. Marshall and Robert A. Gabel. Simultaneous mitigation of multipath jamming and ground clutter. In *Proc. of Adaptive Sensor Array Processing (ASAP) Workshop*, pages 285–313. MIT Lincoln Laboratory, March 1996.

[45] Thomas W. Miller and Janet M. Ortiz. An overview of issues in hot clutter mitigation. In *Proc. of Adaptive Sensor Array Processing (ASAP) Workshop*, pages 193–239. MIT Lincoln Laboratory, March 1996.

[46] Dennis R. Morgan and Athanasios Aridgides. Adaptive sidelobe cancellation of wide-band multipath interference. *IEEE Transactions on Antennas and Propagation*, 33(8):908–917, August 1985.

[47] U. Nickel. Monopulse estimation with subarray-adaptive arrays and arbitrary sum and difference beams. *IEE Proceedings – Radar, Sonar and Navigation*, 143(4):232–238, August 1996.

[48] Ramon Nitzberg. *Adaptive Signal Processing for Radar.* Artech House Inc., Boston, MA, 1992.

[49] Athanasios Papoulis. *Probability, Random Variables, and Stochastic Processes.* McGraw-Hill Inc., NY, NY, third edition, 1991.

[50] O. R. Price and R. F. Hyneman. Distribution functions for monopulse antenna difference patterns. *IRE Transactions on Antennas and Propagation*, 8:567–576, November 1960.

[51] Daniel J. Rabideau. Advanced STAP for TSI modulated clutter. In *Proc. of Adaptive Sensor Array Processing (ASAP) Workshop*, pages 263–287. MIT Lincoln Laboratory, March 1998.

[52] I. S. Reed, J. D. Mallet, and L. E. Brennan. Rapid convergence rate in adaptive arrays. *IEEE Transactions on Aerospace and Electronic Systems*, 10(6):853–863, November 1974.

[53] Donald R. Rhodes. *Introduction to Monopulse.* Artech House Inc., Dedham, MA, 1980.

[54] D. Curtis Schleher. *Introduction to Electronic Warfare.* Artech House Inc., Norwood, MA, 1986.

[55] Yaron Seliktar, E. Jeff Holder, and Douglas B. Williams. An adaptive monopulse processor for angle estimation in a mainbeam jamming and coherent interference scenario. In *Proc. of IEEE Int. Conf. on Acoustics, Speech, and Signal Processing*, volume 4, pages 2037–2040, May 1998.

[56] Yaron Seliktar, Douglas B. Williams, and E. Jeff Holder. Adaptive monopulse processing in the presence of TSI and mainbeam jamming. In *Proc. of Adaptive Sensor Array Processing (ASAP) Workshop*, pages 103–120. MIT Lincoln Laboratory, March 1998.

[57] Yaron Seliktar, Douglas B. Williams, and E. Jeff Holder. Adaptive monopulse processing of monostatic clutter and coherent interference in the presence of mainbeam jamming. In *Proc. Asilomar Conf. on Signals, Systems, and Computers*, November 1998.

[58] Yaron Seliktar, Douglas B. Williams, and E. Jeff Holder. Beam-augmented space-time adaptive processing. In *Proc. of IEEE Int. Conf. on Acoustics, Speech, and Signal Processing*, March 1999.

[59] Yaron Seliktar, Douglas B. Williams, and James H. McClellan. Evaluation of partially adaptive STAP algorithms on the mountain top data set. In *Proc. of IEEE Int. Conf. on Acoustics, Speech, and Signal Processing*, volume 2, pages 1169–1172, May 1996.

[60] Samuel M. Sherman. *Monopulse Principles and Techniques.* Artech House Inc., Norwood, MA, 1984.

[61] Merryl I. Skolnik. *Radar Handbook*. McGraw-Hill Inc., NY, NY, second edition, 1990.

[62] G. W. Titi and D. F. Marshal. The ARPA/NAVY mountaintop program: adaptive signal processing for airborne early warning radar. In *Proc. of IEEE Int. Conf. on Acoustics, Speech, and Signal Processing*, volume 2, pages 1165–1168, May 1996.

[63] USAF Rome Laboratory. *Mountaintop Program Summit Data: ASAP 1995 Data Release*, March 1995.

[64] Hong Wang and Lujing Cai. On adaptive spatial-temporal processing for airborne surveillance radar systems. *IEEE Transactions on Aerospace and Electronic Systems*, 30(3):660–669, July 1994.

[65] James Ward, Edward J. Baranoski, and Robert A. Gabel. Adaptive processing for airborne surveillance radar. In *Proc. Asilomar Conf. on Signals, Systems, and Computers*, volume 1, pages 566–571, 1997.

[66] Jim Ward. Space-time adaptive processing for airborne radar. Technical Report 1015, MIT Lincoln Laboratory, 1994.

[67] Jim Ward. Space-time adaptive processing for airborne radar. In *Proc. of IEEE Int. Conf. on Acoustics, Speech, and Signal Processing*, volume 5, pages 2809–2812, May 1995.

[68] Michael D. Zoltowski and Ta-Sung Lee. ML based monopulse bearing estimation for adaptive phased array radar. In *Proc. Asilomar Conf. on Signals, Systems, and Computers*, volume 1, pages 390–394, 1989.

Vita

Yaron Seliktar was born in Glasgow, Scotland, on September 22, 1969. He received his bachelors degree in Electrical Engineering from Drexel University in 1992, a Master of Science degree in Electrical Engineering from the Georgia Institute of Technology in September 1993, and a Ph.D. degree in Electrical Engineering, from the Georgia Institute of Technology, in March of 1999.

Yaron served as a teaching assistant in the Digital Hardware Laboratory, at the Georgia Institute of Technology, school of Electrical and Computer Engineering, from September 1992 to December 1994. In June 1993 he joined the Digital Signal Processing Laboratory at the Georgia Institute of Technology and held an from September 1992 to December 1994. In June 1993 he joined the Digital Signal Processing Laboratory at the Georgia Institute of Technology and held an appointment of research assistant from September 1994 to September 1996. In September 1996, he was appointed research assistant at the Georgia Tech Research Institute (GTRI), in the Sensors and Electromagnetic Applications Laboratory, and has held this appointment to date. Recently he was offered a position at Norden Systems Northrop Grumman as part of the Electronic Sensors and Systems Division in Norwalk Connecticut, which he accepted and intends to assume on February 1, 1999. Yaron's research interests include statistical signal processing, adaptive space-time array processing, and their application to RADAR signal processing.